UNIVERSITY OF KENT

DOCTORAL THESIS

Time-Stretched Supercontinuum Swept-Sources for High-Speed Optical Coherence Tomography

Author:

Sacha Oscar Darius GRELET

Supervisor:

Prof Adrian Gh. PODOLEANU

A thesis submitted in fulfilment of the requirements

for the degree of Doctor of Philosophy

in the

Applied Optics Group

School of Physical Sciences

June 2025

Declaration of Authorship

I, Sacha Oscar Darius GRELET, declare that this thesis titled, "Time-Stretched Supercontinuum Swept-Sources for High-Speed Optical Coherence Tomography" and the work presented in it are my own. I confirm that:

- This work was done wholly or mainly while in candidature for a research degree at this University.
- Where any part of this thesis has previously been submitted for a degree or any other qualification at this University or any other institution, this has been clearly stated.
- Where I have consulted the published work of others, this is always clearly attributed.
- Where I have quoted from the work of others, the source is always given. With the exception of such quotations, this thesis is entirely my own work.
- I have acknowledged all main sources of help.
- Where the thesis is based on work done by myself jointly with others, I have made clear exactly what was done by others and what I have contributed myself.

Signed:
Sacha Oscar Darius Grelet

Date:
16/04/2026

Last compiled: Thursday 16th April, 2026 at 2:16pm.

"Je suis de ceux qui pensent que la Science a une grande beauté. Un savant dans son laboratoire n'est pas seulement un technicien: c'est aussi un enfant placé en face de phénomènes naturels qui l'impressionnent comme un conte de fées. Nous devons avoir un moyen pour communiquer ce sentiment à l'extérieur; nous ne devons pas laisser croire que tout progrès scientifique se réduit à des mécanismes, des machines, des engrenages, qui, d'ailleurs ont également leur beauté propre.

Je ne crois pas non plus que dans notre monde, l'esprit d'aventure risque de disparaître. Si je vois autour de moi quelque chose de vital, c'est précisément l'esprit d'aventure qui paraît indéracinable et s'apparente à la curiosité. On trouve l'esprit d'aventure chez les enfants, à tous les âges et à tous les degrés."

Marie Skłodowska-Curie, French-Polish physicist and chemist

Abstract

SINCE its introduction, optical coherence tomography (OCT) has become a widely used imaging technique for non-invasive, three-dimensional visualisation of biological tissues. Although resolution has steadily improved, imaging speed remains a key limitation—particularly for reducing motion artefacts and enabling real-time volumetric acquisition. Swept-source OCT (SS-OCT), which uses rapidly wavelength-tunable lasers, has enabled imaging at MHz-scale A-scan rates. However, most conventional swept-source designs rely on mechanically tuned elements, which fundamentally restrict further increases in speed. To overcome this, recent research has turned to akinetic swept-source technologies, which avoid moving parts entirely.

This thesis explores an akinetic swept-source approach based on time-stretched supercontinuum generation. In this technique, ultrashort, high-peak-power pulses are passed through a nonlinear medium to generate a broadband supercontinuum, which is then dispersed through a highly chromatic medium. This process creates a passive wavelength sweep through group delay dispersion. First proposed by Moon *et. al.* in 2006, the approach was initially limited by high noise levels inherent to conventional supercontinuum sources. However, with the development of all-normal dispersion (ANDi) fibres, it became possible to generate broadband light with much lower noise. This work builds on that foundation, investigating whether an ANDi-based time-stretched supercontinuum source at 1060 nm could be suitable for high-speed SS-OCT.

Two swept-source systems were developed as part of this work. The first, operating at 80 MHz, used a fibre-based dispersive stretcher, with the nonlinear broadening optimised through numerical simulations. OCT imaging was demonstrated at an A-scan rate of 40 MHz, and full-volume imaging at 400 Hz was achieved using a fast electro-optic scanner. Although promising, this high-speed setup proved less suited to imaging weakly scattering samples, such as the retina, due to shot and electronic noise. A second source operating at 10 MHz was therefore developed. This version used a custom-fabricated chirped fibre Bragg grating to provide the required dispersion while avoiding the losses associated with long fibre stretchers. A pulse picker was also implemented to reduce the laser's repetition rate, and the supercontinuum generation process was further refined. Using this lower-rate source, low-noise in vivo imaging was successfully carried out on dermal and retinal tissue. Fine structures such as sweat ducts, the retinal nerve fibre layer, and the choroid were clearly visualised. These results demonstrate the feasibility of ANDi-based time-stretched supercontinuum sources for high-speed OCT and highlight their potential for a wide range of biomedical imaging applications.

Acknowledgements

THIS thesis would not have been possible without the support and contributions of many wonderful people. First and foremost, I thank Prof. Adrian Podoleanu. Not only did he build and lead the NETLAS consortium that supported my PhD, but he was also a patient teacher, a cheerful group leader, and an exceptional supervisor. He always found time to help—whether it was guiding me through the administrative chaos of Brexit or tackling exciting scientific challenges.

I am also deeply grateful to my industrial supervisor, Dr. Patrick Bowen Montague, who gave me the opportunity to embark on this adventure when I was a young intern in Bordeaux, eager to explore the world while barely speaking English. Your patience, kindness, and steady support throughout this journey were a rare gift. I aspire to become the kind of manager you have been to me.

I extend my thanks to my colleagues at NKT Photonics—Poul Varming, Ole Bang, Dung-Han Yeh, Jakob Hauge, Angelo Manetta, Erik Nicolai Christensen, Yi An, and Solveig Perret—for making NKT a friendly and lively workplace. A special thanks goes to Rasmus Dybbro Engelsholm: for your scientific enthusiasm, your patient mentoring, and the many passionate board game nights. Winning a game against you remains one of my proudest achievements! Because it can be hard to be a small fish in a big pond, I am especially thankful to my fellow PhD students Anamika Nair and Andrea Pertoldi. You were fantastic companions for discovering Denmark, sharing excitement, and relieving stress through intense badminton and squash sessions.

Across the sea, I would like to thank my colleagues at the University of Kent: George Dobre, Adrian Bradu, and Ramona Cernat for your expertise and kindness; Manuel Marques for the great coffee and running sessions; Gopika Venugopal for the amazing Indian food; René Riha for your scientific rigour; and Lucy Abbott and Adrian Fernandez Uceda for your delightful craziness. Although I went to the UK to discover different cultures, I was happy to meet another Frenchman—Julien Camard. Thank you for using your boundless energy to organize so many events, and for your kindness and constant joy.

I was also very fortunate to collaborate closely with Alejandro Martinez Jimenez, whose research aligned so well with mine. Thank you for the time we spent together—whether designing OCT systems in the lab or laughing in Canterbury's many pubs. Your kindness, scientific curiosity, honesty, and ingenuity continue to inspire me.

I was fortunate to receive support for my PhD from the Marie Curie ITN, through the European Commission (NETLAS-860807). I am also grateful to every contributor to the network, from whom I learned a lot. In particular, I would like to thank Marie Klufts and Philipp Tatar-Mathes, with whom I had a lot of fun organizing events and exploring the many countries we visited.

A special word of thanks to Simon Boivinet, the man who first introduced me to the world of lasers. Thank you for sharing your passion and for encouraging me to travel abroad and begin this incredible journey.

Most importantly, I thank my parents Muriel Riout, Olivier Grelet and siblings Vassily and Mona, whose unwavering support sustained me—even across international borders.

Finally, to my wonderful wife Louise Ferreol—thank you for leaving everything behind to join me in this crazy project, and for walking with me through each step of the way. This achievement is as much yours as it is mine.

Thank you !

Contents

List of Figures

List of Tables

List of Abbreviations

AOM	**A**cousto-**O**ptic **M**odulator
ANDi	**A**ll-**N**ormal **Di**spersion
CFBG	**C**hirped **F**iber **B**ragg **G**rating
CMSI	**C**omplex **M**aster **S**lave **I**nterferometry *(recently renamed **C**omplex **L**eader - **F**ollower **I**nterferometry)*
FFT	**F**ast **F**ourier **T**ransform
FWHM	**F**ull **W**idth at **H**alf **M**aximum
FD-OCT	**F**ourier-**D**omain **O**ptical **C**oherence **T**omography *(also **F**requency-**D**omain **O**ptical **C**oherence **T**omography, equivalent)*
GDD	**G**roup **D**elay **D**ispersion
GNLSE	**G**eneralised **N**on**L**inear **S**chrödinger **E**quation
GVD	**G**roup **V**elocity **D**ispersion
MI	**M**odulation **I**ntensity
OCT	**O**ptical **C**oherence **T**omography
OPD	**O**ptical **P**ath **D**ifference
OWB	**O**ptical **W**ave **B**reaking
PCF	**P**hotonic **C**rystal Fibre
PMI	**P**olarization **M**odulation **I**ntensity
RIN	**R**elative **I**ntensity **N**oise
SCG	**S**uper**c**ontinuum **G**eneration
SD-OCT	**S**pectral-**D**omain **O**ptical **C**oherence **T**omography *(equivalent to **Sp-OCT** , **Sp**ectrometer-based **OCT**)*
SMF	**S**ingle-**M**ode Fibre
SNR	**S**ignal **N**oise **R**atio
SOA	**S**emiconductor **O**ptical **A**mplifier
SPM	**S**elf **P**hase **M**odulation
SS-OCT	**S**wept **S**ource **O**ptical **C**oherence **T**omography
TD-OCT	**T**ime-**D**omain **O**ptical **C**oherence **T**omography
TSSC	**T**ime-**S**tretched **S**uper**C**ontinuum

List of Symbols

Symbol	Name	Unit
B	Electrical Bandwidth	Hz (or s^{-1})
c	Speed of light in vaccum	$\mathrm{m\,s}^{-1}$
D	Dispersion Parameter	$\mathrm{s\,m}^{-1}\,\mathrm{m}^{-1}$
d	Distance	m
e	Elementary charge	C
f	Frequency	Hz (or s^{-1})
k	Wavenumber	m^{-1}
n	Refractive index	no unit
P	Power	W
R	Reflectivity	no unit
S	Spectral Power Density	$\mathrm{W\,m}^{-1}$
t	Time	s
z	Distance	m
α	Optical loss	no unit
β	Propagation Constant	$\mathrm{rad\,m}^{-1}$
γ	Nonlinear parameter	$\mathrm{rad\,W}^{-1}\,\mathrm{m}^{-1}$
η	Stretching Efficiency Factor	$\mathrm{s\,m}^{-1}\,\mathrm{dB}^{-1}$
θ	Angle	rad (or $^\circ$)
Λ	Photonic Crystal Fiber Hole-to-hole Pitch/Grating Period	m
λ	Wavelength	m
ρ	Photodetector Responsivity	$\mathrm{A\,W}^{-1}$
σ	Background noise	A
ϕ	Phase	rad
ω	Angular Frequency	rad

Introduction

Project Motivation

SWEPT-source optical coherence tomography (SS-OCT) is an advanced imaging technique that enables non-destructive, three-dimensional visualisation of multilayered samples. Owing to its potential for high imaging speeds, this modality of optical coherence tomography (OCT) has garnered significant interest from both researchers and clinicians. While the dominant form of OCT — spectrometer-based Fourier domain OCT — offers impressive axial resolution, it is ultimately constrained by the limited acquisition rates of spectrometers. In contrast, SS-OCT replaces the spectrometer with a swept-source laser and a photodiode, thereby shifting the speed bottleneck from the detector to the light source. This configuration enables much higher acquisition rates, as photodiodes can operate at significantly greater speeds than spectrometer arrays.

A key requirement for SS-OCT is the use of a light source capable of rapid frequency sweeping. Several technologies have been developed to meet this demand, leveraging various photonic platforms, including optical fibres and semiconductor devices [1]–[7]. While considerable progress has been made — improving imaging speeds from hundreds of kilohertz to several megahertz — achieving sweep rates in the tens of megahertz remains a considerable challenge[8]. This limitation arises primarily because most swept-source designs rely on mechanical tuning elements to achieve wavelength sweeps, and these components are inherently limited by their physical inertia. Efforts to miniaturise such devices continue, but practical constraints persist.

An alternative approach involves utilising different physical phenomena, such

as chromatic dispersion, to achieve frequency sweeping without moving parts. These sources, known as akinetic swept-sources, have demonstrated sweep rates in the hundreds of megahertz range [9], [10]. However, such sources have predominantly been implemented within telecommunication spectral bands, where mature and cost-effective components are readily available. Unfortunately, these wavelengths are unsuitable for biomedical imaging due to significant absorption by water. Given the increasing demand for ultrafast imaging in medicine, it is vital to explore the feasibility of akinetic swept-sources operating in biologically relevant spectral windows, such as around 850 nm, 1060 nm, or 1300 nm, where water absorption is comparatively low.

This thesis investigates an akinetic swept-source architecture known as the *time-stretched supercontinuum*. In this approach, an ultrashort, high-peak-power monochromatic pulse is first launched into a nonlinear medium, generating a broadband pulse known as a supercontinuum. This broadband pulse then propagates through a dispersive element with high chromatic dispersion, which introduces wavelength-dependent delays, thereby passively producing a temporal frequency sweep. Originally proposed by Moon et al. in 2006 [7], this technique was initially limited by the high noise levels intrinsic to conventional supercontinuum generation. In the early 2010s, a new method employing all-normal dispersion (ANDi) nonlinear media was introduced [11], [12], enabling the generation of low-noise supercontinuum pulses due to the dominance of coherent nonlinear processes [13]. This work builds upon these advances by exploring the feasibility of using an ANDi-based time-stretched supercontinuum as a swept-source centred at 1060 nm for biomedical SS-OCT applications.

Organisation of the Thesis

This thesis is organised into four main chapters. Chapters 1 and 2 provide the theoretical background essential for understanding the experimental work presented in Chapters 3 and 4.

• **Chapter 1** presents the historical context and fundamental principles of OCT. The three principal variants—time-domain OCT, Fourier-domain OCT, and swept-source OCT—are introduced. Special attention is given to signal processing techniques and the influence of swept-source parameters on key imaging performance metrics.

• **Chapter 2** focuses on the optical source technologies relevant to this work. It begins with a discussion on supercontinuum generation and the associated nonlinear optical phenomena, with a particular emphasis on ANDi supercontinuum sources. The latter part of the chapter reviews state-of-the-art high-speed swept-source technologies.

The experimental component of the thesis is presented in the subsequent two chapters, each detailing a specific swept-source design and its corresponding OCT imaging implementation.

• **Chapter 3** details the design and implementation of an 80 MHz time-stretched supercontinuum source. A numerical simulation framework was developed to optimise the nonlinear dynamics within the ANDi photonic crystal fibre. In addition, the dispersive stretcher—comprising long lengths of single-mode fibre—was designed and optimised. The constructed source was experimentally characterised, and its performance evaluated for high-speed SS-OCT imaging of low-scattering samples. Two OCT setups are presented: the first, a fixed-beam configuration without lateral scanning, was used to image fast-moving micrometre-scale targets mounted on a mechanical chopper; the second combines a potassium tantalate niobate (KTN) electro-optic deflector with a galvanometric scanner, enabling volumetric OCT imaging at a rate of 400 Hz.

• **Chapter 4** addresses the development of a 10 MHz swept-source for *in vivo* retinal imaging, where improved sensitivity is essential. The challenges associated with achieving both large dispersion and broad bandwidth in a compact stretcher are discussed, and the design and characterisation of a custom chirped fibre Bragg grating (CFBG) are presented. The full swept-source system, incorporating a pulse picker, was developed and evaluated. SS-OCT imaging was performed on biological tissues, including B-scans of the human thumb and volumetric scans of the retina. Despite the high-speed acquisition, key anatomical features were successfully visualised, such as the optic nerve head, foveal pit, choroid, and retinal vasculature, demonstrating the potential of the system for high-speed biomedical imaging.

• **Chapter 5** concludes the thesis by summarising the work undertaken, outlining its key achievements, and providing a perspective on future directions in time-stretched supercontinuum swept-sources and swept-source optical coherence tomography (SS-OCT).

Part I

Theory

Chapter 1

High-speed optical coherence tomography

Contents

SINCE its first publication in 1991, optical coherence tomography (OCT) became a major imaging technique [14], [15]. This method enables non-invasive volumetric imaging with a resolution and depth that filled a gap between two widely used imaging modalities: ultrasonic imaging with a large depth imaging ($>50\,\text{mm}$) but low resolution ($>50\,\mu\text{m}$) that is suitable for coarse imaging of deep areas, and confocal microscopy with a high resolution ($\sim 1\,\mu\text{m}$) but with limited imaging range ($<0.4\,\text{mm}$) optimal for precise inspection of thin samples [16]. Other imaging modalities such as MRI has greater penetration depth and even lower resolution than ultrasonic imaging, placing it further at the extreme end of the imaging modalities spectrum. For this reason, OCT became popular amongst biologists and medical practitioners. In particular, ophthalmologists appreciated the non-invasive nature of this technique and applied it to retinal imaging since 1993 [17]. This is today one of the main markets for OCT [18], [19].

Multiple improvements of the OCT performance have been made toward better axial resolution $\sim 1.2\,\mu\text{m}$, larger axial range of tens of cm, and higher sensitivity [20]. Of course, each evolution has its problems, and not all the parameters can be optimized at the same time. In recent years, a target toward higher imaging speed has been set. Using the advances in swept-source technologies, axial scan rates of a few MHz have been demonstrated [3].

In this chapter, the fundamental principles of OCT are presented together with the impact of the swept-source parameters on OCT performance. Associated signal processing methods are also explained.

1.1 Principles and techniques

Multiple facets of OCT technologies have been investigated in recent decades, using various light sources and detection systems. One can distinguish between time-domain OCT (TD-OCT) and Fourier domain OCT (FD-OCT). Within the FD-OCT, two technologies should be distinguished: classical spectrometer-based (Sb) OCT, often referred to as spectral domain (SD) OCT, and swept-source OCT (SS) OCT. SS-OCT is the technology studied in this thesis and will therefore be presented in detail. However, the operating principles of TD-OCT and SD-OCT are also introduced as they help with understanding the evolution and limitations of OCT as well as the strengths and weaknesses of SS-OCT for modern applications.

1.1.1 Original concept and time-domain OCT (TD-OCT)

OCT is based on the principle of low-coherence interferometry. The wave trains emitted by a broadband incoherent source are temporally incoherent, meaning that they maintain a fixed phase relationship over a short time. When using an interferometer to separate the wave trains in two before recombining them, interference is obtained for as long as the short length wavetrains are superimposed. The amount of overlap versus delay determines the strength of interference versus relative delay between them. The intensity modulation associated to changing the delay is measured with a photodetector and a digitizer. The modulation intensity depends on the optical path difference (OPD) between the two optical paths, and is maximum when the OPD is zero.

The first technology employing this method was published in 1991 by Huang *et al.* and called time-domain OCT (TD-OCT)[14]. It is based on a Michelson interferometer design, either in free space or fibred as presented in Figure 1.1. The light from a broadband low-coherence source is separated toward a "reference arm" containing a mirror, and a "sample arm" where each interface of the sample

scatters the light back to the interferometer. The output light field is detected using a photodiode and a digitizer (an oscilloscope for example). Interference happens when the OPD is shorter than the coherence length of the source. By axially translating (along z) the reference mirror, one can record the consecutive intensity maxima and the position in z, each corresponding to one layer interface. Each depth point of an image would correspond to a position of the reference mirror. By adding lateral scanners in the sample arm, volumetric images are obtained.

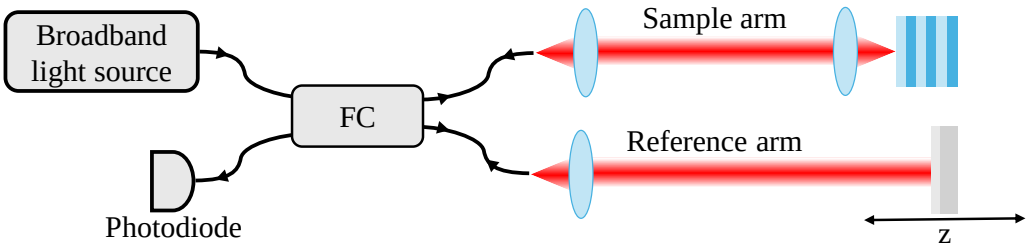

FIGURE 1.1: **Schematic of a time-domain optical coherence tomography (TD-OCT) interferometer.** FC: fibre coupler. The sample comprises multiple layers of materials with differing refractive indices.

While TD-OCT was revolutionary on multiple aspects, recording a full volume required a long time, which limited the applications. Attempts were made to answer the need for faster volume imaging, by developing faster scanning systems, but at the cost of increased complexity. Nonetheless, TD-OCT was the only marketed technology for the first 10 years [18].

1.1.2 Fourier-domain OCT (FD-OCT), a new era

In the mid-1990s, an alternative method to perform OCT measurement was presented by Fercher *et.al.* and by Hausler [21], [22]. This second generation of OCT technology measures the modulation of the reflected spectrum using a spectrometer and performing a Fourier transform to access the intensity information in

space with a fixed reference arm, see Figure 1.2 (a). Due to this step, the method is referred to as Fourier domain OCT (FD-OCT), or spectral-domain OCT (SD-OCT). As this method removes the need for reference mirror scanning, the volume acquisition is significantly faster. A fundamental sensitivity advantage compared to TD-OCT was demonstrated by Leitgeb *et al.* in 2003 [23]. This new technology popularized OCT in the industry and accelerated its deployment on the field of ophthalmology [24].

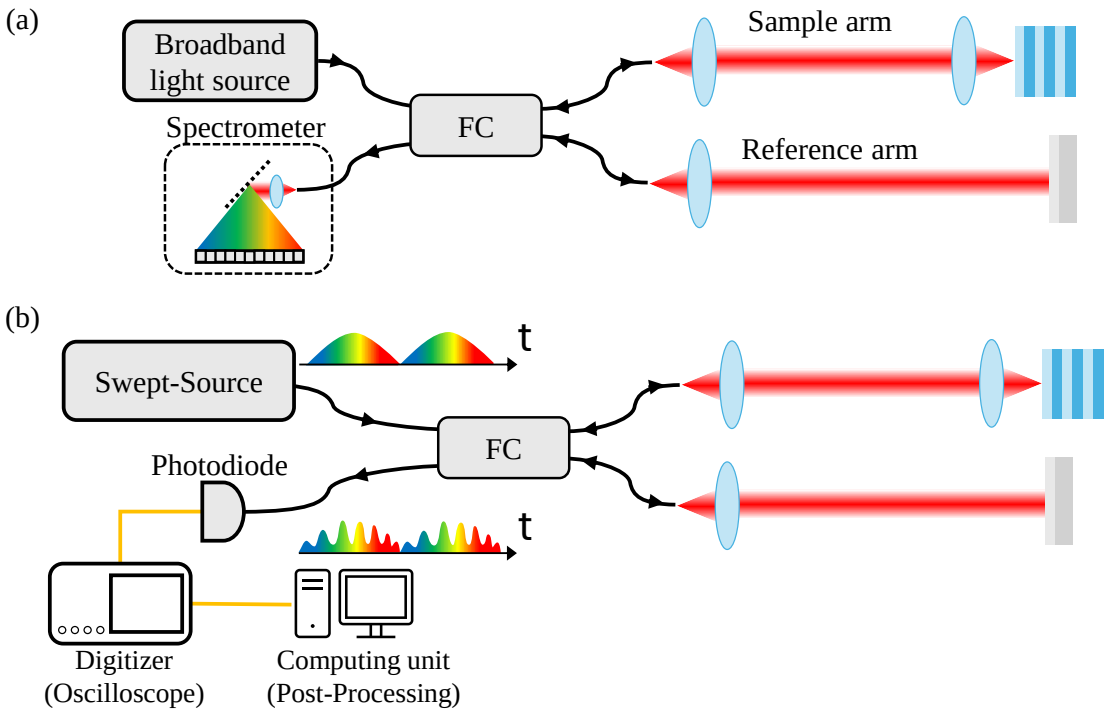

FIGURE 1.2: **Interferometer schematics applicable for (a)** SD-OCT, **(b)** SS-OCT. The scanner in the sample arm is omitted for simplicity.

The development of the spectrometer-based SD-OCT, with larger bandwidth lasers such as supercontinuum lasers enabled high resolution OCT imaging [20], [25].

However, the speed of such systems is fundamentally limited by the detection system, particularly the spectrometer electronics (typically 300 kHz) [26]. Over the past decades, only incremental improvements have been achieved, with recent developments focusing on parallelised (line-field) implementations [27]. In

many applications, higher A-scan rates are desirable, as they can reduce motion artefacts in volumetric imaging caused by sample movement [28].

1.1.3 Swept-source OCT (SS-OCT), a key for high-speed imaging

While also described in the early OCT patents, swept-source OCT (SS-OCT) was first experimentally investigated in 1996-1997 [1], [2]. The solution introduced replaces the spectrum spatial encoding of spectrometer-based FD-OCT with a temporal encoding $\omega(t)$. This peculiarity in the measurement method is enabled by a periodically wavelength-tuned laser source, also known as wavelength-swept-source or swept-source, and a high-speed photodiode as presented in Figure 1.2 (b). By linking the measured intensity time trace to the spectral sweeping of the source, the spectrum is extracted. However, the first studies were limited by the tunable laser available at the time. In the mid-2000's, new developments in high-speed swept-sources enabled a significant increase in A-Scan speed, reaching 1 million A-Scans per second, a speed increase of x100 [3], [29].

Due to the acquisition speed of a single photodetector now reaching 100 GHz, being significantly faster than the speed of spectrometer (100 kHz), faster OCT imaging became possible, reaching the MHz range. However, the complexity is transferred from the detector to the light source, requiring fast tuning. A large palette of swept-source technologies have been investigated since the invention of SS-OCT. This topic is covered in more details in the Chapter 2.

1.2 Scanning and nomenclature

The scanning methods and nomenclatures used in OCT were inherited from the ultrasound imaging community [30]. When the depth reflectivity profile is acquired at one position in x and y as presented in Figure 1.3, it is referred to as A-Scan. Adding a lateral scanner allows one to acquire multiple A-Scans along

one transversal axis, generating a B-Scan (cross section image). With a second scanner along the other transversal axis, a full 3-dimensional volume is acquired named C-Scan.

Another imaging method, known as *en face*, is obtained when scanning both lateral axes at a fixed axial position [31]. This was initially proposed to accelerate image production in TD-OCT. En-face imaging is in fact at the core of full-field OCT (FF-OCT) that uses camera to quickly produce *en-face* views. FF-OCT is particularly used for retinal imaging as it is similar to the image ophthalmologists would obtain by looking directly though the eye.

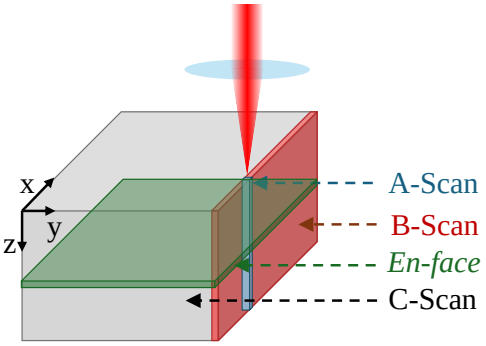

FIGURE 1.3: **OCT scanning nomenclature.** A-Scan is a 1 dimensional profile along z. B-Scan is a 2 dimensional image, composed of a set of A-Scans obtained by scanning along one lateral direction. A C-Scan is a volume composed of a set of B-Scans by scanning along the second lateral direction. An *en-face* is a 2 dimensional image in x and y, from a specific depth z.

1.2.1 Scanning devices

Multiple technological solutions have been investigated over the years to provide laser scanning. One of the most common tools is the galvanometer mirror scanner, often referred to as a galvo scanner. A voltage is applied to the scanner to rotate the mirror up to a desired position. A pair of galvo scanners can be used to provide point scanning along the two dimensions (flying spot technology

as opposed to full field). The major advantage of a galvo scanner is that it provides precise positioning, linear scanning speed and can be held at one position if needed. However, the scanning rates are limited to below 1 kHz.

One specific type of galvo scanner is the resonant scanner, that is able to reach scanning speeds up to 16 kHz. Nonetheless, the operation is more restricted than the galvo scanner, requiring uninterrupted scanning and exhibiting non-linear scanning speed at the edges of the scanned line. Often paired with a galvo scanner, such scanning heads are efficient tools to perform high-rate lateral scanning.

As the ratio of sweep frequency to that of lateral scanning gives the number of A-scans in a volume, for a 1 MHz swept-source, 1000 A-Scans are obtained using a lateral scanning of 1 kHz. If sweeping increases to 100 MHz, the number of A-Scans is too large even when using fast resonant scanners, resulting in significant oversampling. For such cases, electro-optical crystal deflectors are a better solution [32]. Using a high voltage signal to change the refractive index of the material, the beam is deflected along one axis. By applying a sinusoidal signal, a KTN crystal, as presented in Chapter 3, periodically scans over a line at rates >100 kHz. However, such scanners are expensive due to the crystal, special optics to shape the beam, and the high voltage driver.

1.2.2 Scanning patterns

Scanning patterns have been extensively studied and optimized for multiple applications [33], [34]. Some methods, such as Hilbert or Lissajous patterns, have benefits in term of covering and precision, but increase the complexity of the scanners, precise control on both axes and sacrificing scanning speed.

In this thesis, we focused on the raster scanning method, that is fast and simple to implement. It benefits from having two scanner with significantly different speed rates, such as one galvo scanner on the slow axis and a resonant scanner or electro-optical crystal deflector on the fast scanning axis.

1.3 Signal processing

1.3.1 OCT signal

The power spectral density S(k) of a light source is commonly expressed in wavenumber k=$2\pi/\lambda$ within the OCT community, due to its relationship to the spatial depth parameter z. The signal of the interferogram $I_D(k)$ measured from a sample with N reflectors is:

$$\begin{aligned} I_D(k) = &\frac{\rho}{4} S(k) \left(\alpha_R R_R + \alpha_S \sum_{n=1}^{N} R_{Sn} \right) \quad \text{“DC Terms”} \\ &+ \frac{\rho}{2} S(k) \sum_{n=1}^{N} \sqrt{\alpha_R R_R \, \alpha_S R_{Sn}} \cos\left[2k(z_R - z_{Sn})\right] \quad \text{“Cross-correlation Terms”} \\ &+ \frac{\rho}{4} S(k) \sum_{n \neq m=1}^{N} \alpha_S \sqrt{R_{Sn} R_{Sm}} \cos\left[2k(z_{Sn} - z_{Sm})\right] \quad \text{“Auto-correlation Terms”}. \end{aligned} \tag{1.1}$$

where ρ is the photodetector responsivity in A/W, R_R is the reflectivity of the reference arm and R_{Sn} the reflectivity of the sample's n^{th} interface, α_R and α_S the optical loss in the reference and sample arm, and z_R, z_{Sn} the axial depth of the reference or sample n^{th} interface.

In practice the intensity of the light collected from the reference arm is larger than the that of the sample arm, making $R_R >> R_{Sn}$ which makes the auto-correlation terms negligible and simplifies the DC and cross-correlation terms, leading to:

$$I_D(k) = \frac{\rho}{2} S(k) \left(\frac{1}{2} \alpha_R R_R + \sum_{n=1}^{N} \sqrt{\alpha_R R_R \, \alpha_S R_{Sn}} \cos\left[2k(z_R - z_{Sn})\right] \right) \tag{1.2}$$

1.3.2 Signal extraction

The photodetected signal digitised by the oscilloscope records the temporal intensity fluctuations $I_D(t)$. The acquired data are first separated into individual

sweeps and subsequently converted into the spectral domain in wavenumber. To isolate each A-scan, an initial time point is selected to discard the first incomplete sweep, and the temporal data are segmented according to the source sweeping rate.

To convert the temporal data into spectral data, several approaches may be employed. One approach consists in measuring the time-to-wavenumber mapping $k(t)$ of the swept-source, and apply this mapping to each A-Scan, yielding $I_D(k)$. This procedure assumes that the swept-source is sufficiently stable for the mapping to be considered invariant. In practice, this requires that sweep-to-sweep variations in the wavenumber mapping $k(t)$ induce a phase error $\delta\phi$ that remains well below the noise floor (typically < 0.1 rad), ensuring that a single calibration function can be reused without degrading OCT image quality or phase-sensitive measurements [35], [36]. Another method is to perform phase measurement to calibrate every sweep during the imaging.

To improve the shape of the A-Scan signal, a common practice in OCT is to apply a window on the spectral data. The impact of this process, referred to as apodization, depends on the Fourier transform of the window function. In order to remove side pulses, a Gaussian function is commonly used. If the target is to obtain a better axial resolution, a Hanning or a Hamming function can be used, at the expense of a worst suppression of the side lobes.

Due to the finite optical power in both arms of the interferometer, the detected signal contains a low-frequency component, commonly referred to as the DC component (see Figure 1.4 (d)). As defined in Eq.1.1, this contribution is given by $\frac{\rho}{4}\, S(k) \left(\alpha_R R_R + \alpha_S \sum_{n=1}^{N} R_{Sn}\right)$, and arises from the self-interference (intensity) terms of the reference and sample arms. These terms are independent of the optical path length differences and therefore do not encode depth-resolved information.

In the wavenumber domain, this contribution follows the source spectrum $S(k)$ and appears as a slowly varying, low-frequency component compared to

the oscillatory cross-correlation terms, which contain cosine modulations proportional to the optical path differences. Since the reference arm power is typically much larger than the sample arm power $R_R >> R_{Sn}$, the DC component is dominated by the reference intensity and can significantly exceed the amplitude of the interference signal.

As a result, this low-frequency component reduces the effective dynamic range and can obscure the depth-encoded information. Consequently, it is a standard practice to suppress it using high-pass filtering, either in hardware or through digital post-processing.

Alternatively, a balanced photodetector can be employed to suppress the DC component of the interference signal. In this configuration, the optical signal is split equally and directed onto two photodiodes. The resulting photocurrent is subtracted electronically, cancelling the common-mode DC background while preserving the modulated interference fringes. This differential detection not only removes the need for post-detection filtering to isolate the AC component, but also increases the effective dynamic range of the detection system. Additionally, it significantly reduces sensitivity to relative intensity noise (RIN), which is common in broadband and swept-source light sources. However, in practical implementations, residual DC content may persist due to imperfections in optical splitting or detector mismatch. In such cases, the application of a high-pass filter may still offer performance benefits by further attenuating the residual DC component.

1.3.3 Fourier transform processing

The depth information of the A-Scan lies in the frequency of the cosine in Eq.1.2. It is therefore natural that the classical processing to obtain the A-Scan signal is to perform a fast Fourier transform (FFT) on the data in wavenumber. Indeed, the wavenumber k is a Fourier pair with the depth information z. Each frequency in

the channelled spectrum becomes a peak along the spatial axis z, with low frequency leading to a peak near 0 and high frequency generating peaks at larger depths. When applied, the FFT generates data to both positive values and negative values of the spatial axis, leading to a "mirror image". For this reason, most applications use only the data on the positive depths, as presented in Figure 1.4 (d).

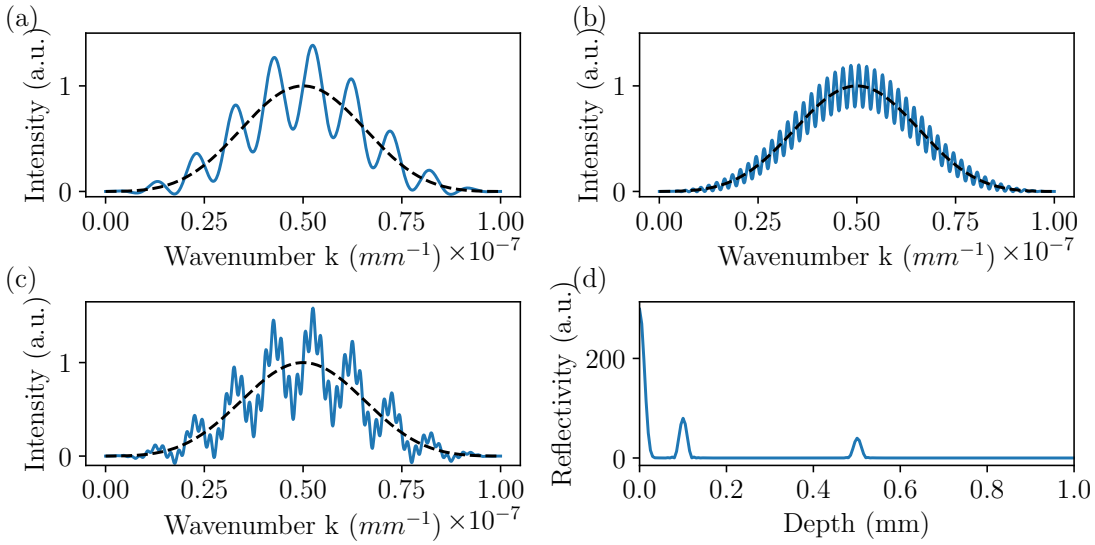

FIGURE 1.4: **OCT Processing**. **(a)-(b)** Channelled spectrum for interfaces respectively at low and high OPD. The black dashed curve is the DC function, here a Gaussian. **(c)** Channelled spectrum for two interfaces. **(d)** A-Scan after FFT processing of the channelled spectrum in (c)

For FFT processing to operate correctly, the wavenumber data need to be resampled. Indeed, when converted from time to wavenumber, the spacing between the datapoint might not be constant in wavenumber. Therefore, a new array is generated to linearize the wavenumber array, obtaining equally spaced datapoint. This additional processing step adds complexity that can slow down the image production. For this reason, using a swept-source with linear sweeping in k is strongly beneficial.

1.3.4 Master slave processing

Parallel to FFT processing, a second method was developed. Master Slave (MS) processing does not use Fourier transform to produce the A-Scan. Instead, the signal processed is compared with a basis of eigenvalues corresponding to each depths. Prior to the imaging, a calibration is performed to record these values, also known as "masks", using a mirror as a highly reflective sample. A matrix is built, containing the masks at each depth. During the imaging, the signal is compared to each mask via a correlation with the matrix, providing high A-Scan intensity when the periodicity in the measured signal matches that of the mask and low intensity when it is different as seen in Figure 1.5.

$$A(z)^{\text{CMS}} = |M \cdot E| = \begin{bmatrix} M(z_1,k_1) & M(z_1,k_2) & \cdots & M(z_1,k_N) \\ M(z_2,k_1) & M(z_2,k_2) & \cdots & M(z_2,k_N) \\ \vdots & \vdots & \ddots & \vdots \\ M(z_Q,k_1) & M(z_Q,k_2) & \cdots & M(z_Q,k_N) \end{bmatrix} \cdot \begin{bmatrix} E(k_1) \\ E(k_2) \\ \vdots \\ E(k_N) \end{bmatrix} \tag{1.3}$$

The number of points along the depth axis therefore corresponds to the number of masks.

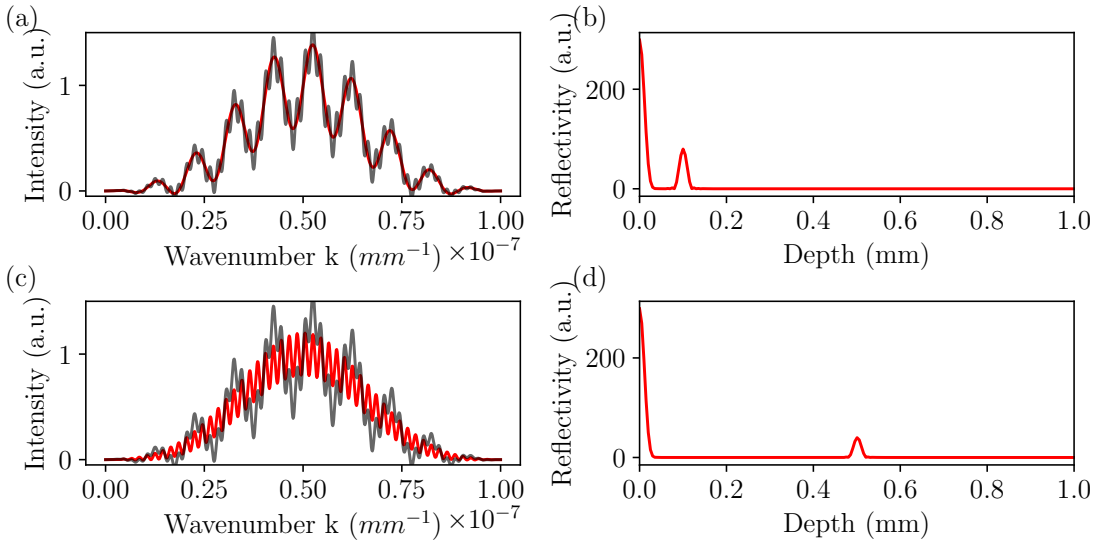

FIGURE 1.5: **Master Slave processing concept. (a,c)** OCT signal (black) and mask signal (red) for low and high OPD. **(b,d)** Resulting A-Scan after convolution with the mask.

In the initial version of MS processing, all the masks used to process the volumes were manually acquired by translating the mirror in the reference arm in steps by a fixed distance. This led to long precalibration of the instrument, and limited number of masks. A solution proposed was to produce *en face* images using only a few masks at a depth of interest, but this requires some prior knowledge of the sample.

In order to simplify the production of volumes, complex master slave (CMS) processing was developed [37]. Here, from only a few channelled spectra acquired, separated by a known distance, any number of masks are produced. By extracting the phase of each mask, two phase parameters g and h are extracted, respectively representing the phase change with depth and the fixed residual phase:

$$\phi(z,k) = g(k)z + h(k) + \phi_{rand} \tag{1.4}$$

where ϕ_{rand} is a possible random phase shift between the measurements, and z the path length difference in the interferometer arms. Using g and h, a set of masks is synthesized. This method enables fast calibration with the generation of numerous masks, for an A-Scan production both fast and with high-resolution.

Compared to the classical FFT processing method, CMS provides similar performance in term of axial resolution and sensitivity. However, it has been demonstrated that CMS processing is highly beneficial when the number of points in the A-Scan is limited, with up to x100 faster processing [38].

1.4 Parameters and impact of the swept-source

The properties of the swept-source have a direct impact on the OCT imaging performance. They are detailed here and summarized in the Figure 1.6.

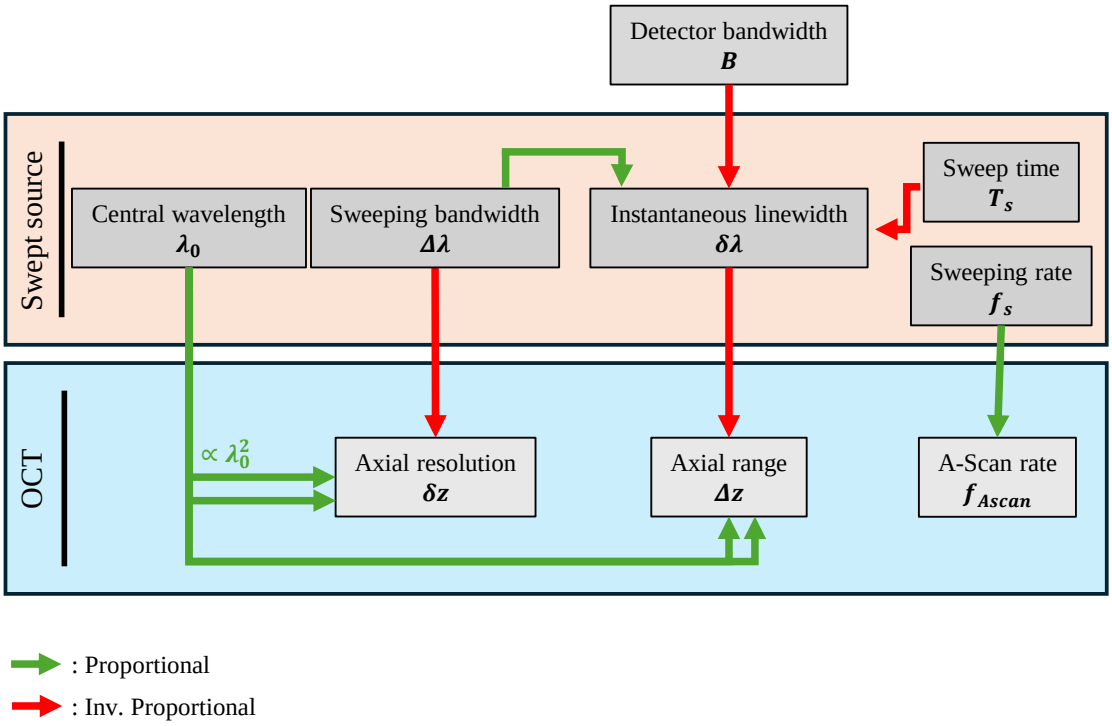

FIGURE 1.6: **Relationship between the swept-source parameters and OCT performance.**

1.4.1 Axial resolution

Due to the Fourier transform properties, the axial resolution δz is closely linked to the swept-source spectral properties. Assuming a Gaussian spectrum, the axial resolution is:

$$\delta z = \frac{2 \cdot ln(2)}{n \cdot \pi} \frac{\lambda_0^2}{\Delta\lambda} \tag{1.5}$$

with n the refractive index of the material, λ_0 the central wavelength of the swept-source, $\Delta\lambda$ the full-width half-maximum (FWHM) of the tuning bandwidth. From this equation, one understands that the larger the sweeping bandwidth, the better the resolution, i.e. more details can be imaged. We can note that the axial resolution is also proportional to the square of the central wavelength, the shorter the wavelength, the better the axial resolution.

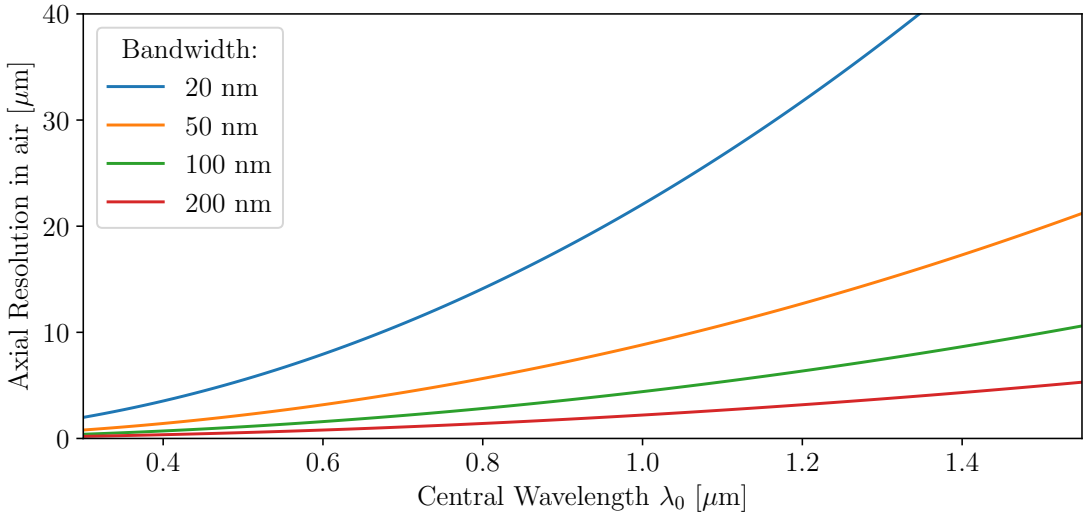

FIGURE 1.7: **SS-OCT axial resolution in the air**, for various sweeping bandwidth and central wavelength, assuming a Gaussian spectrum.

1.4.2 Axial range

If the spectral bandwidth of the swept-source could be measured instantaneously at a time t, the value then measured would be significantly smaller than the sweeping bandwidth. This value, named instantaneous linewidth $\delta\lambda$, is linked to the axial range Δz of the OCT system:

$$\Delta z = \frac{\lambda_0^2}{2 \cdot \delta\lambda} \tag{1.6}$$

The smaller the linewidth is, the larger the axial range, and therefore the deeper the OCT system can image. The "instantaneous" linewidth is generally a theoretical concept, as truly instantaneous measurement are not feasible in most cases. In practice, the linewidth depends both on the sweeping mechanism and on the detection sampling rate. Assuming a linear sweeping performed in a sweep duration of Δt_s over a bandwidth of $\Delta\lambda$, the linewidth is calculated as:

$$\delta\lambda = \frac{\Delta\lambda}{2B\Delta t_s} \tag{1.7}$$

with B the electrical bandwidth of the detection system.

While Δz defines the maximum axial imaging range of the system, both spectrometer-based OCT and swept-source OCT are subject to axial signal decay: the intensity of the A-Scan typically decreases with increasing OPD. This phenomenon, also known as *roll-off*, is directly linked to the spatial overlap between the optical pulses returning from the reference and sample arms. As the OPD increases, this overlap diminishes, resulting in a corresponding reduction in the visibility of the interference fringes. By convention, the axial range of a Fourier-domain OCT system is often defined as the depth at which the A-Scan signal drops by 6 dB, corresponding to a factor of two reduction in the field amplitude (or a factor of four in intensity).

A second critical factor influencing imaging depth in optical coherence tomography (OCT) is absorption within the sample. For an OCT signal to be detected from deeper layers, light must first propagate through the tissue, undergo backscattering towards the sample surface, and subsequently be collected by the detection system. Consequently, substantial optical absorption attenuates the signal and limits the effective imaging depth. In biomedical OCT, three principal spectral windows are commonly utilised—centred around 850 nm, 1060 nm, and 1300 nm—owing to local minima in water absorption at these wavelengths. These regions offer a favourable trade-off between scattering and absorption, thereby enabling improved penetration depth and image contrast in biological tissues.

1.4.3 A-Scan rate

Another important parameter in SS-OCT is the A-Scan rate, denoted f_{A-Scan}. This defines how many axial scans (A-Scans) the system acquires per second and plays a critical role in determining both the imaging speed and the temporal resolution of the system. In swept-source systems, the A-Scan rate is directly tied to the sweep rate f_s of the laser source.

In the ideal case of a 100% duty cycle—where the laser is continuously sweeping across its entire spectral range without any dead time between sweeps—the A-Scan rate is simply given by:

$$f_{\text{A-Scan}} = f_s = \frac{1}{\Delta t_s}, \tag{1.8}$$

where Δt_s is the time taken to complete one spectral sweep.

A higher A-scan rate enables faster image acquisition, which is especially important in applications where motion artefacts need to be minimised, such as in ophthalmic imaging or in vivo microscopy.

However, increasing the A-scan rate comes with trade-offs. As the sweep rate increases, the time available to sample each spectral point decreases, which may limit the system's axial resolution if not properly managed.

1.4.4 Lateral resolution

The lateral resolution in optical coherence tomography (OCT) is primarily determined by the spot size of the focused Gaussian beam. As a result, it depends on the central wavelength of the light source, λ_0, and the optical elements used to focus the beam. Based on Abbe's criterion, the lateral resolution δx can be approximated by [39]:

$$\delta x \approxeq 0.61 \frac{\lambda_0}{NA} \tag{1.9}$$

where NA is the numerical aperture of the objective lens. One important aspect to note is that the lateral resolution does not depend on the specific tuning characteristics of the swept-source laser, but rather on the focusing optics. A higher numerical aperture results in a smaller spot size, and therefore better lateral resolution.

However, this improvement comes at a cost. As the NA increases, the depth of

focus (DoF)—the axial distance over which the beam remains sufficiently focused—becomes smaller. For a Gaussian beam, the DoF is defined as twice the Rayleigh range, z_R, and can be expressed as:

$$DoF = 2z_R = \frac{2\lambda_0}{NA^2} \tag{1.10}$$

This inverse relationship means that although increasing NA improves lateral resolution, it also reduces the axial range over which that resolution is maintained. In practice, this introduces a trade-off: a system optimised for high lateral resolution will have a shallower depth of focus, which may not be ideal for imaging thicker samples. Therefore, system design often involves finding a balance between these two competing factors, depending on the intended application.

1.4.5 Noise and sensitivity

In imaging technologies, the sensitivity describes the capacity of the system to detect small signals. It depends mostly on the noise of the system. The parameter of reference used is the signal-to-noise ratio (SNR), calculated as the ratio of the OCT output signal over the background noise of the system:

$$SNR = \frac{I_{RMS}^2}{\sigma_{bg}^2} = \frac{I_{max}^2}{2\sigma_{bg}^2} = \left(\frac{\rho P_0 M \sqrt{\alpha_R \alpha_S R_R}}{\sqrt{2}\sigma_{bg}} \right)^2 \tag{1.11}$$

where P_0 is the average optical power, $M = \Delta\lambda_{sweep}/\delta\lambda$ is the number of sampling points per sweep, σ_{bg}^2 is the background noise variance, comprising the detection system electronic noise, the shot noise and the excess photon noise, as:

$$\begin{aligned} \sigma_{bg}^2 &= \sigma_{elec}^2 + \sigma_{shot}^2 + \sigma_{excess}^2 \\ \sigma_{elec}^2 &= NEC^2 \cdot M \cdot B = (NEP \cdot \rho)^2 \cdot M \cdot B \\ \sigma_{shot}^2 &= M 2e\rho P_0 \alpha_R R_R \cdot B \\ \sigma_{excess}^2 &= M \cdot RIN \left[\rho P_0 \alpha_R R_R\right]^2 \cdot B \end{aligned} \tag{1.12}$$

where NEC is the noise equivalent current in $A/\sqrt{Hz}$, RIN is the relative intensity noise in $1/\sqrt{Hz}$, B the electrical bandwidth of the detector, e the elementary charge. The electronic noise σ_{elec} depends on the photodetector and on the digitizer used. As the electronic bandwidth increases, the noise also augments drastically. There is therefore a balance between imaging speed and sensitivity.

The two other sources of noise depend on the swept-source and the system's attenuation. The shot noise σ_{shot} is a fundamental limitation linked to the quantum noise of the photons. It increases linearly with the optical power. Increasing the power, excess photon noise σ_{excess} is manifest, when the photodetection statistics deviates from Poisson to Bose Einstein. In addition, linked to power fluctuations in the light source, excess photon noise is produced adding to the shot noise. Due to its quadratic dependence on the optical power, this noise is dominant at high power operation.

The sensitivity is commonly measured by using a totally reflective sample (a mirror) and introducing increasing attenuation in the sample arm of the interferometer until the SNR equals 1. Commonly expressed in decibel, the sensitivity S is calculated as:

$$S[dB] = SNR[dB] - Att[dB] \tag{1.13}$$

with Att the attenuation of the light scattered back from the sample until the photodetector. For a shot-noise limited sensitivity, the calculation becomes:

$$S_{shot}[dB] = 10log\left(\frac{\rho PT}{e}\right) - Att[dB] \tag{1.14}$$

where ρ is the detector responsivity, typically $\sim 0.7\,A/W$ at 1060 nm, P is the average power, T the sweeping period. This equation clarifies the fundamental inverse relationship between imaging speed and sensitivity, constrained by shot-noise limitations.

In practice, however, this expression represents an upper bound that is not

fully reached in real systems. Additional noise contributions, such as relative intensity noise of the source, detector and electronic noise, as well as non-ideal interferometric efficiency and optical losses, lead to a degradation of the measured sensitivity. Typically, experimental sensitivities are found to be on the order of 5 to 15 dB below the shot-noise limit, depending on the system design and operating conditions, with optimised configurations approaching this limit within a few decibels. Thus, the design of each OCT system must achieve an optimal compromise tailored to its targeted application.

1.5 Conclusion

Optical coherence tomography (OCT) has established itself as a leading non-invasive imaging modality, combining high spatial resolution with real-time acquisition capabilities. Its evolution, from the original time-domain approach to Fourier-domain methods and subsequently to swept-source OCT (SS-OCT), has been driven by the pursuit of higher imaging speeds, greater sensitivity, and broader imaging depths. Among these developments, SS-OCT has enabled a significant increase in performance; however, the technology remains fundamentally limited by the properties of the swept light source.

In practice, the design of swept-sources involves critical trade-offs between sweep-speed, tuning range, coherence length, and output power, all of which directly influence image quality and system performance. A clear understanding of these trade-offs is therefore essential, not only for optimising current SS-OCT systems but also for identifying technological gaps and guiding future research efforts aimed at overcoming these constraints.

Chapter 2

Introduction to supercontinuum and swept-sources technologies

Contents

NONLINEAR optics has led to the development of a wide range of technologies, such as ultrashort pulsed lasers or broadband light sources, which are now essential to many fields. Despite its significance, the field remains complex, as multiple nonlinear effects often occur simultaneously, influencing light propagation in intricate ways.

This chapter begins by exploring supercontinuum generation, starting with the principles of nonlinear light propagation in optical fibres and how these effects interact to shape supercontinuum dynamics. Following this, we introduce swept-source technology, with a focus on high-speed tuning mechanisms operating at megahertz rates. This discussion sets the stage for the central topic of this thesis: supercontinuum time-stretched swept-sources.

2.1 Nonlinear light propagation in fibres

The propagation of light in optical fibres is governed by linear and nonlinear phenomena. These effects act simultaneously on the light in a complex manner. However, one can discuss each phenomenon independently, to better understand its effect on the light. We will present those phenomena that are happening during the supercontinuum generation to obtain a better grasp of the critical parameters one can optimise. While the effects also occur for continuous wave propagation, the emphasis will be put on nonlinear effects during pulse propagation.

2.1.1 Attenuation

First, one can identify the material attenuation and guiding loss in a fibre. This results in a decrease of the light power along the propagation axis. Depending

on the wavelength band targeted, different material can be used to manufacture the fibre, resulting in a different attenuation spectral profile. In most single mode fibres (SMF), the guiding loss is negligible compared to the material attenuation. However, guiding losses can be significant when the fibre is bent and are a major limitation in the design of compact fibre lasers.

2.1.2 Chromatic dispersion

A second linear effect is the chromatic dispersion. It represents the refractive index n(ω) dependence on the light frequency, and therefore determines the light propagation speed through the fibre. The phase constant β is modeled by a Taylor series expansion around the pump frequency ω_0:

$$\beta = n_{eff}(\omega)\frac{\omega}{c} = \beta_0 + \beta_1(\omega - \omega_0) + \frac{1}{2!}\beta_2(\omega - \omega_0)^2 + \ldots + \frac{1}{m!}\beta_m(\omega - \omega_0)^m \quad (2.1)$$

where m=(0,1,2,3,...) and

$$\beta_m = \frac{d^m\beta}{d\omega^m}\Big|_{\omega=\omega_0} \quad (2.2)$$

For pulse propagation, the first β_1 and second β_2 order are primordial as they represent the group velocity and the group velocity dispersion (GVD). These respectively determine the propagation speed of the pulse and the distortion of a broadband pulse in the time domain. To quantify the dispersion, another parameter is commonly used, expressed in ps/nm/km:

$$D = -\frac{2\pi c}{\lambda^2}\beta_2 \quad (2.3)$$

When the parameter D is positive, the dispersion is said to be anomalous and longer wavelengths propagate slower than shorter wavelengths, as represented in Figure 2.1. When D is negative, this regime is referred to be normal and longer wavelengths travel faster than shorter wavelengths. The wavelength for which the dispersion is null is termed as the zero-dispersion wavelength.

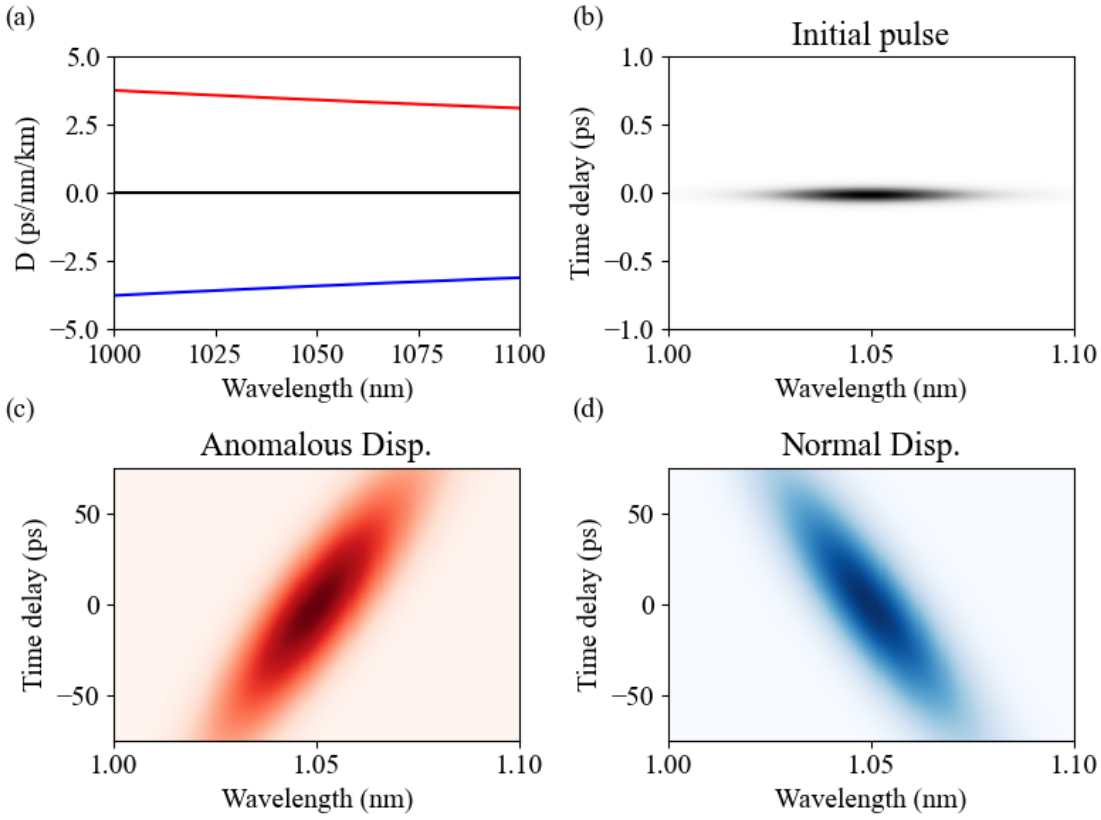

FIGURE 2.1: **(a)** Example of anomalous (red) and normal (blue) dispersion profiles, and the impact on a broadband pulse initially Fourier transform limited **(b)**, of anomalous dispersion **(c)** and normal dispersion **(d)**.

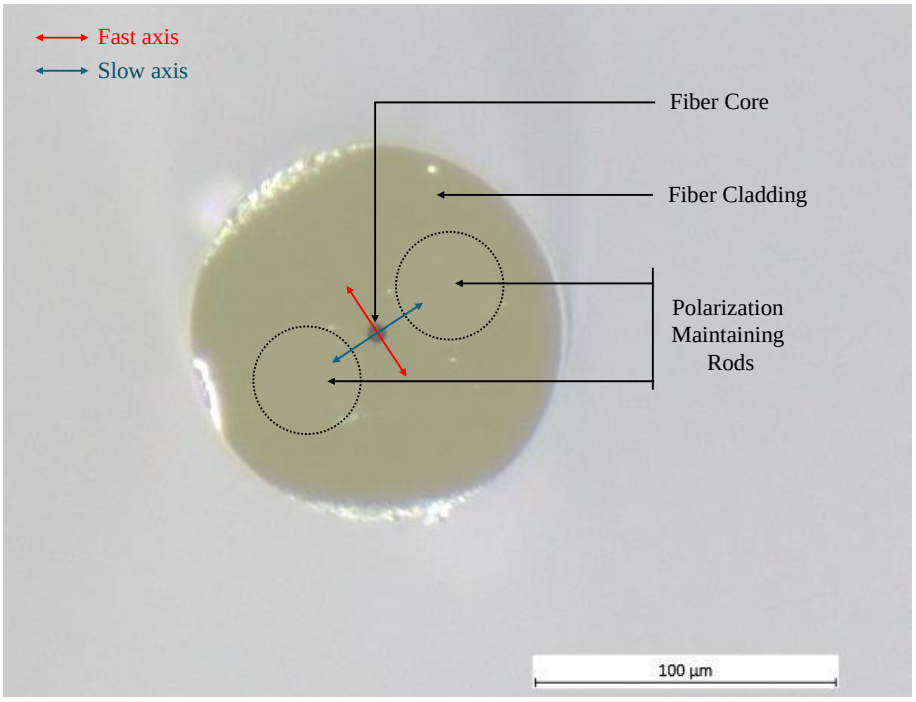

FIGURE 2.2: PM1950 from Nufern observed with a microscope, illustrating a PANDA design.

2.1.3 Birefringence

Birefringence in an optical fibre is the difference in refractive index experienced by light polarised along two orthogonal axes, leading to different propagation speeds. For this reason, these are referred to as the fast and slow axes. Birefringence can be caused by asymmetry in the fibre, but also from external effects such as heat, pressure or fibre twisting. To reduce the impact of external variations on a polarisation sensitive system, polarisation maintaining fibres are often used. These fibres are modified with asymmetric components that generate important birefringence, fixing "fast" and "slow" axes. Multiple structures exist, one popular example is the "PANDA" design that consists of two rods aligned on both sides of the core of a step index fibre that apply stress on it along this axis, creating the birefringence. This structure is presented in Figure 2.2.

2.1.4 Self-phase modulation

When dealing with high intensity light fields, nonlinear effects start to manifest. A high intensity laser pulse temporarily changes the refractive index of the material. Due to this local refractive index modification, the pulse experiences a phase change known as self-phase modulation (SPM). Let us consider a Gaussian pulse of intensity I(t):

$$I(t) = I_0 \exp(-t^2/\tau^2) \tag{2.4}$$

where I_0 is the peak intensity, τ half the pulse duration. The material refractive index n is then expressed as:

$$n(I) = n_0 + n_2 \cdot I \tag{2.5}$$

with n_0 the linear refractive index and n_2 the nonlinear index, also referred to as Kerr index. The phase ϕ can be derived:

$$\phi(t) = \omega_0 t - \frac{2\pi}{\lambda_0} \cdot n(I) L \tag{2.6}$$

where ω_0 and λ_0 are the central angular frequency and wavelength of the pulse, and L the length along which the pulse propagated in the material.

In the spectral domain, the SPM-induced phase shift generates additional frequency components, leading to a broadening of the optical spectrum

$$\omega(t) = \frac{d\phi(t)}{dt} = \omega_0 - \frac{2\pi}{\lambda_0} \cdot \frac{dn(t)}{dt} L \tag{2.7}$$

Using Eq.2.4 and Eq.2.5, the frequency modification $\delta\omega$ can then be expressed as:

$$\delta\omega(t) = \frac{4\pi n_2 L I_0}{\lambda_0 \tau^2} \cdot t \; e^{-t^2/\tau^2} \tag{2.8}$$

As Eq. 2.8 shows, the broadening efficiency of SPM is directly linked to the light intensity I_0. In the case of optical pulses propagating in a fibre, this intensity is

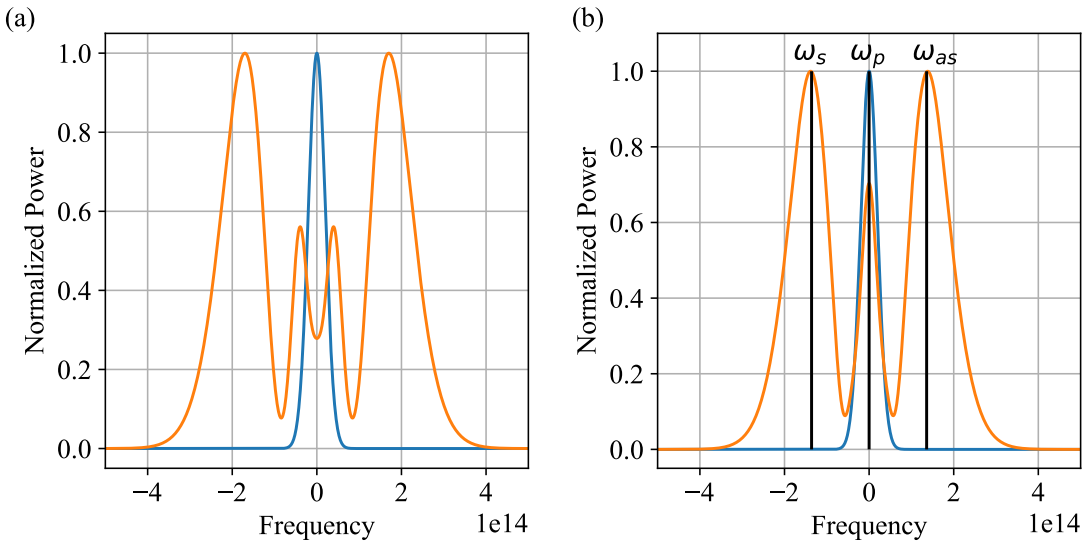

FIGURE 2.3: **Impact of nonlinear effects on the spectrum. (a)** Illustration of the spectral broadening from the SPM (orange) on a Gaussian pulse (blue). **(b)** Effect of degenerate FWM (orange) on a Gaussian pulse (blue) with pump, Stokes and Anti-Stokes frequencies. Both simulations use a 100 fs fwhm Fourier-limited Gaussian pulse with 2.5 kW peak power, propagating in 1m of optical fibre with a nonlinear parameter $\gamma = 4\,\mathrm{radW^{-1}km^{-1}}$

enhanced by both higher peak power and a stronger spatial confinement, leading to increased spectral broadening. It is interesting to note that according to Eq. 2.7, SPM is also sensitive to the pulse shape.

In a single mode fibre, the expression of the nonlinear phase shift in Eq. 2.6 can be written using the effective mode area A_{eff} and the optical power P:

$$\phi_{NL} = \frac{2\pi}{\lambda_0} n_2 \frac{P}{A_{eff}} L \tag{2.9}$$

An effective nonlinear coefficient γ (in rad/(W m)) can be introduced as:

$$\gamma = \frac{2\pi}{\lambda_0} \frac{n_2}{A_{eff}} \tag{2.10}$$

leading to a simplified expression for the nonlinear phase shift:

$$\phi_{NL} = \gamma P L \tag{2.11}$$

2.1.5 Four wave mixing

The second noticeable nonlinear effect is an interaction between photons of multiple wavelengths called four wave mixing (FWM). This describes the absorption by an electron of two photons of frequencies ω_1 and ω_2 , and re-emission of two other photons of frequencies ω_3 and ω_4 different from the two original ones, following the principle of conservation of energy:

$$\omega_1 + \omega_2 = \omega_3 + \omega_4 \tag{2.12}$$

For this effect to occur, the principle of conservation of momentum imposes a phase-matching requirement that can be expressed as follows:

$$\Delta k = (\tilde{n}_3\omega_3 + \tilde{n}_4\omega_4 - \tilde{n}_1\omega_1 - \tilde{n}_2\omega_2)/c = 0 \tag{2.13}$$

with $\tilde{n}_j$ the mode refractive index at the frequency ω_j.

Degenerate FWM happens when the two absorbed photons originates from a powerful optical wave $\omega_1 = \omega_2 = \omega_p$ (pump) and generate a photon pair at symmetrically positioned frequencies ω_s (Stokes) and ω_{as} (anti-Stokes) around the pump frequency with a frequency shift $\Omega = \omega_p - \omega_s = \omega_{as} - \omega_p$. The phase mismatch Δk of the degenerated FWM then becomes:

$$\Delta k = \tilde{n}_s\omega_s + \tilde{n}_{as}\omega_{as} - 2\tilde{n}_p\omega_p \tag{2.14}$$

The phase matching between the four waves is dependent on the dispersion, but also on the nonlinear associated index of refraction. For a single mode fibre, the phase mismatch can be expressed based on the contribution of dispersion and of the SPM:

$$\Delta k = \Delta\beta_L + 2\gamma P_0 = 2\Sigma_{m\geq 2}\frac{\beta_{2m}}{(2m)!}\Omega^{2m} + 2\gamma P_0 \tag{2.15}$$

The phase matching condition is satisfied when the linear term $\Delta\beta_L$ is compensated by the Kerr index modification $2\gamma P_0$ [40].

2.1.6 Optical wave breaking

In the regime of ultrashort pulse propagation at high peak power, the combined action of self-phase modulation and chromatic dispersion can lead to a strongly non-perturbative propagation regime known as *optical wave breaking* (OWB). This phenomenon is most prominently observed in fibres operating in the normal dispersion regime and plays a central role in the early stages of all-normal dispersion supercontinuum generation [41], [42].

Optical wave breaking originates from the intensity-dependent frequency chirp imposed by self-phase modulation. As discussed in the previous section, SPM generates a time-dependent frequency shift across the pulse, with newly created spectral components distributed symmetrically around the carrier frequency. In the presence of normal group-velocity dispersion, these frequency components propagate at different group velocities, with longer wavelengths travelling faster than shorter wavelengths. As a result, portions of the pulse carrying different instantaneous frequencies can overtake one another during propagation, leading to a temporal overlap of distinct spectral components.

This frequency-dependent velocity mismatch induces a reorganisation of the pulse in the time domain, characterised by the formation of steep temporal gradients and rapidly oscillating structures. This behaviour is closely analogous to wave breaking in hydrodynamics, where a nonlinear dependence of the wave velocity on amplitude leads to the formation of shock-like features. In the optical domain, these effects manifest as strong temporal distortions accompanied by the appearance of sidelobes and sharp features in the optical spectrum.

Although the spectral signatures associated with optical wave breaking can be interpreted as resulting from degenerate four-wave mixing between overlapping

frequency components, OWB should not be regarded as an independent four-wave mixing process. Rather, it represents a propagation regime arising from the combined influence of Kerr-induced phase modulation and dispersion, in which multiple intra-pulse frequency components interact coherently once temporal overlap is established [43], [44]. No explicit phase-matching condition is required beyond that imposed by the dispersive properties of the fibre and the nonlinear phase accumulated during propagation.

The onset of optical wave breaking marks a transition beyond the regime of purely self-similar spectral broadening driven by self-phase modulation. Once wave breaking occurs, additional spectral expansion is accompanied by irreversible temporal distortion and increased chirp. In all-normal dispersion fibres, this regime is nevertheless highly advantageous, as both SPM and OWB are coherent processes [45], [46]. When modulation instability is suppressed, optical wave breaking enables efficient and broadband spectral generation while preserving a high degree of phase coherence, which is a key requirement for low-noise supercontinuum sources.

2.1.7 Modulation instability

During propagation of an intense pulse in a single mode fibre, perturbations of the waveform generate modulations in time domain, creating new frequencies on both sides of the pump frequency. The sidebands can be amplified through degenerated FWM, leading to a scalar modulation instability (MI). The phase matching condition in an optical fibre given by Eq.2.15 requires an anomalous dispersion fibre to counterbalance the positive nonlinear phase shift.

However, a normal dispersion fibre can also experience vectorial modulation instability, known as polarisation modulation instability (PMI). PMI emerges from the interaction between two waves propagating along orthogonal polarisations. For this effect to occur, the walk-off between the two waves should be negligible, which is the case for low birefringence fibres ($\Delta n < 10^{-4}$) [47], [48]. The

pump on one polarisation axis amplifies the two sidebands on the orthogonal axis. When pumping on the fast axis, the gain on the slow axis can be expressed as [49]:

$$g_{slow}(\Omega) = |\beta_2|\sqrt{(\Omega^2 + \Omega_{c2}^2)(\Omega_{c1}^2 - \Omega^2)} \tag{2.16}$$

with $\Omega_{c1} = (4/3 \cdot \gamma\beta_2)^{1/2}\sqrt{P_0 - P_c}$ where $P_c = 3\Delta\beta_0/2\gamma$, $\Omega_{c2} = (2\Delta\beta_0/\beta_2)^{1/2}$, $\Delta\beta = \beta_{0,fast} - \beta_{0,slow}$. No PMI gain happens when the input power P0 is inferior to the power threshold P_c.

For a pump aligned to the slow axis, the gain becomes:

$$g_{fast}(\Omega) = |\beta_2|\sqrt{(\Omega^2 - \Omega_{c2}^2)(\Omega_{c3}^2 - \Omega^2)} \tag{2.17}$$

with $\Omega_{c3} = (4\gamma/3\beta_2)^{1/2}\sqrt{P_0 + P_c}$.

As it can be seen from these equations, the maximum gain on both axes strongly depends on the input power and on the birefringence. Using high birefringent fibres reduces the noise amplification from PMI [50].

In a strong birefringent fibre ($\Delta n > 10^{-4}$) with normal dispersion, cross phase modulation instability (XPMI) happens when pumping at 45° to the fibre's polarisation axes [51], generating pairs of sidebands on each orthogonal polarisation axis. XPMI depends highly on the input polarisation, and is minimized when aligned on one of the fibre polarisation axis.

2.1.8 Raman scattering

During the propagation of light in an optical fibre, photons undergo both elastic scattering (Rayleigh scattering) and inelastic scattering, primarily Raman scattering and, to a lesser extent, Brillouin scattering. In the former case, the scattered photon conserves its energy and therefore its frequency. In contrast, in Raman scattering, part of the photon energy is transferred to the silica network and converted into vibrational excitation, leading to the generation of photons with

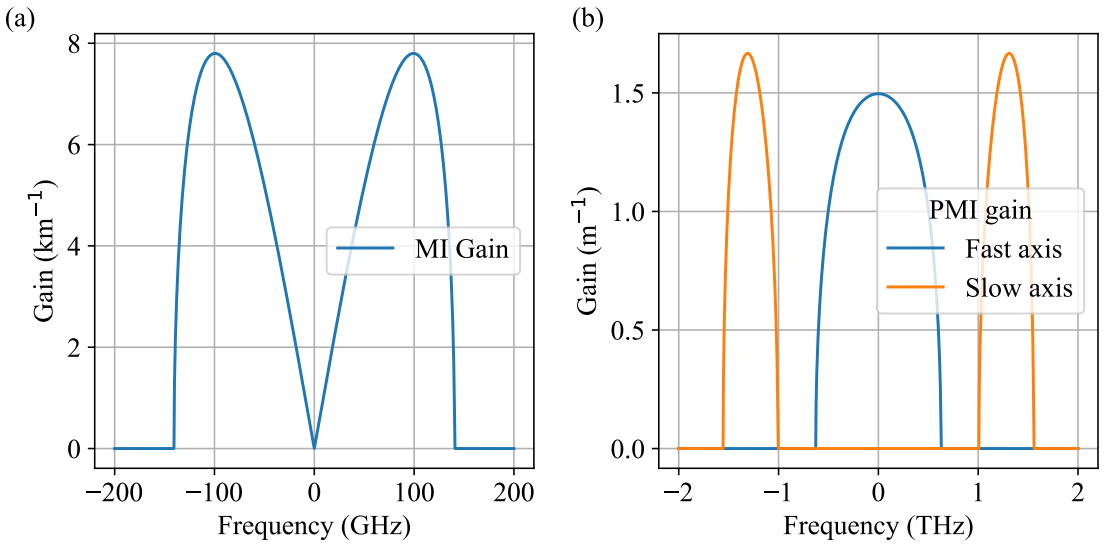

FIGURE 2.4: **(a)**Modulation instability gain. **(b)** Polarisation modulation instability gain along fast (slow) for linear input polarisation along slow (fast) axis.

downshifted (Stokes) and upshifted (anti-Stokes) frequencies. Brillouin scattering arises from the interaction of light with acoustic phonons in the medium, resulting in a much smaller frequency shift and predominantly backward scattering.

Stimulated Raman scattering (SRS) occurs when an intense pump beam at a frequency ν_p amplifies a signal at frequency ν_s, such that $\nu_p - \nu_s$ matches a vibrational frequency of the material.

In silica fibres, the Raman contribution to the nonlinear response is delayed, with a characteristic response time on the order of tens of femtoseconds. For ultrashort pulses with durations comparable to or shorter than this timescale, the Raman interaction becomes temporally nonlocal and its effective strength is reduced, particularly outside the soliton regime [52], [53]

2.2 Supercontinuum dynamics

Although the first demonstration of supercontinuum generation (SCG) in bulk glass dates back to 1970, it was not until the late 1990s with the development of high-nonlinearity fibres — referred to as photonic crystal fibre (PCF) — that the

field significantly expanded [54]–[56]. In parallel, the emergence of compound (i.e. non-silica) glass fibres, such as fluoride and chalcogenide fibres, further extended SCG towards longer wavelengths and enhanced nonlinear efficiencies.

Due to their extreme large bandwidth, supercontinuum lasers found numerous applications such as in spectroscopy [57], biomedical imaging (CARS, OCT, fluorescence microscopy and fluorescence lifetime imaging) [7], [58]–[60], and in optical fibre telecommunications [61].

In this section, the PCF structure and its characteristics are introduced to highlight why this fibre type is so attractive for the scientific community. Then we discuss the supercontinuum generation with an emphasis on all-normal dispersion (ANDi) SCG. Finally, we present the generalized nonlinear Schrödinger equation (GNLSE), a powerful tool to describe and simulate the evolution of a light pulse in a fibre.

2.2.1 Photonic crystal fibre

Photonic crystal fibres, sometimes also referred to as microstructured fibres, rely on an arrangement of microscopic holes around the fibre core to guide light. PCFs can be broadly divided into two groups: index-guiding PCFs and hollow-core fibres. In the former, the core is solid and the microstructured cladding can be treated as an effective medium with a reduced refractive index, enabling guidance by total internal reflection. If properly designed, such fibres can support only the fundamental mode over a wide wavelength range, leading to so-called endlessly single-mode behaviour [62].

In the latter case, light is guided in a hollow core. Two distinct guiding mechanisms can be identified: photonic band gap guidance and antiresonant guidance. In photonic band gap fibres, confinement arises from a forbidden frequency band in the cladding. In contrast, antiresonant fibres rely on reflection from thin glass membranes surrounding the core, without requiring a true photonic band gap

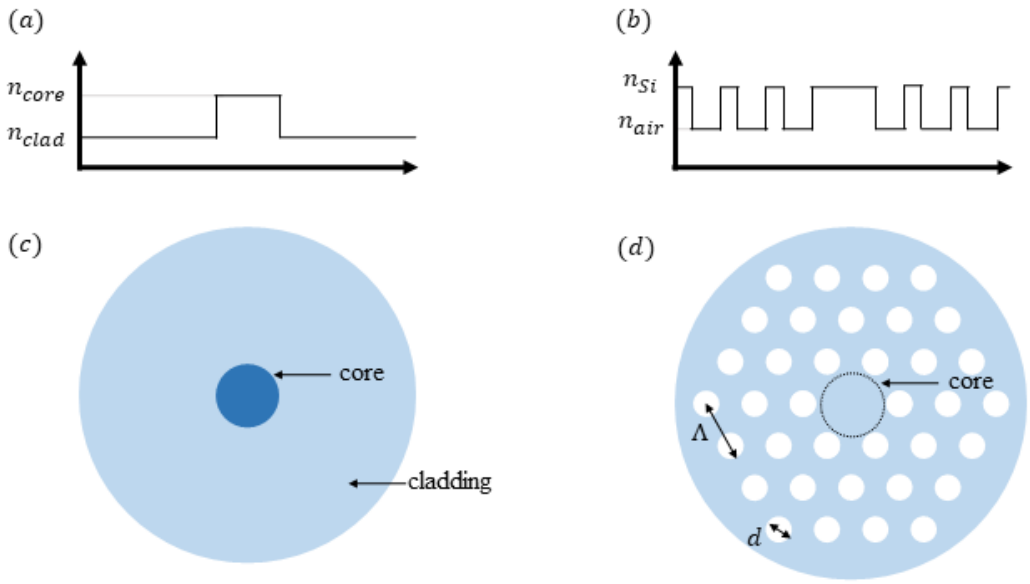

FIGURE 2.5: **Comparison of step index fibre and hexagonal solid-core PCF structures**. **(a)** and **(b)** are the refractive index profiles, **(c)** and **(d)** are structure representations.

[63]. Modern hollow-core fibres are predominantly based on this antiresonant mechanism.

Photonic crystal fibres offer a great design flexibility. Parameters such as the material used in the core, the one used in the holes, the size and distance between the holes determine a particular attenuation profile, dispersion profile, as well as an effective mode area of the fibre. Among other unique properties, PCF enable the access to high numerical aperture, increasing the nonlinearity of the fibre. The development of PCF opened the path for a thriving market in specialty fibres, uniquely designed for advanced applications in telecommunications, sensing, nonlinear optics, and high power delivery [64]–[67].

In this thesis, we focus on full silica, solid core PCF, and the holes are filled with air. A descriptive representation of such fibre is presented in Figure 2.5. The holes diameter d is considered identical for all the holes in this case. The hole-to-hole pitch Λ and the relative hole diameter d/Λ are the two parameters used in the design of the fibre. From this structural information, can be obtained in respect to the core diameter $d_{core} = 2\Lambda - d$ and, using simulation software

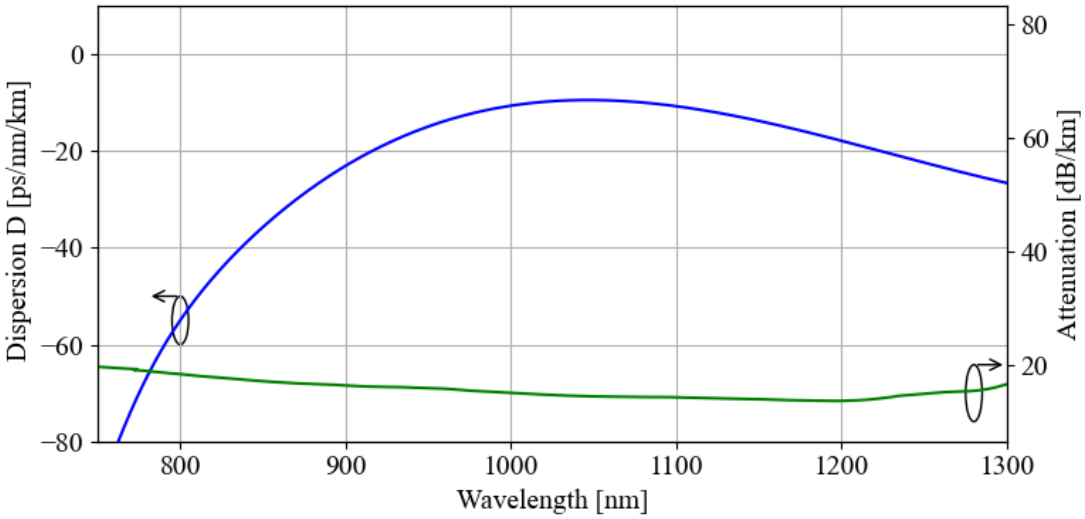

FIGURE 2.6: **Example of dispersion (blue) and attenuation (green) profile of an ANDi PCF (NL-1050-NEG-1-PM, NKT Photonics)**.

such as COMSOL Multiphysics®, the dispersion and attenuation profiles and the nonlinear coefficient.

These PCFs are critical to supercontinuum generation for two reasons. First, their high nonlinear coefficient improves the efficiency of nonlinear effects, reducing the power needed to obtain spectral broadening. Second, the dispersion could be more freely tuned, with the possibility to produce fibres with very low and flat GVD, but also fibres with all-normal dispersion (ANDi) over a large bandwidth [68]. As an example, the dispersion and attenuation of the commercially available PCF NL_1050_NEG_1-PM manufactured by NKT Photonics can be seen on Figure 2.6. This is the fibre that was used in the rest of this thesis.

2.2.2 All-normal dispersion supercontinuum generation

Introduction

Supercontinuum generation in silica fibres can be achieved by pumping next to the zero dispersion wavelength (ZDW) in the anomalous region. This is the method used in many commercial supercontinua. The initial pulse splits through soliton fission, generating the first broadening. Part of the soliton experiences

a red-shift from Raman scattering. For specific wavelengths in normal dispersion region, a phase matching condition can be met generating a dispersive wave through FWM, which broadens the spectrum toward lower wavelengths [66].

The combination of these effects enable the generation of octave spanning supercontinua [69]. However, this technique presents two major drawbacks. First, the power spectral density is not homogeneous in the supercontinuum. Indeed, a significant portion of the power is at the pump wavelength. For some power sensitive application, this remaining pump power needs to be filtered out, leading to a significant power loss. Secondly, the soliton fission is initiated through modulation instabilities. Because of this, the laser emission is highly incoherent, with a relative intensity noise typically exceeding 20% [70].

In the last decade, following the development of ANDi PCF, the generation of ANDi supercontinua raised interest [11], [12], [71]. Due to this dispersion profile, soliton do not exist. Therefore, the broadening mechanism is radically different.

ANDi supercontinuum generation dynamics

The ANDi supercontinuum generation steps are presented in Figure 2.7. The initial short pulse with high peak power experiences a symmetrical spectral broadening caused by SPM. As explained in Eq.2.8, the instantaneous phase change depends on the peak power, and the nonlinear coefficient parameter of the fibre.

Due to the normal dispersion, the higher wavelength of the pulse intermediate front propagates faster than the central wavelength of the pulse front edge. When both overlap in time, spectral broadening through optical wave breaking (OWB) is initiated, with the tail part of the pulse being converted first due to the higher dispersion on the lower wavelength, followed by the front part of the pulse. Once the OWB fully converted the pulse front and tail, further propagation only results in additional chirp, stretching the pulse in time.

ANDi supercontinuum raised interest due to two features. First, the spectrum obtained after broadening is highly flat, which ensures homogeneous power

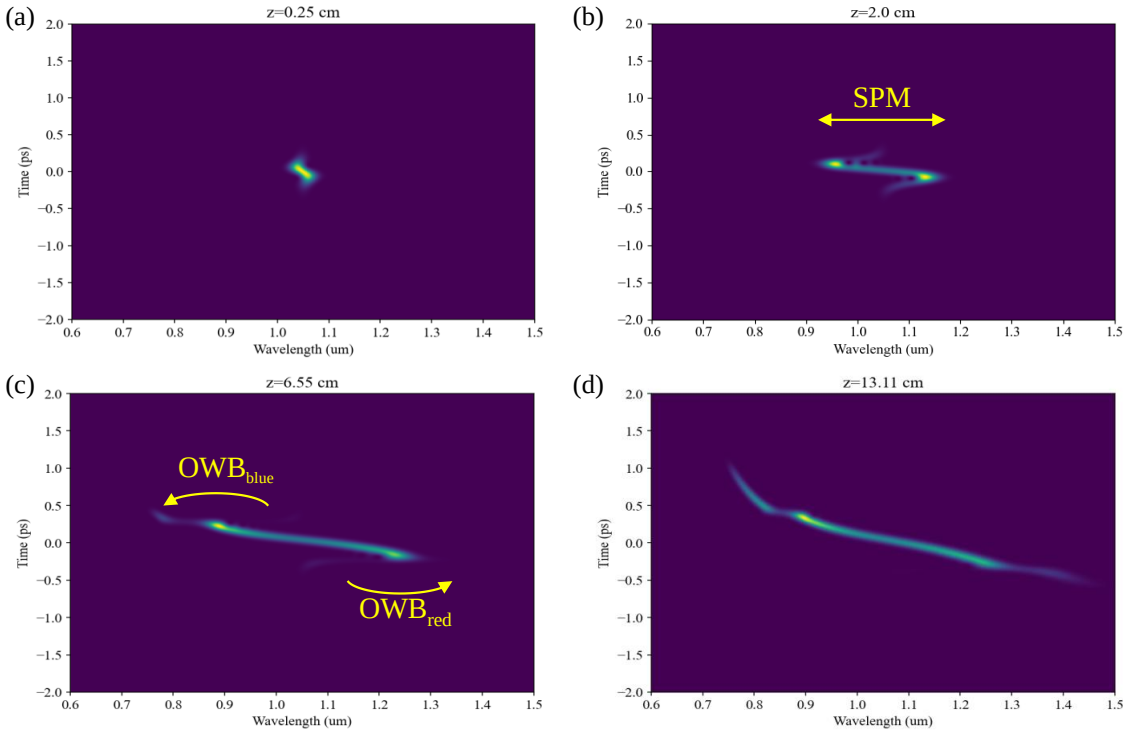

FIGURE 2.7: **All-normal dispersion (ANDi) supercontinuum generation steps**. **(a)** Initial sech-shaped transform limited pulse, **(b)** Self phase module (SPM) broadening, **(c)** Optical wave breaking (OWB) on the low wavelength side, **(d)** OWB on the high wavelength side.

spectral density across the whole bandwidth. Second, self phase modulation and optical wave breaking are two coherent mechanisms. For this reason, assuming short pulses suppressing polarisation modulation instability and cross-phase modulation instability, using a low intensity noise laser to seed the ANDi supercontinuum generation results into a low-noise supercontinuum, thus lifting one of the major limitation of supercontinuum generation for numerous applications like OCT [59], [72].

2.2.3 Numerical simulations based on the generalized nonlinear Schrodinger equation

The analysis of such a complex phenomenon with multiple entangled effects is not straight forward. Numerical simulations have been developed, based on the powerful generalized nonlinear Schrodinger equation (GNLSE):

$$\begin{aligned}\frac{\partial A(z,T)}{\partial z} = &\sum_{m\leq 2} \frac{i^{m+1}\beta_m}{m!}\frac{\partial A(z,T)}{\partial T^m} - \frac{\alpha}{2}A(z,T) \\ &+ i\gamma\left(1 + i\tau_{\text{shock}}\frac{\partial}{\partial T}\right)\left(A(z,T)\int_{-\infty}^{+\infty} R(T')|A(z,T-T')|^2 dT'\right)\end{aligned} \tag{2.18}$$

where A(z,T) is the time domain field envelope obtained by inverse Fourier transform of the complex field envelope in the frequency domain $\tilde{A}(z,\omega)$, given by:

$$A(z,T) = \frac{1}{2\pi}\int_{-\infty}^{+\infty} \tilde{A}(z,\omega-\omega_0)e^{-i(\omega-\omega_0)T}dw \tag{2.19}$$

where ω_0 is the central wavelength of the initial pulse.

The first term of Eq.2.18 describes the dispersion of the fibre, and the second its attenuation. The third term includes the nonlinear effects, with the nonlinear coefficient γ. The partial derivative is the self steepening, a dispersive effect that shortens the front end of the pulse and effectively steepens it. A characteristic value for this effect is the $\tau_{shock} = 1/\omega_0$ time scale. Finally, the last term is the

Raman response function R(t) decomposed as

$$R(t) = f_R\delta(t) + (1 - f_R)h_R(t) \tag{2.20}$$

with $\delta(t)$ the instantaneous response, $h_R(t)$ the normalized delayed response, and f_R the fractional contribution of the Raman delayed response.

The generalized nonlinear Schrödinger equation is derived under several standard approximations [49]. In particular, it relies on the slowly varying envelope approximation, assuming that the pulse envelope evolves on a timescale much longer than the optical period, which may become less accurate for few-cycle pulses. The model further assumes unidirectional propagation in a single spatial mode and neglects polarisation effects, which is justified for weakly birefringent single-mode fibres. The nonlinear response is limited to third-order effects, including the instantaneous Kerr contribution and a delayed Raman response described by a fixed material response function. In addition, the dispersion relation is approximated by a Taylor expansion around the carrier frequency, which may limit accuracy for ultra-broadband spectra. Nevertheless, within these limits, the GNLSE remains a remarkably successful model for describing ultrafast nonlinear dynamics in optical fibres, including supercontinuum generation.

2.3 Swept-source technologies

2.3.1 Introduction

The term *swept-source* refers to periodically wavelength-tuned laser. While tunable lasers have been studied for multiple decades, the interest of rapidly wavelength-tuned lasers over a broad spectral range came with the development of SS-OCT and remained tightly connected with this technology [1], [8]. By sweeping the wavelength of the emitted light in a controlled manner, swept-sources enable

precise time-encoded detection of spectral information, offering significant speed advantage.

The development of swept-sources have been linked to key components including dispersion elements, semiconductor technologies, modulation devices. Multiple parameters have been defined to characterise swept-sources, such as the tuning range, the sweeping linewidth, and sweeping rate. Other parameters are also considered for OCT applications, such as the sweeping linearity in wavenumber, or the duty cycle.

Over the years, a wide range of swept-source technologies have been conceived and developed. In this section, we present some of the leading technologies of swept-sources, highlighting their similarities and differences. Then, we focus on the time-stretch supercontinuum design, which is the subject of investigation in this thesis.

2.3.2 Sweeping methods

Although the sweeping methods are diverse, these designs can be categorized into two groups: kinetic and akinetic swept-sources.

Kinetic swept-sources rely on mechanical devices to perform the spectral sweep. This group includes the miniaturized swept-source concepts using a micro-electro-mechanical system (MEMS)-tunable vertical-cavity surface-emitting laser (VECSEL), and the fibre based Fourier domain mode-locking (FDML). Other interesting sweeping methods have been reported (grating based sweeping using galvo-scanner mirror, or rotating polygon mirrors, etc...) but were limited to sweeping rates $<$100 kHz and are therefore not covered in this section.

On the other hand, akinetic swept-sources use alternative sweeping techniques without mechanical filters. We will describe three methods based on dispersion management (or time-stretching): the streched-pulse mode-locking (SPML), dispersion-tuned mode locking (DTML), and the time-stretched supercontinuum (TSSC).

2.3.2.1 MEMS-VECSELS

The MEMS-VECSEL technology is born out of the progress made in semiconductor fabrication and thin layer deposition, notably the molecular beam epitaxy (MBE) [73], [74]. A principle schematic is presented in Figure 2.8 (a). A VECSEL consists of distributed Bragg reflectors on both ends of the cavity and a gain medium with a layer of quantum wells or quantum dots. Optical pump schemes have been studied, but electrical pumping remains widely popular due to its better stability, simplicity and compactness [75]. The wavelength tuning is performed by placing one of the reflectors on a vibrating MEMS membrane, which modifies the cavity lengths and tunes the wavelength of the fundamental mode of the cavity.

This method has multiple advantages in performance, with a long coherence range [76]. Additionally, the recent progress in semiconductor technologies on active media enabled operation at spectral bands interesting for multiple applications, such as 800 nm, 1060 nm, 1300 nm [77]–[79]. It also represents a huge commercial interest due to the small footprint of the device, and its potential mass production, providing large quantity of affordable swept-source devices[4], [76].

However, the MEMS-VECSEL technology still suffers from the significant entry cost of semiconductor fabrication labs. The limited access to equipped facilities and to specialized operators, the long fabrication time and the failure rate of the chips slows the development of novel structures. This is especially problematic for high-speed swept-sources, where the mechanical and electrical properties of the structure are exploited to their limits, and exploration of disruptive structure is required [75].

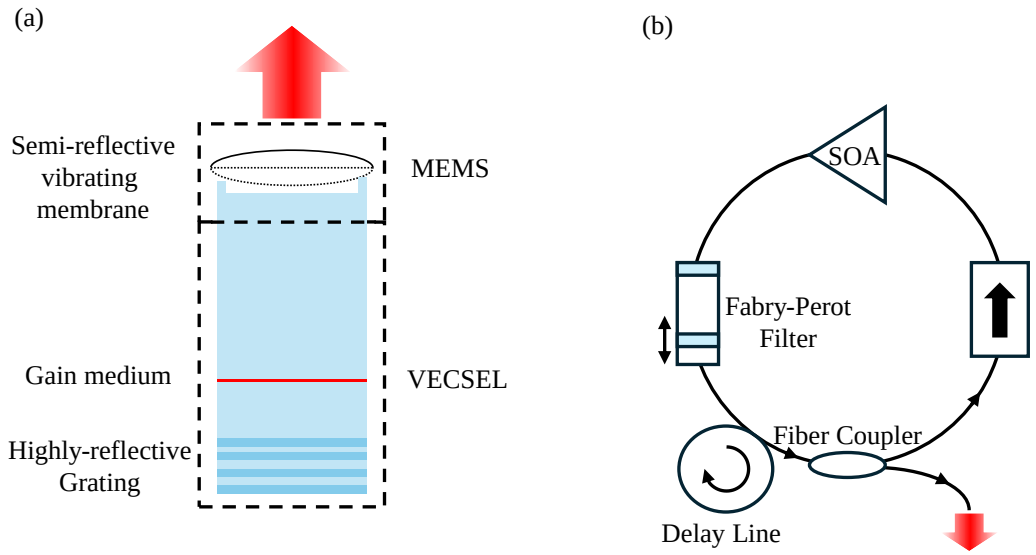

FIGURE 2.8: **Sketch of (a) micro-electro-mechanical system (MEMS)-tunable vertical-cavity surface-emitting laser (VECSEL) and (b) fibre based Fourier domain mode-locking (FDML) laser** with their respective gain element and wavelength tuning mechanism.

2.3.2.2 Fourier-domain modelocking

In order to access high sweeping-rate, the theory would encourage to reduce the cavity length like the MEMS-VECSEL. In 2006, a group of researchers imagined a solution that goes the opposite way [3].

FDML lasers are composed of an extremely long ring laser cavity, containing a variable spectral filter that would sweep periodically its central wavelength, as shown by the schematic Figure 2.8 (b). For this laser to achieve stable operation, a considerable length of optical fibre is added to the cavity so that its round-trip time would correspond to the filter sweeping rate f_s:

$$f_s = \frac{c}{nl_c} \tag{2.21}$$

with l_c the cavity length, n the refractive index of the fibre and c the speed of light in vacuum.

This method is interesting as it can exploit the mature optical fibre technology, that presents low attenuation and exhibits moderate cost for high sweeping rates up to 400 kHz (without buffering). It is also robust and has a relatively reduced footprint. Additionally, the fact that a continuous emission is produced maximizes utilization of the high sweeping rate [80], [81].

The FDML lasers face two major challenges: the high-speed tuning of the spectral filtering, and the dispersion management. First, the tuning rate of the spectral filter determines the sweeping rate. In most FDML lasers, a Fabry-Perot cavity is used where one mirror is translated back and forth to tune the nominal operating frequency of the filter. These mirrors are limited by mechanical properties, such as their weight, the frictions with the ambient medium, etc. While 400 kHz tuning rate filters have been demonstrated and buffering can provide provide access to 1.6-3.2 MHz sweeping rates, their manufacturing is complex and further speed increase is far from straightforward [82], [83].

A second challenge faced by the FDML technology is the dispersion control. Indeed, the operation of the FDML laser requires that the round-trip time of each wavelength is synchronized with the corresponding filtering timing of the Fabry-Perot cavity. As the FDML laser contains significant lengths of optical fibre, dispersion compensation devices such a dispersion compensating fibre (DCF) or CFBG are required to achieve net zero cavity dispersion and stable operation. This makes the development of FDML systems over broad bandwidth highly non-trivial and raises the cost of manufacturing.

In addition to dispersion management and high-speed spectral filtering, gain dynamics can also impose limitations in FDML lasers. The gain medium, typically a semiconductor optical amplifier, must provide broadband and temporally stable amplification over the entire sweep range. However, gain saturation and finite gain bandwidth can lead to non-uniform intensity profiles and reduced coherence, particularly at high sweep speeds. As a result, careful optimization of the gain medium and its operating conditions is required to maintain stable

FDML operation

2.3.2.3 Stretched pulse modelocking

After identifying the sweeping limitations of MEMS-VECSELs and FDML, an endeavour to seek akinetic swept-sources was initiated. In 2006, Yamashita *et al.* presented a laser cavity they referred to as dispersion tuning [84]. The gain of the cavity is modulated in synchronization with the round-trip time. Using large chromatic dispersion, only a short bandwidth meets the harmonic modelocking conditions. By applying periodic tuning of the modulation frequency, the lasing wavelength can be swept across large bandwidth. The dispersion tuning works best with a short cavity and a large dispersion. For this reason, the long SMF was replaced by CFBG [85].

In 2014, Tozburun *et al.* proposed a different approach where the active modelocking comes from an intensity modulator (IM) in a ring cavity, surrounded by two dispersive elements of opposite sign [5], [86]. This added dispersion stretches the pulse in time after the IM, and compresses it before the pulse returns to the modulator. The pulse is extracted from the cavity while time-stretched, where each pulse is therefore considered as a wavelength sweep. For this reason, the technique was named stretched-pulse mode-locking (SPML).

While this technique enabled sweeping >10 MHz, SPML operation is challenging. Firstly, it is sensitive to higher order mismatch between the two dispersion elements. Leftover dispersion prevents the onset and the stable operation of the mode-locking mechanism. Although improvement in the CFBG manufacturing reduced this issue, it remains an obstacle especially over large bandwidth SPML sources. Secondly, SPML requires high-frequency intensity modulator and precise timing synchronization, which increases significantly the complexity of this architecture.

2.3.2.4 Dispersion-tuned modelocking

Dispersion-tuned mode locking (DTML) is second type of akinetic swept-source design, with a laser cavity containing three main elements: a gain medium, an intensity modulation and chromatic dispersion [87]. Similar to active mode-locking, lasing is achieved by modulating either the gain or the loss within the cavity. The wavelength sweep is controlled by tuning the modulating frequency f_m such as it corresponds to a multiple of the resonant frequency $f_r(\lambda)$ of the desired wavelengths:

$$f_m = m \cdot f_r(\lambda) = m\frac{c}{n(\lambda)L(\lambda)} \tag{2.22}$$

where $n(\lambda)$ and $L(\lambda)$ are adjusted via the chromatic dispersion element within the cavity.

Compared to the SPML method, DTML is less complex, as it does not require precise zero net cavity dispersion. This approach has been successfully demonstrated across multiple wavelength bands relevant to optical coherence tomography (OCT), including 850 nm, 1060 nm, and 1550 nm [88]–[90]. Short cavity lengths enable rapid sweeping; however, an alternative modality employs longer cavities, wherein the tuning of a voltage-controlled oscillator is synchronised with the round-trip time of the cavity—akin to the principle of Fourier Domain Mode-Locked (FDML) lasers—though slight detuning from resonance appears necessary to enable effective optical tuning [6].

However, gain modulation imposes constraints on the sweeping frequency, ultimately affecting laser stability. Furthermore, the nonlinear relationship between drive current, optical power, and spectral bandwidth introduces additional operational instabilities. These factors have historically limited DTML technology to sweep rates below 100 kHz, with tuning ranges of approximately 10 nm. Recent advancements have explored the use of high-frequency intensity modulators operating above 10 GHz, demonstrating improved stability and broader spectral bandwidths exceeding 35 nm [89].

2.3.2.5 Time-stretched supercontinuum

Time-stretching of broadband pulsed lasers represents another akinetic swept-source design. Its fundamental principle is the separation of the generation of broadband pulses and the time-stretching process responsible for producing the akinetic wavelength sweep via chromatic dispersion [91]. This enables much more flexibility in the design of stable, high-speed, and broadband swept-sources.

In 2006, Moon and Young Kim reported a 5 MHz swept-source using a supercontinuum laser stretched using 20 km of dispersion compensating fibre [7]. Due to the large bandwidth of the supercontinuum, a sweeping bandwidth >200 nm was demonstrated, centered at 1300 nm. However, the high-order dispersion led to strongly nonlinear wavelength sweep. Additionally, the intensity noise of the supercontinuum prevented OCT imaging.

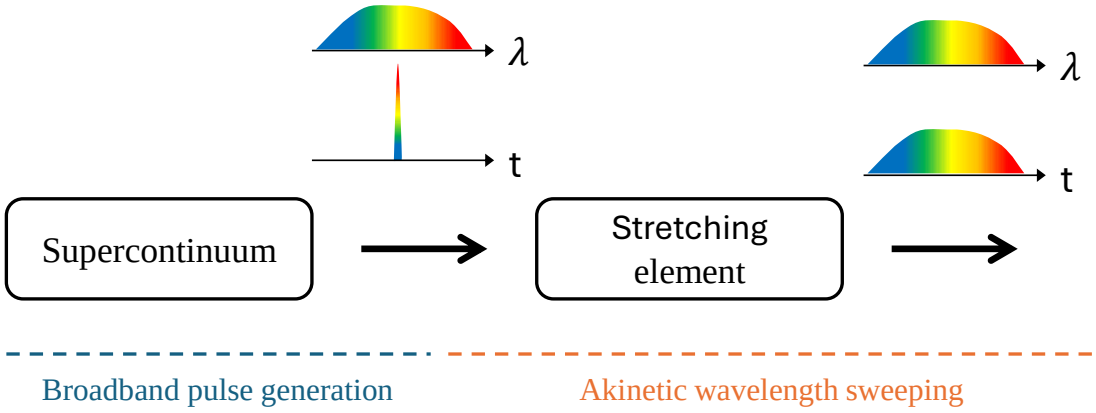

FIGURE 2.9: **Sketch of the time-stretched supercontinuum operating principle.**

The principal advantage of the time-stretching technique is that the sweeping rate is determined by the repetition rate of the laser. As pulsed lasers operate at high repetition-rate (typically 80 MHz), a significant increase in sweeping rate compared to other technologies can be obtained. In order to maximize the duty cycle of the swept-source, the total quantity of dispersion D_{tot} (in ps/nm) must be

adjusted depending on the desired sweeping rate f_r and on the sweeping bandwidth $\Delta\lambda$:

$$D_{tot} = \frac{1}{f_r \cdot \Delta\lambda} \tag{2.23}$$

Combining Equation 1.7 and Equation 2.23 and considering a set sweeping rate f_r and a maximized duty cycle, the instantaneous linewidth $\delta\lambda$ can be calculated as:

$$\delta\lambda = \frac{1}{2B \cdot D_{tot}} \tag{2.24}$$

The total dispersion is therefore directly linked to the axial range of the OCT system. This demonstrates that the time-stretched supercontinuum approach offers remarkable flexibility in the design of swept-sources tailored for specific applications, via the three key parameters: Sweeping Rate f_r / Optical Bandwidth $\Delta\lambda$ / Dispersion D_{tot}.

Using a 100 MHz modelocked fibre lasers and a pulse picker (or buffering stage) reducing (increasing) the pulse rate coupled with the appropriate lengths of optical fibre, Huang *et.al.* reported swept-sources with sweeping rates from 10 MHz to 400 MHz [9], [10]. Yet, the modelocked laser had a limited bandwidth and the high sweep rate limited the linewidth of the swept-source.

Recent research has revealed the remarkable potential of ANDi supercontinuum generation providing low-noise broadband pulses centered at 1060 nm [72], a breakthrough that paves the way for advanced time-stretch-based swept-source techniques within this critical spectral band. This development holds significant promise for applications in retinal OCT imaging. Accordingly, this thesis is dedicated to an in-depth exploration and analysis of this technology.

2.3.3 State of the art time-stretching methods

Multiple devices were investigated to apply a large amount of dispersion to broadband pulses. They offer variable maximum GVD, attenuation, higher order dispersion, and robustness. We discuss here the working principle, advantages and

drawbacks of the most common time-stretchers, and review some creative designs. To ease the comparison, an efficiency factor η is introduced, defined as

$$\eta = \frac{D}{\alpha} \quad [ps/nm/dB] \tag{2.25}$$

where D is the dispersion parameter and α the optical attenuation parameter.

2.3.3.1 Single mode fibres

Since its early development in the 70s thanks to the telecommunication applications, the optical fibre became more and more refined, with lower attenuation, reduced cost, better robustness, and easier handling. While the spectral bands covered by optical fibre expanded from UV to MIR, the technology really thrived around 1550 nm. For these reasons, long spools of single mode fibre (SMF) were the first time-stretcher used [7], [92]–[94]. For the SMF28 (by Corning), the efficiency factor η ~100 ps/nm/dB at 1550 nm.

In single mode optical fibres, the dispersion originates from a combination of material dispersion and waveguide dispersion. The dispersion from the waveguide usually dominates. By changing the structure of the fibre and the material used, the dispersion can be tuned.

In the case of broadband pulse stretching, it is critical for the dispersion $D(\lambda)$ to have the same sign across the whole bandwidth of the pulse. In a situation where it is not the case, wavelengths on each side of the zero-dispersion wavelength (ZDW) will both experience similar delay and risk to overlap in time. Therefore, dispersion shifted fibres can be interesting tools for applications near 1300 nm where the ZDW of typical silica fibres is situated.

The use of SMF to temporally stretch pulses presents many advantages. First, there are many different fibres currently available commercially, which offer multiple dispersion profiles, and therefore more flexibility in the design of the system

[10], [95]. As the fibre manufacturing technology improved, the costs of specialized fibre also decreased. Moreover, the total dispersion of the device is easily tunable by changing the length of the fibre. Using these properties, one could achieve any amount of delay and a very long stretched pulse. Finally, the dispersion profile of a fibre is continuous which makes it an interesting tool to stretch large bandwidth pulses (>100 nm).

However, while increasing the length of fibre to obtain larger dispersion is possible, the attenuation becomes rapidly high which prevents most applications. This is especially critical for fibres in near infrared (NIR) and visible range. For example, the efficiency factor η of the commercial HI1060 fibre by Corning at 1060 nm is $\sim$25 ps/nm/dB. Using Eq.2.23 and Eq.2.25 and assuming a bandwidth of 100 nm, we obtain that any sweeping rate below 20 MHz induces more than 20 dB attenuation, which limits the potential of the source for many applications. Additionally, the higher order dispersion can be significant in standard SMF, which induces a nonlinear sweeping.

2.3.3.2 Chirped fibre Bragg gratings

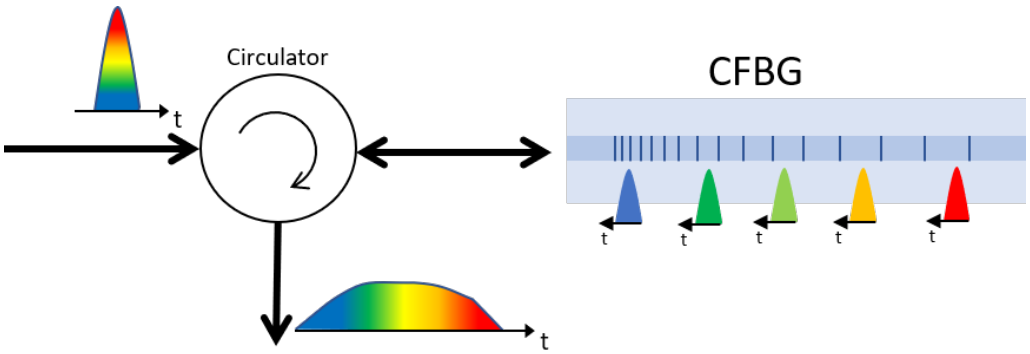

FIGURE 2.10: **Chirped fibre Bragg grating operating principle**.

As an alternative, a variant of fibre Bragg grating (FBG) was proposed, named chirped fibre Bragg grating (CFBG), to stretch the pulses. In CFBGs, instead of a constant period between each refractive index change in the fibre, this period

continuously varies, as represented in Figure 2.10. As a consequence, short wavelengths will reflect where the period is small and large wavelengths where the period is long. Alternatively, one can see CFBGs as a cascade of FBGs with different Bragg wavelengths. Each spectral component travels through a different length of fibre and therefore accumulates a different time delay.

This technology is very attractive mainly because of the low resulting optical losses. Indeed, many manufacturers can provide CFBGs with a reflectivity >90% [10], [96], [97]. CFBGs are also robust fibred components that do not need any maintenance once spliced. This makes it a good choice to develop a reliable and robust product, where free-space is often avoided for this reason.

CFBGs being relatively new, there is only a limited offer of commercial products on the market. Moreover, the design of a CFBG is expensive which can explain the limited number of companies providing custom CFBGs. Another technical issue, especially in the case of time-stretch sources where the chirp needs to be important, is the length of the CFBG. Indeed, to achieve a high reflectivity over a broad bandwidth and a high chirp, the distance between each grating plane needs to be longer, which induces mechanical difficulties for the writing of the grating. For example, to achieve a dispersion of 280 ps/nm, on a 30 nm bandwidth around 1550 nm, the CFBG would be longer than 55 cm [98]. CFBG for broader pulses would be multiple meters-long. Additionally, broadband CFBG also rely on efficient, large band fibre circulators. Such devices are not available at every spectral band of interest, increasing the complexity of such implementation.

This topic will be presented in more detail in Chapter 4, with the study of a 10 MHz swept-source using a CFBG to provide high dispersion.

2.3.3.3 Multimode fibres

Alternative time-stretching techniques have been explored, including the use of modal dispersion in few-mode and multimode fibres to achieve high chromatic

dispersion [99], [100]. However, such approaches are of limited practical utility in swept-source OCT. The coupling conditions in multimode fibres are highly sensitive to alignment, as small variations in the input angle significantly alter the modal excitation and, consequently, the dispersion characteristics. Moreover, the wavelength-dependent modal distribution leads to complex output beam profiles that are incompatible with applications requiring spatial coherence, such as those relying on Gaussian beam propagation.

2.4 Conclusion

Nonlinear effects during optical pulse propagation play a crucial role in shaping the spectrum, temporal profile, and noise characteristics of the pulse. Key parameters, such as the dispersion profile and nonlinear coefficient of the material, as well as the pulse's peak power and duration, determine how the propagation can be modeled using the generalized nonlinear Schrödinger equation (GNLSE). Under the right conditions, all-normal dispersion (ANDi) supercontinuum generation follows a two-step process: initial spectral broadening driven by self-phase modulation (SPM), followed by additional broadening through optical wave breaking (OWB). Since these effects are coherent, ANDi supercontinua offer strong potential for applications requiring broadband, low-noise pulses.

The growing demand for high-speed tunable laser sources, particularly in swept-source optical coherence tomography (SS-OCT), has led to the exploration of various designs. Some approaches, such as MEMS-VECSELs and Fourier domain mode-locked (FDML) lasers, rely on mechanical tuning mechanisms, which limit their sweeping speeds to below the multi-megahertz range. To overcome this constraint, akinetic swept-sources—those using non-mechanical tuning methods—have gained increasing interest. Among these, time-stretched supercontinuum

sources stand out, particularly due to the recently demonstrated low-noise characteristics of ANDi supercontinua, making them a promising solution for next-generation high-speed applications.

Part II

Experimental Work

Chapter 3

Ultra high-speed swept-source with fibre-based stretcher

The study presented in this chapter encompasses the work undertaken at NKT Photonics between July 2020 and August 2021, as well as the OCT imaging conducted at the Applied Optics Group (AOG), School of Physical Sciences, University of Kent, from September to November 2021. During my time at NKT Photonics, I developed the simulation tool and was responsible for the design, assembly, and characterisation of the swept-source. In collaboration with the AOG, I reassembled and recharacterised the swept-source. The design, assembly, and characterisation of the OCT systems were carried out in collaboration with Alejandro Martinez Jimenez, who was also a PhD candidate at the University of Kent at the time.

Contents

3.1 Introduction

Swept-source optical coherence tomography (SS-OCT) has gained significant attention due to its higher imaging speed compared to spectral-domain (SD) OCT, its longer imaging range, and its recent ability to access spectral bands of interest, such as 1060 nm and 1300 nm. Further advancements in this technology rely on the development of improved swept-sources. Among the various parameters defining these sources, increasing the sweep rate remains one of the most challenging. In most leading technologies, this limitation arises from the mechanical components used for wavelength sweeping. As a result, akinetic swept-source designs are attracting increasing interest within the scientific community.

This chapter explores the potential of time-stretching supercontinuum (TSSC) swept-sources employing a long single-mode fibre (SMF) stretcher for high-sweep-rate SS-OCT operating at frequencies above 10 MHz. The targeted application is biomedical imaging; therefore, the source is designed to operate within the spectral band of 1000–1100 nm, where water absorption is minimal.

A major challenge encountered in previous studies has been the high relative intensity noise (RIN) of supercontinuum lasers [7]. In recent years, however, it has been demonstrated that all-normal dispersion (ANDi) supercontinuum lasers can exhibit significantly lower noise than their anomalous dispersion

counterparts under certain conditions [72]. Consequently, the first part of this chapter details the careful optimization of the ANDi supercontinuum generation process, facilitated by the development of numerical simulation tools. This optimization led to the design of the broadband source integrated into the high-speed swept-source. Additionally, the optimization of the SMF-based time stretcher is presented.

The second part of the chapter focuses on the experimental realization of the swept-source and its characterisation. Its performance in OCT applications is assessed using a simple interferometer, and the results are discussed. Finally, the last section of the chapter explores the integration of this source into advanced OCT systems employing high-speed detectors and scanners.

3.2 Numerical simulations

The supercontinuum generation is a complex process, with multiple nonlinear effects occurring simultaneously and interacting. To assist us in the development of our swept-source, a code to simulate the nonlinear propagation of pulses in an optical fibre has been developed. It was based on the generalized nonlinear Schrodinger equation (GNLSE) presented in Equation 2.18.

The code is designed so that it generates two objects named ”Pulse” and ”Fibre”. The Pulse object contains physical information about the input laser pulse duration and temporal shape, the peak power, the central wavelength, as well as simulation parameters such as the number of points or the time resolution. The Fibre object is generated with parameters about the length, the dispersion, attenuation and the nonlinear parameter. The dispersion data from the fibre manufacturer are imported and fitted to a Taylor expansion up to the tenth order centred around the central wavelength of the pulse. The nonlinear parameter is either calculated based on the central wavelength, the nonlinear index of silica at

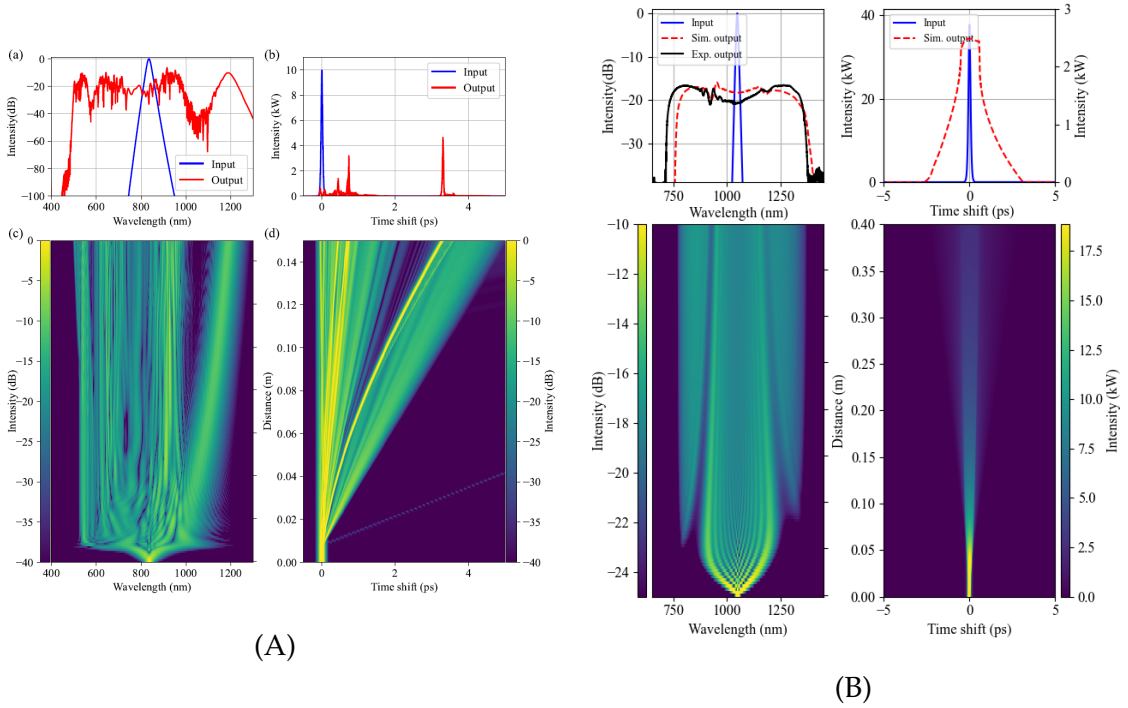

FIGURE 3.1: **(A)** Spectrogram of the supercontinuum generation in anomalous PCF simulation using the same parameters used in [66], using a sech2 input pulse at 835 nm of 50 fs FWHM with 10 kW peak power. **(B)** Simulation and experiment of ANDi supercontinuum generation in an ANDi PCF, with an input pulse duration of 180 fs (FWHM) and input peak power of 48 kW as detailed in [72]

this wavelength, and the fibre effective area, or, if previously known, its value is stored.

With these two objects created, an object Simulation imports both the Pulse and Fibre, and stores the simulation parameters, such as the step size along the fibre (fixed in this simulation code), and the number of saved points along the fibre were also adjusted to find a compromise between simulation precision and time/memory management. The propagation in the fibre follows the split-step Fourier algorithm, calculating for each step the linear effects (dispersion and attenuation) followed by the nonlinear effects (SPM, Raman) in the step. For the nonlinear effects, a custom Runge-Kutta method of the fourth order was implemented. For the consecutive propagation through different fibre length or types, multiple Fibers can be imported for successive propagation simulation.

Once the simulation is finished, a Visualizer generates the graphs needed to

analyse the simulation results: plot of the input and output spectra and time trace, 2D mapping of the spectra and time domain intensity evolution along the fibre at each saved point, as well as the relative photon error along the fibre for sanity checking the simulation. The Visualizer can also generate spectrograms to analyse the time domain and spectral domain relationship. Finally, this Visualizer can also perform measurements of the spectral bandwidth, pulse duration, peak power, and pulse energy.

To first test the code, the pulse propagation described by Dudley *et.al.* in [66] was simulated. It uses a PCF with anomalous dispersion and a 50 fs full width half maximum (FWHM) pulse with 10 kW peak power and a central wavelength at 835 nm. The simulated pulse propagation is presented in Figure 3.1(a). After confirming good agreement with the results presented in the paper [66], we next started running simulations on the ANDi supercontinuum experiment in our lab [72]. Here, a 180 fs pulse with 48 kW peak power and a central wavelength at 1049 nm propagates in 2 m of ANDi PM PCF. Once again, agreement was observed with the experimental measurements. We note that the remaining discrepancy in the ANDi simulations and the experiment are predominantly caused by assumptions about the dispersion profile of the PCF that was measured experimentally in the range 800 - 1200 nm by NKT Photonics, and extrapolated to cover the simulation range. However, for the spectral band of interest of the work presented in this thesis covering 1000 - 1100 nm, the simulation is in good agreement with the experiment.

3.2.1 Supercontinuum generation design

With confidence in the numerical model, we next started to design the swept-source. First, establishing the parameters of the input pulse was necessary. The seed laser used was an Origami 10 LP from NKT Photonics. It is a free-space mode-locked laser with specified low relative intensity noise (RIN) ($< 1\%$). The

pulse duration at FWHM of 140 fs is fixed and the maximum average power available is 65 mW with a central wavelength at 1055 nm. The repetition rate is fixed at 80 MHz. The output beam is linearly polarised with a specified polarisation extinction ratio (PER) $>$ 24 dB.

Then, the nonlinear medium had to be chosen. As the available peak power is limited, a highly nonlinear PCF was used (NL-1050-NEG-1-PM, NKT Photonics). The fibre needs to be PM to avoid noise from polarised modulation instability (PMI) [50]. The fibre core diameter is 2.4 µm, with a hole to hole pitch $\Lambda = 1.44\,\mu\text{m}$, a relative hole diameter $\mathrm{d}/\Lambda = 0.39$ and a nonlinear coefficient $\gamma = 26.8\ \mathrm{W^{-1}km^{-1}}$. The group velocity dispersion (GVD) parameter D has a parabolic profile with a maximum of -13 ps/km/nm at 1040 nm for propagation along the fast axis of the fibre [11], [50], [72].

In the design of a swept-sources for SS-OCT, three parameters require a trade-off, depending on the targeted OCT application: sweeping bandwidth, instantaneous linewidth and sweeping rate. The strength of time-stretched supercontinuum is the capacity to maximize any one of these parameters. One can use a large bandwidth supercontinuum, and then use a limited time stretching to obtain the swept-source. The instantaneous linewidth would be large, which would mean that the axial resolution would be better on the expense of the axial range. Such a swept-source would be interesting for thin samples imaging.

Where a more powerful dispersive element is available, larger axial range can be accessed. For example, let us consider a pulsed laser operating at 80 MHz with a gaussian-shaped spectrum centred at 1050 nm. If this laser has a spectrum of 100 nm bandwidth at FWHM stretched over 12.5 ns and measured with a 10 GHz photodiode and oscilloscope, the instantaneous linewidth would be 2.66 nm. In OCT parameters, this would give an axial resolution of 4.87 µm and an axial range of 0.11 mm. In the second situation, if this spectrum is reduced to 20 nm, the axial resolution becomes 24.3 µm and the axial range 0.52 mm.

However, it should be noted that this assumes that the dispersion and the

transmission efficiency of the system are approximately the same across the whole bandwidth. Significant higher order dispersion and spectral-dependent attenuation will strongly impact the final OCT parameters and will limit the use of high-dispersion high-loss stretcher.

For the swept-source presented in this chapter, we decided to use the maximum bandwidth that could be generated. The supercontinuum generation was optimized by changing the pulse peak power and the PCF length. In this case, as the pulse duration was fixed, the peak power was modified by tuning the average power. To obtain the maximum spectral bandwidth, we used the maximum power our laser could deliver. For the numerical simulations, we assumed a coupling efficiency of 60 %, giving a laser average power of 39 mW and a pulse peak power of 3 kW. The result of the simulation is presented in Figure 3.2. While some discrepancies between the spectral edges observed in the experiment and those predicted by the simulation are apparent—likely attributable to the local character of the Taylor expansion used to approximate the fibre dispersion profile—a satisfactory agreement is nonetheless achieved in terms of the supercontinuum bandwidth at full width at half maximum. In particular, a spectral bandwidth of 100 nm (FWHM) and a pulse duration of 3 ps were obtained.

3.2.2 Time stretching design

With the design of the broadband pulsed source established, we next focus on the design of the time stretcher. In this thesis, both a fibre stretcher and CFBG are presented as stretching elements. However, sourcing a proper CFBG was a major task and when decided, it had a lead time of about 1 year. We therefore performed our early (and low dispersion) experiments using a single-mode fibre. This was motivated by the availability of a large choice of fibres at a relatively low price. Multiple commercial fibres designed for 1060 nm were compared, based on their dispersion profile, attenuation profile, and cost.

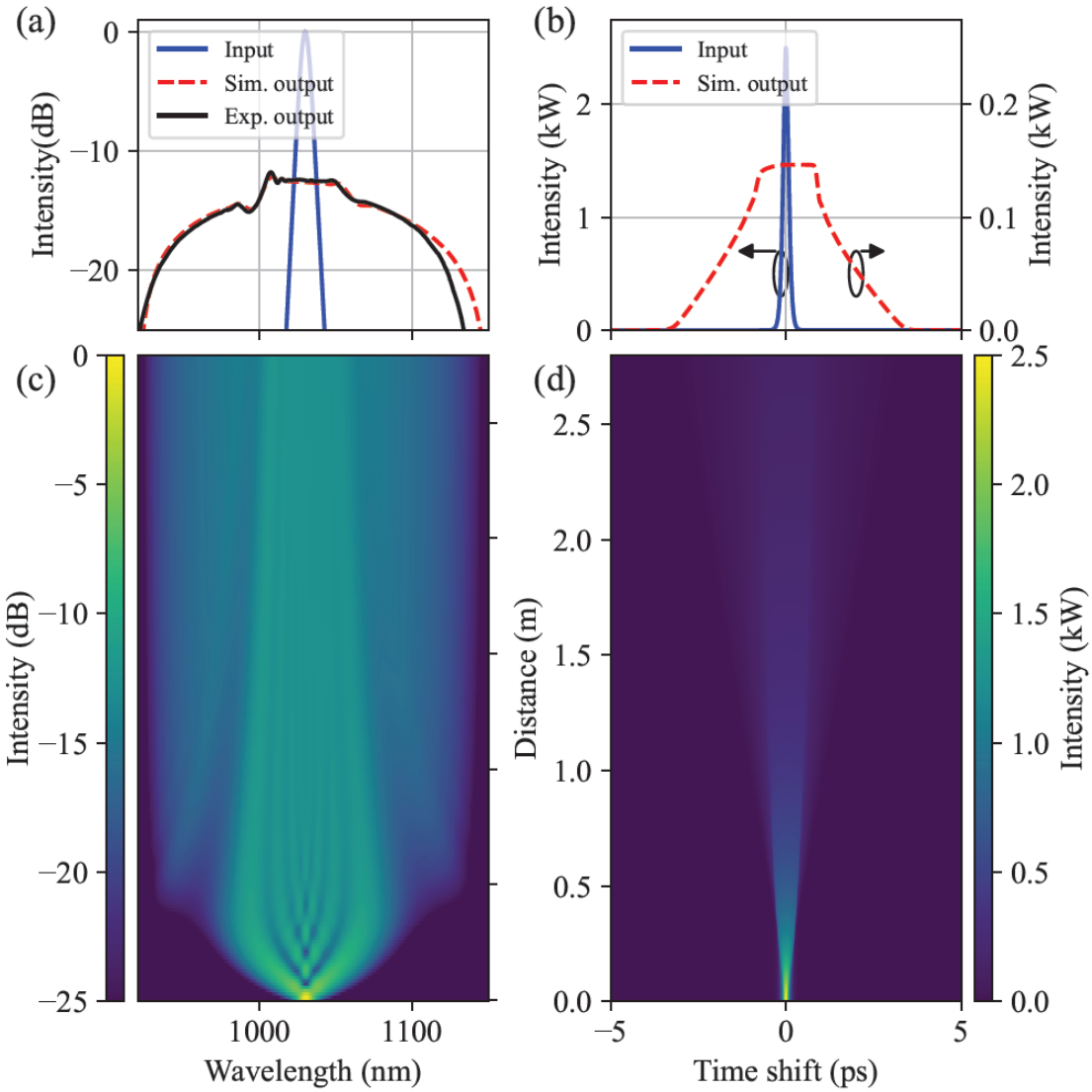

FIGURE 3.2: **ANDi supercontinuum generation.** Simulation input (blue), simulation output (red dashes), and experimental output (black) **(a)** Spectral domain. **(b)** Time domain. **(c) - (d)** Evolution of the pulse in the spectral domain and time domain during propagation. The abscissa of a-c and b-d are shared.

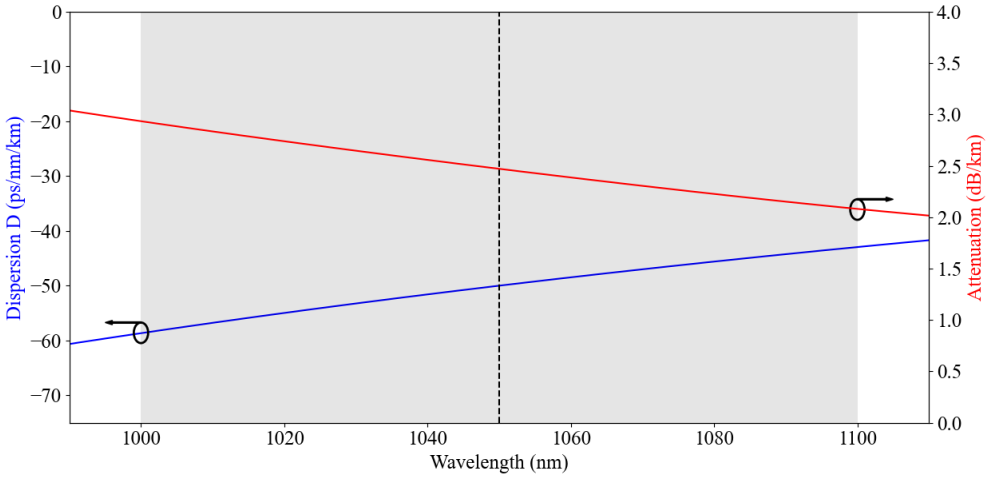

FIGURE 3.3: **Specifications of the 980-XP fibre.** The central dotted line is the central wavelength of the seed laser and the 1000 nm - 1100 nm working bandwidth defined in the introduction is marked in grey. The circles indicate the appropriate axis for each curve.

While a high absolute value of group delay dispersion (GDD) is important, attention was given to carefully minimize the higher-order dispersion in order to enable better linearity of the wavenumber-to-time mapping, which would be advantageous for the final application. Additionally, the attenuation was minimized to preserve the power of the swept-source, and its variation across the 1000-1100 nm spectral band was also limited to prevent spectral reshaping.

For the most promising fibres, simulations were performed to better estimate the length needed to reach 12.5 ns pulse stretch, which corresponds to the time interval between successive pulses. Out of these simulations, the PM980 and 980XP fibres from Nufern were the most interesting. Both fibres present similar dispersion and loss profiles. The non-PM version was used as polarisation maintaining was not a requirement for the OCT system. The dispersion and attenuation spectral profiles of the 980-XP fibre are presented in Figure 3.3.

3.3 Experimental realization and characterisation

With the design fixed, we could work on the assembly of the swept-source. The supercontinuum was generated by coupling the light from the seed femtosecond

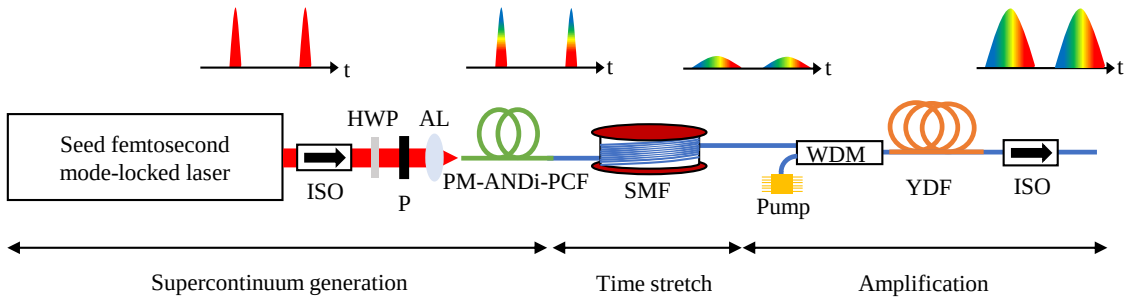

FIGURE 3.4: **Schematic of the swept-source and depiction of pulse evolution throughout the system**. ISO: isolator; HWP: half-wave plate; P: polariser; AL: aspheric lens; SM: single-mode fibre; WDM: wavelength division multiplexer; YDF: Ytterbium-doped fibre

mode-locked laser (Origami 10 LP) into the PM-ANDi PCF. An isolator was positioned in front of the laser to protect it from back reflections that could disturb the mode-locking mechanism and/or damage the laser. Due to the small mode field diameter (MFD) of the PM-ANDi fibre, measured to be 2.6 µm at 1050 nm, fibre coupling was not a trivial process. The fibre was placed in a metal holder with a V-groove, fixed on a 3-dimensional translation stage. This allows high precision in the fibre positioning. To ease the coupling, the air holes of the PCF were collapsed over 200 µm using a Vytran splicer. This also reduces the risk of damage to the fibre facet. Moreover, to couple the light to the stretcher, the PCF was first spliced to a short length of 980XP fibre (20 cm), referred to as "transition fibre". The splice was optimized using the Vytran splicer to reduce the loss as much as possible, leading to only 1 dB of attenuation.

An aspheric lens was positioned in front of the translation stage to focus the light on the fibre. The following equation describing the size of a diffraction limited gaussian beam was used to select the focal length of the lens:

$$f \approx \frac{2w_0\, d\, \pi}{4\, \lambda} \tag{3.1}$$

with $2\ w_0$ the beam waist diameter, d the collimated beam diameter. The collimated beam diameter was measured to be 1.25 mm (at $1/e^2$) by performing a

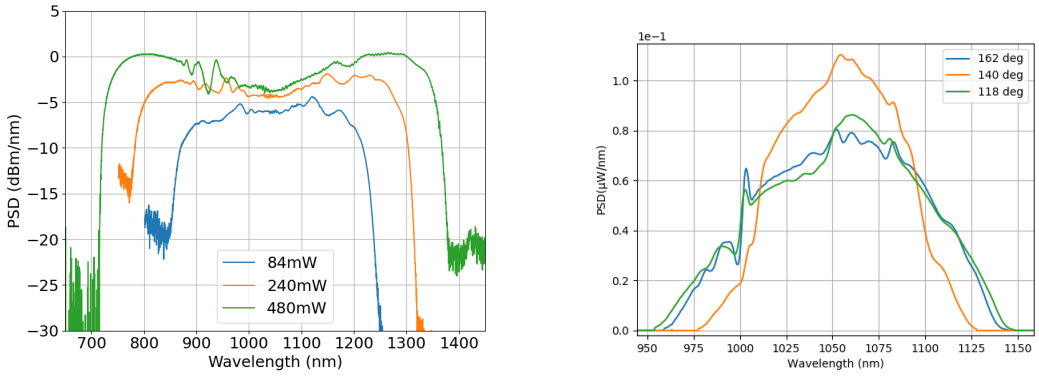

FIGURE 3.5: Example of the effect of power increase (a) and polarisation rotation (b) on the supercontinuum power spectral density (PSD)

knife edge measurement on the laser beam. To obtain a full beam waist matching the MFD of the fibre ($2\ w_0 = 2.6\ \mu m$) at a central wavelength of 1055 nm, a lens of focal length of 2.4 mm would be required. The commercial aspheric lens with the closest focal length was the C230TMD-B by Thorlabs with a 4.51 mm focal length and a B-coating. Two silver mirrors mounted in precision mounts were used to steer the beam. Using a thermal power-meter that exhibits a constant sensitivity in the spectral band, an average power of 32 mW was measured at the fibre output. Considering the 1 dB attenuation of the splice between the PCF and the transition fibre, it corresponds to 40 mW coupled into the PCF, and a coupling efficiency of 62%, matching the numerical simulation assumption.

As the nonlinear fibre used is polarisation maintaining, the output spectrum is greatly dependent on the input polarisation. The laser light is specified to be linear, but knowing the alignment polarisation axes of the fibre is challenging. Once the maximum coupling efficiency was obtained, we used the following process while monitoring the spectrum and average power at the fibre output. Firstly, a half-wave plate (HWP) was inserted in the optical path before the aspheric lens and rotated until the spectrum bandwidth was maximized. Indeed, the broadening is less efficient when the laser power is distributed on the two axes of the fibre as can be observed on Figure 3.5 (b). Differentiating between the fast and slow axes is more challenging. As the dispersion profiles are different on both axes

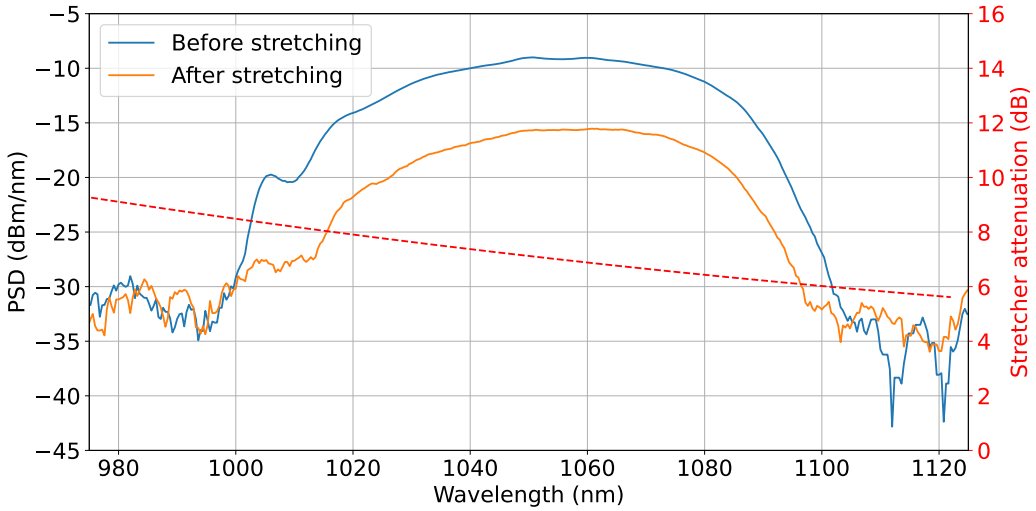

FIGURE 3.6: **Measurement of the spectrum attenuation through the stretcher.** The red dotted curve is the calculated attenuation of the stretcher.

- with a steeper parabola for the slow axis - the optical wave breaking is more efficient for the fast axis. The spectrum is therefore broader when the input light is aligned on the fast axis. Secondly, a polariser was inserted after the HWP and rotated until the average power was maximal. This ensures further cleaning of the polarisation state for a high linearity.

Once the coupling into the PCF was optimized, the transition fibre was spliced to a 99/01 fibre coupler to monitor the broadening process while the swept-source was in operation. Due to mechanical and thermal drifts, the coupling efficiency can degrade over time and the system require realignment using this 1 % output. The high transmission end of the coupler has then been spliced to the stretcher, a spool of 2.8 km of 980XP fibre.

The optical spectrum was measured after the stretcher and compared to the corresponding measurement taken before the long fibre segment, in order to characterise the wavelength-dependent attenuation introduced by the stretcher, as shown in Figure 3.6. An attenuation variation ranging from -8.2 dB to -6 dB across the spectral bandwidth was observed. This non-uniform loss resulted in a slight spectral reshaping, primarily through depletion at the shorter-wavelength edge.

The average power at the output of the stretcher was 2.9 mW, which is insufficient for the intended OCT application, where approximately 20 mW is typically required. Although this limitation was anticipated, the lack of access to higher-performing components—such as a lower-loss stretcher or higher-power laser source—hidered efforts to mitigate the low output power. As a result, a ytterbium-doped fibre amplifier was developed to compensate for the power deficit. This amplifier consisted of a 976 nm pump laser diode was spliced to a WDM to pump a 4.5 m of ytterbium-doped fibre (SM-YSF-HI-HP, Nufern). At the output of the amplifier, an isolator was spliced after the amplifier to protect the source, and an FC-APC connector was also spliced to ease the use of the swept-source for different OCT systems. The laser diode driver was set to 150 mW pump power after the WDM. Due to the splice loss and the limited bandwidth of the WDM, the broadband signal was attenuated by 3 dB, leading to 1 mW at the output of the WDM. With the amplification, the swept-source output was increased from 1 mW to 22 mW, corresponding to an amplifier gain of 13 dB.

The spectral evolution is presented in Figure 3.7, with spectra measured after the seed laser, after the broadening in the PCF and after the YDF amplifier. Due to the limited gain bandwidth of the ytterbium ions, the spectral bandwidth was reduced to 47.3 nm at FWHM. While the power amplification enables the OCT application, it also puts a significant limitation on the system, as a reduction of the optical bandwidth worsens the OCT axial resolution. Further optimization of the amplifier with a lower attenuation WDM and a better optimized fibre doping concentration and fibre length could limit this bandwidth reduction.

For the OCT application, it is interesting to know how the spectral information is mapped in time. When the sweep is obtained by time stretch, this is referred to as a time warp. This time warp was measured by filtering each spectral component and measuring each delay compared to a fixed reference. The output of the swept-source was collimated using a silver parabolic mirror, which avoids chromatic aberrations. Then, the beam was aligned into a monochromator made out

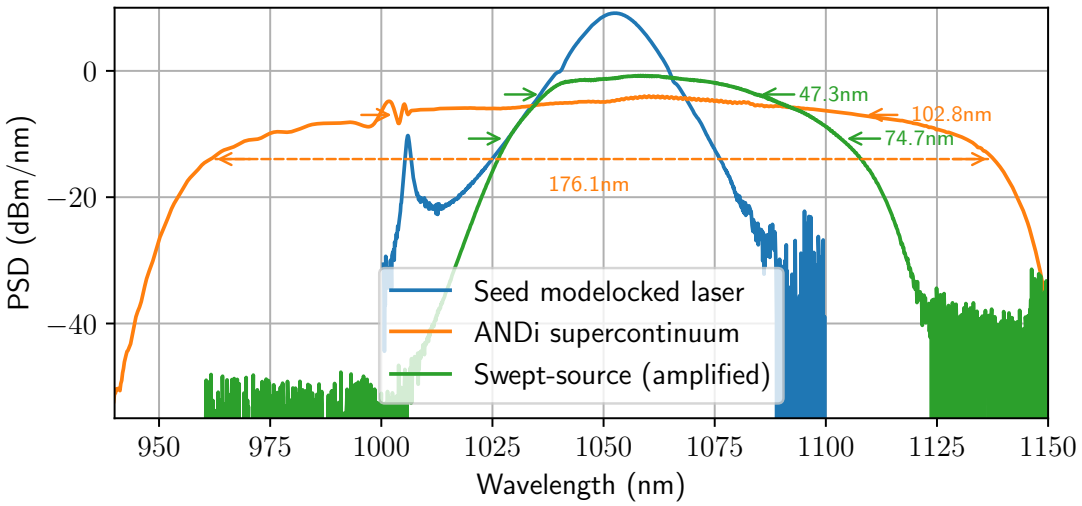

FIGURE 3.7: **Spectrum measured along the system**. The bandwidth are measured at FWHM (-3 dB) and -10 dB.

of two parabolic mirrors and one diffraction grating placed on a rotation stage. By rotating the grating, the wavelength was selected. A slit at the output of the monochromator limited the linewidth of the output spectrum to 1 nm. The output of the monochromator was coupled into a multimode fibre connected to the desired instrument.

For the spectral domain measurement, an optical spectrum analyzer (OSA) was used (AQ6374 by Fujikura). Then, the time domain was recorded by a 5 GHz biased InGaAs photodiode (DET08CFC by Thorlabs) and digitized using a 12 GHz sampling oscilloscope (Picoscope 9201 by Pico Technology). The scope was triggered by a temporally-fixed reference signal obtained from an internal photodiode in the Origami 10 LP, allowing a relative delay of each wavelength component to be measured. Both measurements were performed for every 1 nm from 1030 nm to 1110 nm. The result is presented in Figure 3.8. Each point is mapped in Figure 3.8 (b) and the data are fitted with a parabolic function. In the inset, the same plot is presented in wavenumber, as this parameter has more meaning for the OCT characterisation. This shows the high linearity of the sweep with a coefficient of determination higher than 0.99998, which reduces the need for nonlinearity compensation in OCT processing. The pulse duration measured at

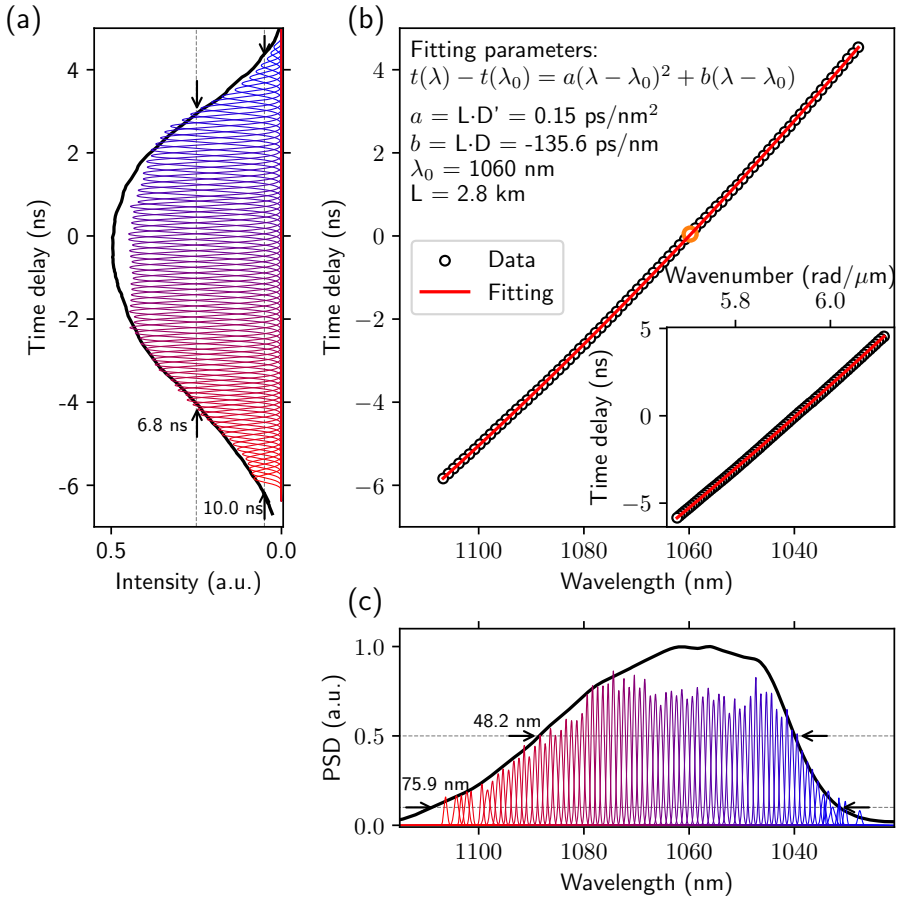

FIGURE 3.8: **Time warp measurement.** **(a)** Time domain measurement. **(c)** Spectral domain measurement. Each position of the grating is presented with the same colour in both domains. The black line corresponds to the pulse measured before the monochromator. The pulse duration and spectral bandwidth are measured at -3 dB and -10 dB. **(b)** Time warp fitted with a second order polynomial according to the formula presented. The inset presents the time warp in wavenumber with a linear regression.

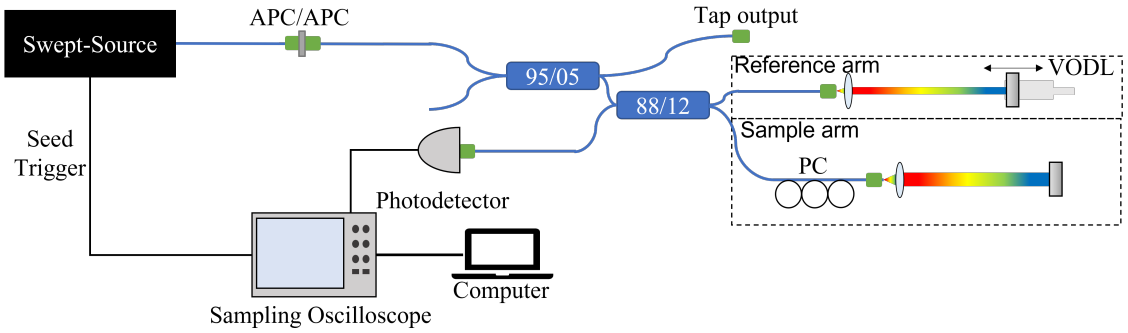

FIGURE 3.9: **OCT performance characterisation set-up.** APC: Angled Physical Contact fibre connector; VODL: Variable Optical Delay Line; PC: Polarisation Controler.

-10 dB was 10.0 ns, leading to a duty cycle of 83%. The parabolic regression gives a measure of the stretcher dispersion $L \cdot D = -135.6\,\mathrm{ps/nm}$ at 1060 nm, giving $D = -48.4\,\mathrm{ps/nm/km}$ that confirmed the theoretical value of the 980XP fibre dispersion.

3.4 Characterisation of performance for OCT

To confirm the performance of the swept-source for SS-OCT, a simple interferometer was built, shown in Figure 3.9. An APC connector was spliced to a 95/05 coupler that was used as a tap output to monitor the swept-source output average power and spectrum. On the 95% end, an 88/12 coupler was spliced, splitting the light into the reference and sample arms. This splitting ratio was used to maximize the light collected from the sample. Both couplers are made with HI-1060 fibre. In the sample arm, a fibre polarisation controller was spliced so it can be tuned to match the polarisation state of the reference arm and maximize the fringes visibility. An equivalent length of fibre is added in the reference arm to compensate for the dispersion introduced in the sample arm, thereby reducing the need for dispersion compensation during post-processing. The fibre output of each arm was connectorized with APC connectors and fixed to 3D stages with aspheric lenses to collimate the beam. The average power in the reference and sampled arm were measured to be respectively 19.0 mW and 2.6 mW. A silver

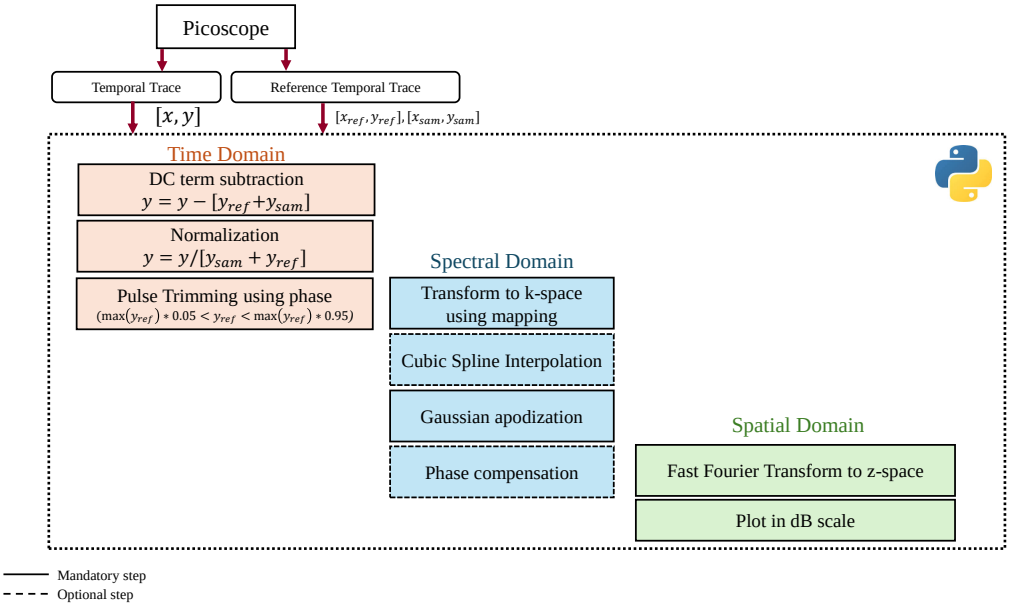

FIGURE 3.10: Schematic detailing the processing used for the OCT. x and y respectively are the time and the intensity data.

mirror was placed on a translation stage aligned along the optical axis (noted z-axis) in the reference arm. For the calibration, another silver mirror was positioned on the sample arm. The light from both arms traveled through the coupler and was measured at the output with a 5 GHz biased photodiode and the sampling scope used for the time warp measurement. The position along the z-axis was measured so that the distance to the fibre was the same in both axes. An average power of 1.8 mW was measured on the photodetector (0.9 mW from each arm) which includes the coupling loss and the attenuation of the imperfect mirror.

We performed a roll-off measurement, recording the interference signal for each optical path difference (OPD), as well as the signal from the light in the reference (sample) arm while blocking the sample (reference) arm for DC subtraction.

Once the data were recorded, it was processed by a code developed in Python using phase calibration with dispersion compensation (PCDC) algorithm as described by Bradu *et.al.* [38]. The schematic presented in Figure 3.10 details each

step in the processing, grouped according to the domain on which they act (time, spectral or spatial domains).

First, the time trace of the interference and the reference signal are imported. Due to the akinetic sweeping mechanism, the pulses out of the swept-source were identical. Therefore, the DC signal could be used to detect the position of the pulse in the recorded time frame, using a threshold at 50% peak intensity. To obtain the DC term, the two measurements respectively with the sample arm or the reference arm blocked were summed. The DC term was then subtracted from the interference trace and the result was normalized to the DC term. The frame was then cropped to avoid inter-pulse noise.

Using the time warp function measured previously, the data in the time domain were transferred to the spectral domain, or k-space. However, with this transfer, the k-array was not linear anymore, which is necessary for the fast Fourier transform (FFT). Therefore, a cubic spline interpolation was used to re-linearize the array. Finally, an apodization function was applied to reduce sidelobes. For this processing, we chose to use a Gaussian apodization to avoid the generation of sidelobes at the expense of a slight loss in axial resolution. The spectral channel was ready to be transferred to the spatial domain via FFT. The output is plotted in logarithmic scale.

The results of these measurements are presented in Figure 3.11. Each colour represents a measurement done with a sample mirror a different axial positions separated by 100 μm, resulting in an OPD change of 200 μm. The axial resolution on the first A-Scan measured is 18.9 μm, as presented in the inset of Figure 3.11 (c). The difference with the theoretical limit of 10.3 μm can be attributed to the Gaussian apodization window that artificially reduces the spectral bandwidth, but also to any remaining chirp due to dispersion imbalance in the two interferometer arms. As the chirp is deterministic, it can be compensated in post-processing. The processing algorithm used in subsequent OCT set-ups includes dispersion compensation.

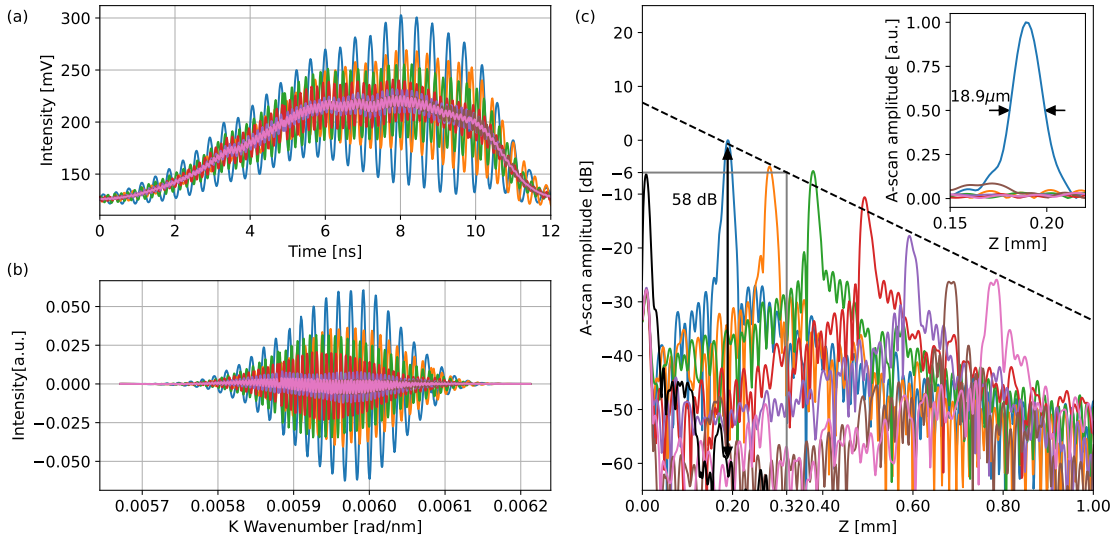

FIGURE 3.11: **OCT results with FFT-base processing for different positions of the sample mirror.** (a) Time traces of the interference pattern. (b) Channeled spectra in the K-space. (c) A-scans in the spatial domain, in dB scale. The dotted black line represents the roll-off, with the two grey lines marking the -6 dB crossing. The black continuous line is the noise measured without signal. The vertical black arrow presents the SNR. The inset presents the first A-Scan full-width half-maximum corresponding to the imaging resolution.

The roll-off was calculated with a linear regression of the A-scans maxima, with an attenuation slope of -41 dB/mm. The figure of merit traditionally used is the position where the signal intensity measured is half of that encountered close to zero OPD, leading to a -6 dB attenuation. Using the first A-Scan measured, this was evaluated as 0.32 mm. We note that this value is linked to the instantaneous linewidth of the swept-source. In a time stretch swept-source, this linewidth depends on both the stretched pulse duration and the sampling frequency of the digitizer (here 12 GHz). Therefore, a faster digitizer would enable deeper imaging. Finally, a solid black line represents the background noise of the detection system measured in the absence of incident laser light. This baseline is used to estimate the signal-to-noise ratio (SNR) of the system, yielding a value of 58,dB for the first A-scan. As the photodiode operates below saturation, this value may be regarded as an approximation of the system sensitivity. However, it should be noted that, strictly speaking, sensitivity in swept-source OCT is defined with respect to the minimum detectable sample reflectivity under illumination and in

the shot-noise-limited regime. Consequently, the reported SNR provides an indicative, rather than exact, measure of the sensitivity.

3.5 OCT application

The main limitation of ultrafast OCT systems, apart from the light source, is the speed of the detector and digitizer. The performance of these two components directly constrains the axial imaging range of the system. Moreover, they are among the most expensive elements, as the complexity of electronic devices tends to increase significantly with speed.

For this reason, although imaging with the 5 GHz photodiode and 12 GHz Picoscope would have been feasible, it was decided to conduct these experiments in the laboratory of the Applied Optics Group at the University of Kent. This allowed the use of a 20 GHz balanced photodiode and a 20 GHz oscilloscope available there.

This section first describes the installation of the system in the new laboratory and the modifications made to the OCT setup. This is followed by a characterisation of the upgraded system and the demonstration of B-scans using a commercial resonant scanner. Subsequently, the system's high-speed imaging capability is demonstrated on a moving sample. Finally, an electro-optic deflector operating at 100 kHz was used to achieve high-volume imaging rates.

3.5.1 Shipment and installation in the new set-up

To simplify the shipment and installation of the prototype swept-source, a packaging was developed housing all the fibre components (PCF, fibre stretcher, amplifier), as well as the alignment devices for the spectral broadening such as the 3D-stage with the aspheric lens, and the amplifier pump. The driving electronics were placed on a different shelve, separated from the optical system, to limit the disturbance from the fans vibration. The seed laser was a separate unit, as well

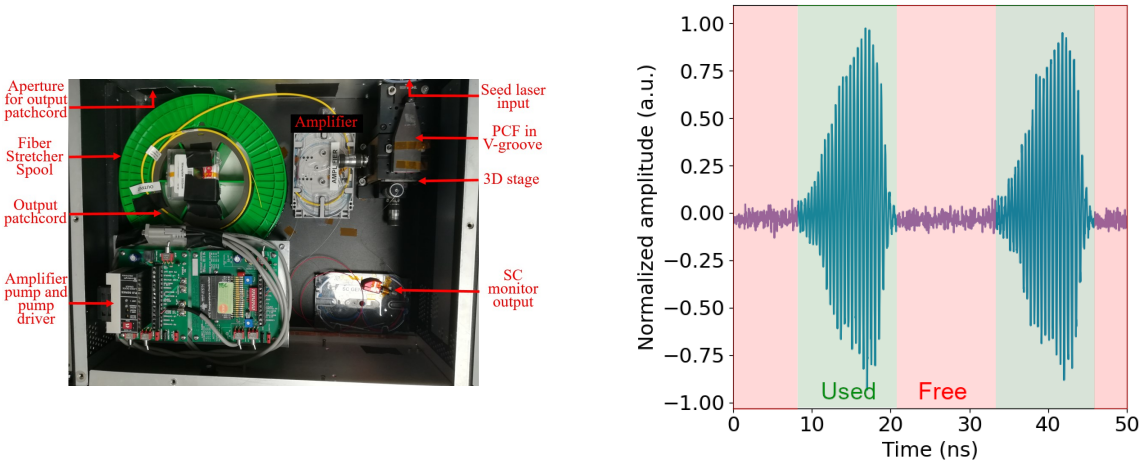

FIGURE 3.12: **(a)** Picture of the packaged swept-source. **(b)** Example of the photodetected signal obtained at the output of the OCT interferometer after replacement of the seed laser by the 40 MHz Origami 10 LP

as the other free space components used for the fibre coupling. Three openings were made in the housing: a first one in front of the 3D stage for the seed laser beam, a second one for the delivery fibre, and a third one for the pump driver electronic cables. During installation, the swept-source housing was secured to the optical table to ensure stability and maintain alignment with the free-space optics. A picture of the packaging is presented Figure 3.12 (a).

The swept-source used in this section is identical to that described in the previous section, except for the seed laser. During the initial installation, we noticed that the seed laser ceased emitting light. After conducting various debugging procedures with the manufacturer, it became evident that the damage was severe, requiring the laser to be sent for repairs. In the meantime, a replacement laser was provided by the manufacturer.

The specifications of this replacement Origami 10 LP unit were very similar to our previous source, with the major differences being a central wavelength of 1030 nm and a repetition rate of 40 MHz. The rest of the chapter reports work carried on with the 40 MHz swept-source with a 50% duty cycle, see Figure 3.12 (b), but all the results would be valid at 80 MHz with the initial swept-source as no changes were made in the stretcher. The change in central wavelength slightly

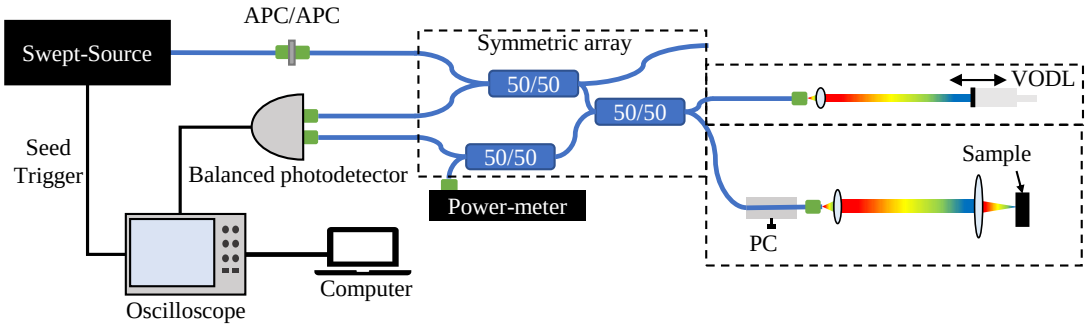

FIGURE 3.13: **Experimental set-up of the OCT system.** APC: Angled Physical Contact fibre connectors; PC: Polarisation Controller; VODL: Variable Optical Delay Line

shifted the swept-source spectrum toward shorter wavelength but the spectral broadening was identical and the final bandwidth was also limited by the fibre amplifier, as visible in Figure 3.15.

A first OCT system was built, targeting non-biological samples for a preliminary testing of the system. For this reason, power on the sample was not a limitation. This enabled us to use a symmetrical design presented in Figure 3.13, based on a fibre array composed of three 50/50 fibre couplers made of HI1060 fibre that split the power equally between a reference arm and a sample arm. The light was then collimated using aspheric lenses. The reference arm had a silver mirror on a translating mount aligned along the z-axis (optical axis) that reflects the light to the fibre. At first, the sample arm had a fixed-position silver mirror for characterisation. The light was reflected through the array and split in two before being measured by a 23 GHz balanced InGaAs photodetector (BPR-23-M by Optilab). The electrical signal was digitized using a 20 GHz oscilloscope (WaveMaster 820Zi-B by Teledyne Lecroy). The length of fibre of the couplers of the fibre array were precisely matched to minimize the dispersion imbalance between the two optical paths.

The average power at the output of the swept-source was 19 mW. Due to the design of the interferometer consisting of 50/50 couplers and the internal loss of

the components (measured to be 25% when propagating through any two couplers), the average power in each arm is 3 mW. The light reflected back to each port of the balanced photodetector has an average power of 0.55 mW, from which 0.35 mW is from the reference arm and 0.2 mW from the sample arm.

3.5.2 Characterisation process

The OCT system was characterized following the same process described in Chap.3.4. The time traces were stored in the oscilloscope and transferred afterward to the computer for processing. The real-time transfer was attempted using the Ethernet port of the oscilloscope (RJ45 cable). However, the amount of data generated exceeds the data transfer rate of Ethernet, limited to 1 GB/s. A high-speed volume acquired at 400 Hz, presented later in this chapter, represents 4 GB. This would lead to a volume acquisition at 0.25 Hz taking only into account the transfer time. That makes real-time imaging impracticable.

Storing each spectrum in individual files within the oscilloscope's memory was too slow for acquiring consecutive spectra. To address this, when multiple consecutive channelled spectra were measured, a single data file containing a large time trace of all spectra was recorded. Consequently, the oscilloscope's available RAM (32 GB) limits the maximum number of consecutive spectra to 400,000, which approximately corresponds to a volumetric image of 720 × 480 pixels along the X and Y axes. The exact physical size imaged then depends on the scanning speeds of the X and Y axes.

Once stored in the computer, the channelled spectra were processed with a Matlab code that uses complex master-slave (CMS) processing. The choice of the processing method was motivated by the multiple year of experience of the Applied Optics Group with this technique, and the robust codes that were developed that could be adapted to this project. CMS has some benefits compared to FFT-based processing, such as a more direct en-face OCT production. We note

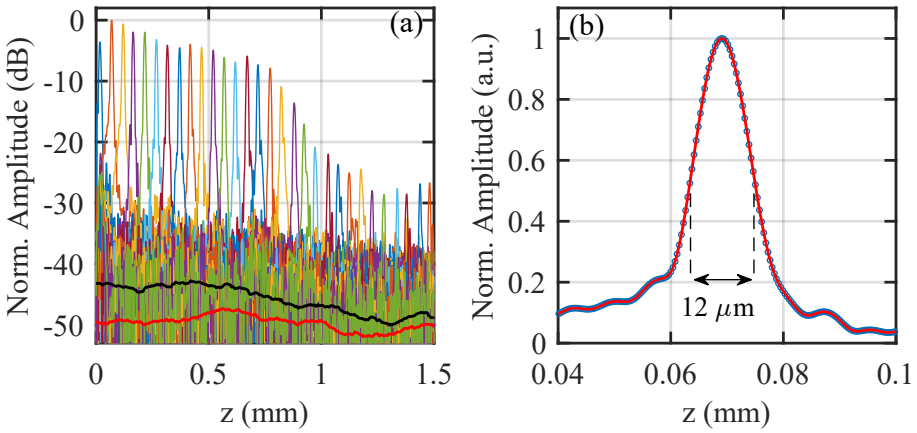

FIGURE 3.14: **OCT system characterisation. (a)** A-scans for different OPD values. The bottom black and red lines are respectively measurements of the system noise floor and the detector noise. **(b)** A single A-Scan showing an axial resolution at FWHM of 12 μm in air.

that in this situation similar performance would be obtained with Fourier transform processing. Using ten measured channelled spectra as original masks, the phase derivative was calculated, and a set of 10.000 synthesized masks that cover all the axial range was generated as presented in Chap.1.3.4. A Hamming function was used for apodization of the generated masks, to attenuate the side lobes in the A-Scan while preserving the axial resolution.

3.5.3 Characterisation results

The results of characterisation measurements are presented in Figure 3.14. An axial resolution in the air of 12 μm is obtained which is close to the 10.3 μm theoretical limit imposed by a 48.2 nm wide spectrum, considering a Gaussian shaped spectrum.

Due to high attenuation throughout the system, the photodiode was not saturated, meaning that the signal-to-noise ratio (SNR) measured corresponds to the system sensitivity. To elaborate on this, we consider the possible noise contributions in terms of shot noise, detector noise, and excess photon noise [13]. Until now, most reports of OCT sensitivity at multi-MHz scan rates considered the shot

noise as the limiting parameter [10], [82]. Based on the same assumption, we calculated the maximum sensitivity in our system to be 72 dB. In comparison to OCT systems operating at hundreds of kHz to MHz sweep rates, which typically have a shot-noise limited sensitivity higher than 90 dB, the short integration time due to high-speed imaging poses a significant barrier.

By measuring the noise present on the balanced detector when no optical power was applied, we determined the receiver noise to be 51 dB, as shown by the red line in Figure 3.14 (a). When applying the optical power, the noise floor raises to 41 dB shown by the black line in Figure 3.14 (a), indicating that receiver noise was not the dominating noise contribution. This value, less than 72 dB, also confirms that the system was not shot noise limited.

Therefore, the excess photon noise was studied, specifically considering the relative intensity noise (RIN). To perform this measurement, 1000 consecutive channeled spectra were acquired using a mirror as a sample, then transferred from the time domain to the spectral domain via the time warp presented in Fig. 3.8, and the envelope of each channeled spectrum was obtained. Using these envelopes, the RIN was then calculated for each spectral point as:

$$RIN(\lambda) = \sqrt{\langle(|\hat{A}(\lambda)|^2 - \langle|\hat{A}(\lambda)|^2\rangle)^2\rangle}/\langle|\hat{A}(\lambda)|^2\rangle \tag{3.2}$$

Figure 3.15 shows that, similar to ANDi supercontinuum reported in previous work [72], a low RIN $\sim 3-4\%$ was obtained across the FWHM bandwidth. This value is significantly lower in comparison to $\sim 20\%$ measured in OCT reports using anomalous-dispersion-supercontinuum dynamics [59]. The RIN spectrum does not show characteristics of incoherent broadening mechanisms induced by Raman scattering, technical noise, or polarisation modulation instability [50], [101]. It is therefore characteristic of low-noise ANDi supercontinuum dynamics, confirming that both the seed laser and nonlinear broadening process are low noise. We, therefore, attribute the 41 dB sensitivity to excess noise generated by

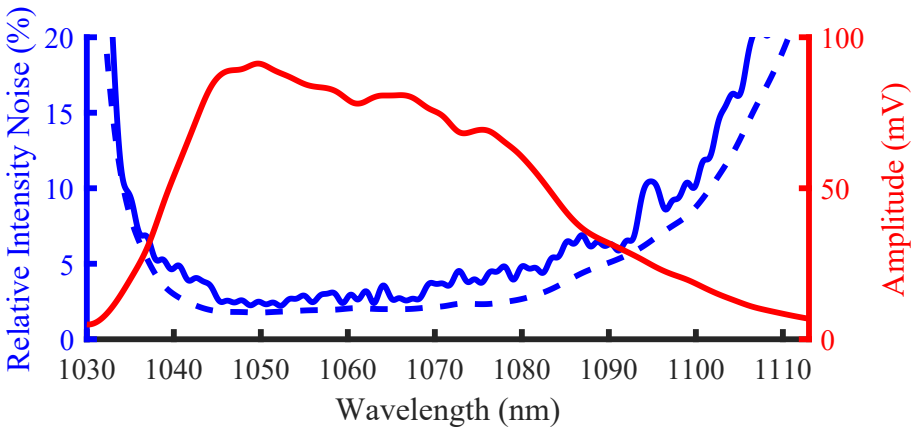

FIGURE 3.15: **RIN system characterisation.** Experimentally measured relative intensity noise (in blue) for 1000 consecutive channeled spectra with the detector limit (dotted blue), and the swept-source spectrum (red)

amplified spontaneous emission in the amplifier [102] and minor wavelength-dependent splitting-ratio imperfection on the couplers which leads to inefficient cancellation of noise at the balanced detection output. We specifically note that noise from amplified spontaneous emission in the amplifier is an incoherent noise source that cannot be eliminated by balanced detection [103].

To improve this sensitivity in future trials, two main considerations should be made. First, the use of an amplifier could be avoided by employing a higher power seed and/or a less lossy stretching mechanism, for instance, a chirped fibre Bragg grating. Second, more power from the sample would be required on the balanced detecting block. This could be achieved by reducing interferometer losses and using an asymmetric design, by increasing source power. Another possibility would be to stretch the pulses up to the seed laser period which leads to a reduction in the electrical bandwidth needed, consequently enabling noise reduction.

3.5.4 Scanning imaging

After characterizing the source, the system was prepared for imaging. First, a 4 kHz resonant mirror scanner (CRS4KHz by Cambridge Technology) was inserted into the sample arm. An achromatic focusing lens with a 30 mm focal length

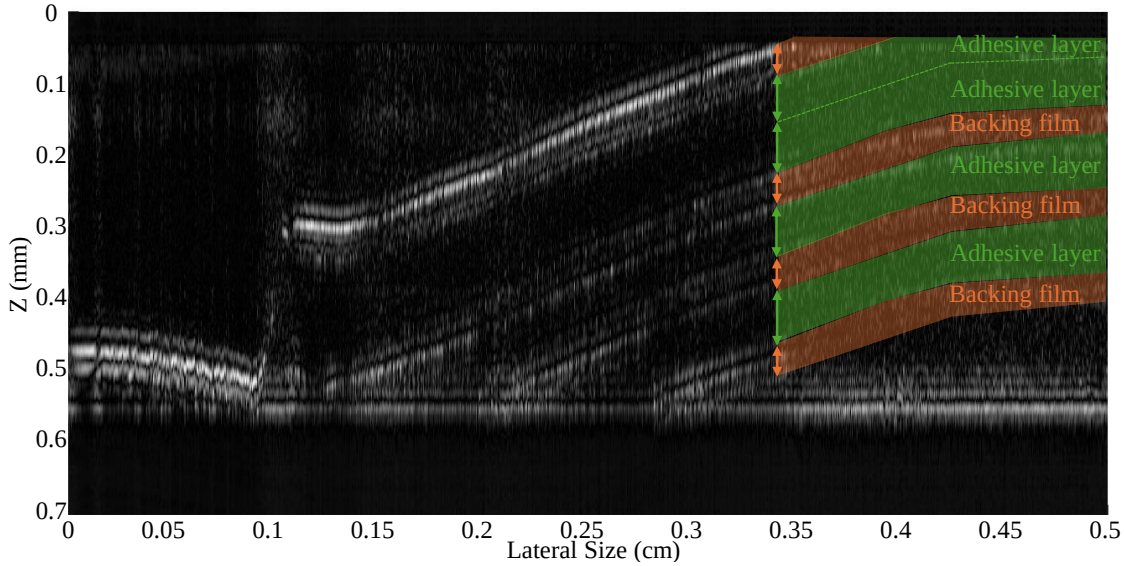

FIGURE 3.16: **B-Scan on a sample of four layers of tape**.

(AC254-030-C-ML from Thorlabs) was placed before the sample, at focal length from both the resonant mirror and the sample. The lens, scanner, and sample positions were adjusted by observing the signal measured on the photodiode while scanning, coming back from the sample arm only. For the alignment, the sample was a silver mirror as a high reflectivity eases the process. When the lens was not properly aligned, a significant drop in signal power was observed for some positions of the scanning mirror. When properly aligned, the signal intensity is homogeneous across the scanned area. The scanner driving signal was used as a trigger to record the limit of the scanning frame.

Once the scanner alignment was correct, a sample made out of multiple layers of Kapton tape in a stair shape was imaged. This is presented in Figure 3.16.

First, we notice that the layers are not perpendicular to the optical axis. This is due to the sample holder that could not handle enough strength to keep the sample flat. Second, we can clearly distinguish the different interfaces from air to tape. The different layers in each piece of tape are measured. The Kapton tape used is composed of a 25 µm polyimide backing film and a 45 µm silicone adhesive layer. Using this OCT B-Scan, the respective thickness of both layers was measured to be 65 µm and 40 µm. This matches the expected equivalent

distance in the air (calculated to be 61 μm and 43 μm) that takes into account the refractive index of these materials. Finally, the straight horizontal lines at 530 μm are due to parasitic oscillations present in the spectrum of the swept-source, not reduced by balanced detection. This can be attributed to induced birefringence in the stretcher, leading to polarization modes interference.

With this, the possibility to obtain OCT images with the swept-source has been demonstrated. However, the scanner could not match the sweeping rate of the source, which resulted in oversampling. A 4 kHz B-Scan rate consists of 25,000 points. Due to the resonant scanner, the scanning distance on the B-Scan edges is nonlinear and these points need to be removed from the data set, leading to 20,000 points/B-Scan. For a 5 mm scanning, this leads to an A-Scan lateral spacing of 0.25 μm. Considering a calculated lateral resolution of 20 μm, an oversampling factor of 80 is obtained. For this reason, another experiment had to be designed to demonstrate high-speed imaging.

3.5.5 M-Scan for fast-moving object imaging

For this experiment, the scanner was switched off, resulting in a static-focused beam on the sample. The sample was placed on a rotating beam chopper. The disk of the chopper rotates at a rate of 110 Hz. The probing point is placed at 4.2 cm from the centre of the disk, leading to a tangential speed of 29 m/s. The sample was composed of three objects. First, one layer of Kapton tape, the same used in the previous experiment, covers the chopper. On top of the Kapton tape, small pieces of Crystal tape are placed (by Scotch, with a thickness of 42 μm ± 1 μm independently measured using a high-resolution OCT). These two samples are used to demonstrate OCT imaging on fast-moving scattering multi-layered phantoms. Finally, a metallic wire whose diameter was measured to be 70 μm was placed perpendicular to the rotation direction. This last object is used to demonstrate the resolving capabilities of the high-speed system.

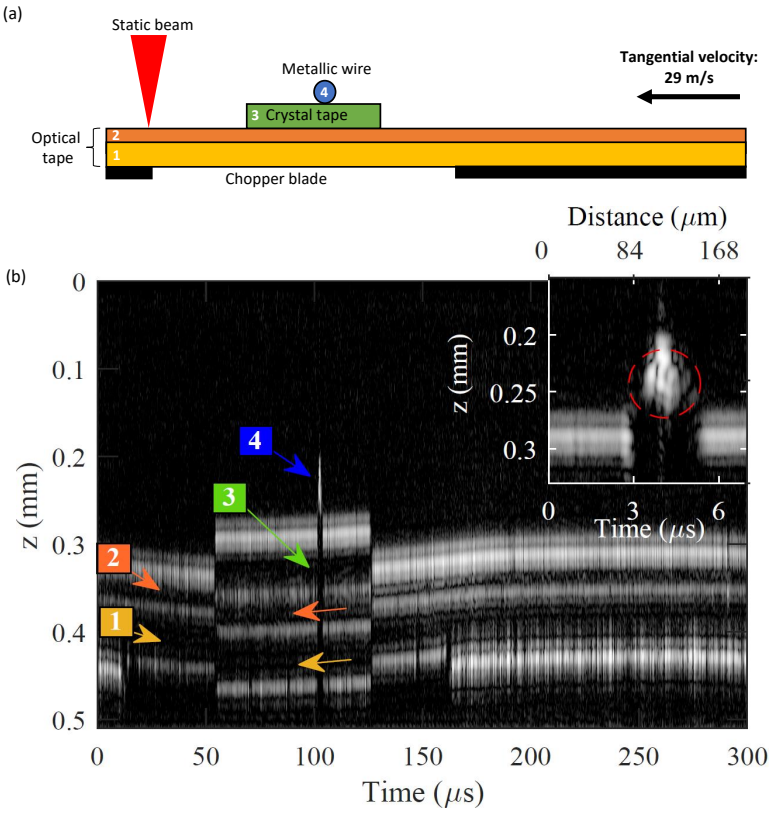

FIGURE 3.17: **Imaging of fast moving objects. (a)** Representation of the sample used. Several objects are imaged: **1** Adhesive layer and **2** backing film of an optical tape covering the whole surface of a rotating chopper disk, **3.** Short piece of Crystal tape, **4.** 70 µm metallic wire. **(b)** OCT image. The insert is a zoom on area 4. A circle in red dashed lines with a 70 µm diameter is plotted for scale

Figure 3.17 (b) shows 12,000 consecutive A-scans recorded in 0.3 ms. In the first and second areas, respectively marked by yellow and orange arrows, the optical tape is recognizable by the 3 interfaces between the air, the adhesive layer (1), the backing film (2), and the air.

In the third area marked by the green arrow, one small piece of Crystal tape is measured, with a thickness of 67 µm (66 µm calculated). The high-speed of the system allows a sharp detection of the edges of the fast-moving piece of tape while performing precise depth measurements of the four interfaces.

Finally, in the fourth area marked by the blue arrow and presented in the inset, the metallic wire can be identified. Notably, the 70 µm metallic wire, measured over a 2.4 µs range in the B-Scan, comprises 96 consecutive A-scans. This

observation suggests that the system is capable of detecting micrometric objects moving at significantly higher velocities.

3.5.6 High-speed volume imaging

These experiments demonstrated the feasibility of SS-OCT imaging with a swept-source and its potential for high-speed detection. However, no volumetric data were acquired. To enable volumetric optical coherence tomography (OCT) imaging, a high-speed scanning system incorporating an electro-optic deflector was employed. The deflector, based on a potassium tantalate niobate (KTN) crystal—hereafter referred to as the KTN crystal—operates via the electro-optic effect, enabling resonant scanning at 100 kHz. When used in conjunction with a galvanometric scanner, this configuration successfully facilitated high-speed volumetric imaging.

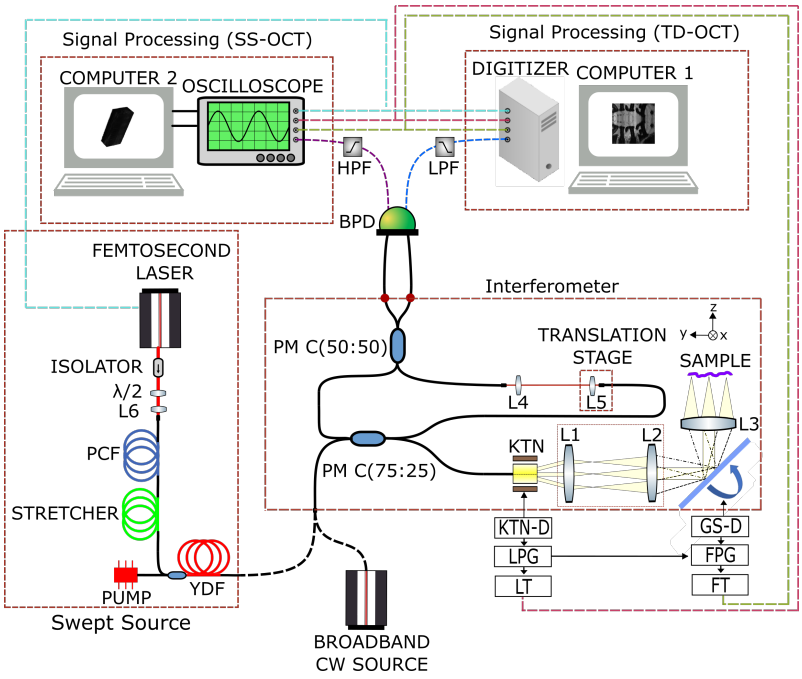

FIGURE 3.18: **Experimental set-up.** SS: swept-source; TD: Time domain, Interferometer (KTN: beam deflector using a KTN crystal, GS: galvanometer scanner, PM C: polarisation maintaining couplers); Signal processing block (BPD: balanced photodetector, HPF: High pass filter, LPF: Low pass filter); Triggers (LT: line, FT: frame); Pulse generators (LPG: line, FPG: frame); Drivers (KTN-D: KTN, GS-D: galvanometer scanner). Lenses: L1, L2, L3, L4, L5, and L6 of focal lengths 3 cm, 7.5 cm, 4.5 cm, 1.5 cm, 1.5 cm, and 4.51 mm respectively.

The first challenge is that the KTN scanner requires a linearly polarised input for efficient deflection. Therefore, a new interferometer was built, using all polarisation maintaining fibre. The system is presented in Figure 3.18. A fibre polariser filtered out one of the two polarisations at the input of the interferometer. To limit the power loss, a fibre polarisation controller was placed before the polariser and adjusted measuring the output power and spectrum at the polariser output. To ensure the stability of the polarisation state, all the fibre components were taped on the optical table, and the temperature in the laboratory was controlled.

The interferometer was implemented with an asymmetric splitting ratio in order to limit the optical power incident on the sample while maintaining a comparatively higher reference arm power at the detector. Although such an imbalance reduces the fringe visibility relative to a symmetric configuration, it enables more efficient use of the detector dynamic range and helps preserve detection sensitivity, particularly when operating below saturation. In contrast, the use of a neutral density filter at the source output would attenuate the optical power in both arms simultaneously, thereby reducing the detected signal without improving the heterodyne gain. The chosen configuration therefore represents a compromise between fringe visibility and overall signal-to-noise performance, tailored to the power constraints of the sample arm. This was an anticipation of future ophthalmic applications of our system.

The light from the swept-source was split with a 75/25 PM coupler, with most of the power directed toward the reference arm and the lowest amount toward the sample arm. The light in the reference arm was then collimated using an aspheric lens placed at a fixed position on the fibre end. The fibre end and the lens are placed together on a translation stage along the Z-axis (optical axis) to enable fine tuning of the interferometer OPD. The beam was focused again using an identical lens, and coupled in a fibre propagating the light toward the output 50/50 PM coupler. Finally, the light from the coupler was detected and digitized by a balanced photodetector and an oscilloscope, both identical to the previous

experiment.

In the sample arm, the light was deflected along the X-axis by the KTN scanner, driven using a 100 kHz sinusoidal wave generated by the KTN driver (KPS1001CH-00 by NTT Advance Technology Corporation). The deflection angle depends on the driving AC voltage, with a maximum of 124 mrad at 200 V. Fundamentally, this is limited by the thickness of the crystal [104]. The crystal induced beam shape distortions that were compensated for by a cylindrical concave lens that produces a round beam with a 1 mm diameter. A telescope made with two achromatic lenses of the respective focal length of 30 mm and 75 mm enlarged the beam diameter to improve the transversal resolution of the OCT image. Then the beam was scanned along the Y-axis with a galvo scanner (6210H by Cambridge Technology). A sawtooth signal at 400 Hz was used to drive the scanner. The light was focused on the sample using a lens of 45 mm focal length.

Along the system, significant signal attenuation was noticed. While the swept-source output was 19 mW, only 10 mW remained after the polariser, even after we optimized the swept-source output polarisation with the fibre polarisation controller. Ultimately, these losses limit the sensitivity of the system.

With the scanners switched off, the system was calibrated using CMS processing. The results are presented in Figure 3.19. An axial resolution in the air of 14 μm was measured using a Gaussian apodization. The Gaussian function makes sure that the side lobes are suppressed as much as possible but also worsen the axial resolution which explains the difference with the value measured on the previous interferometer. Similar to the precedent experiments, the axial range measured at 6 dB of attenuation was 0.61 mm, and the SNR near the zero OPD was 45 dB.

Driving the KTN scanner with the maximum voltage leads to scanning along the X-axis of 2.95 mm. With the 40 MHz sweeping rate, a line scanning rate of 200 kHz (twice the scanning rate of the KTN deflector) leads to 200 points per line along X spaced by 14.75 μm. We note that this calculation does not include

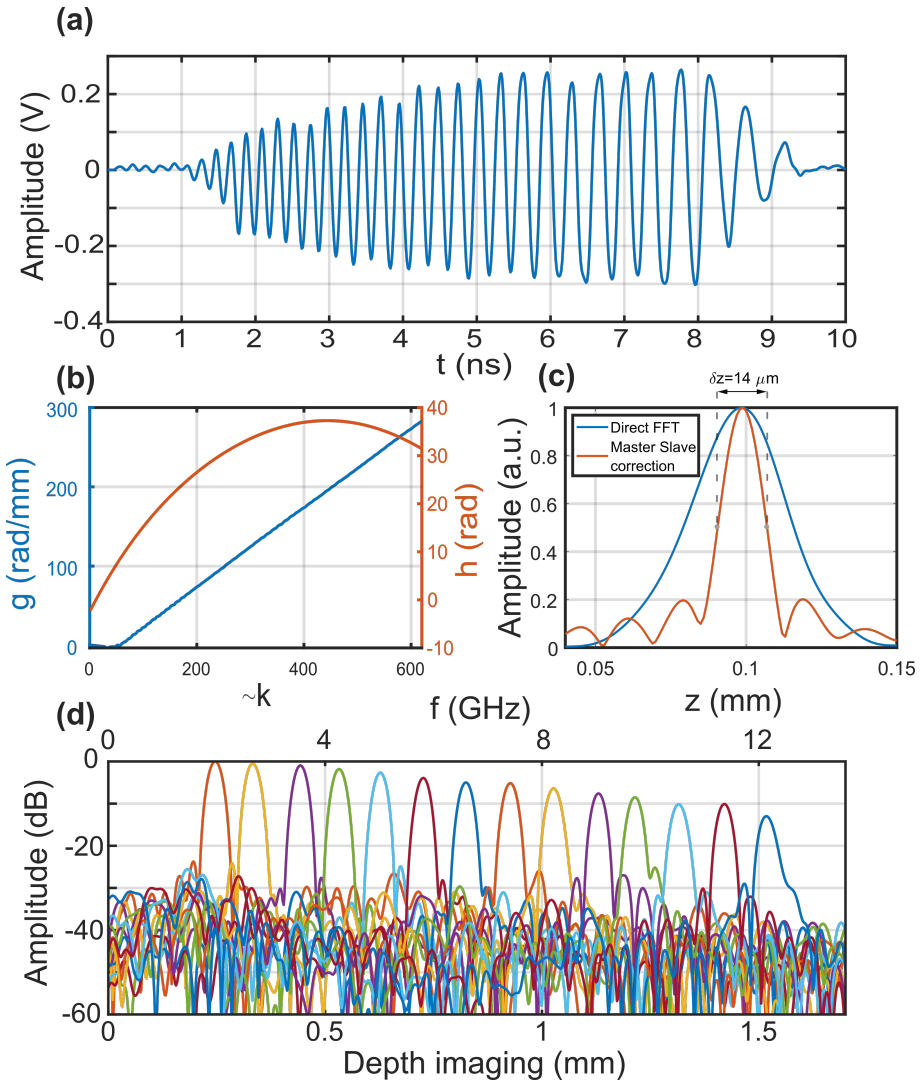

FIGURE 3.19: **Calibration:** (a) Photodetected signal corresponding to a sweep. (b) g and h calibration functions obtained by CMS. (c) Comparison between FFT of uncorrected photodetected signal (blue) and corrected by CMS (red). (d) A-Scans obtained by CMS at 14 different OPD values.

the deformation due to sinusoidal resonant scanning of the KTN, slowing the scanning at the edges. Along the Y-axis, when driven with 2.5 V peak-to-peak the galvo-scanner covers 6.6 mm. Considering the frame rate of 400 Hz, this gives 500 lines separated by 13 µm. To avoid significant oversampling, only one scanning direction along the X-axis was kept in the processing, leading to 250 lines along the Y-axis separated by 26 µm. This also eases the processing as the scanning pattern goes from sawtooth to tilted stairs scanning.

The lateral resolution was measured by the imaging of an USAF target. Along the X-axis, 23 µm was measured, and 18 µm along the Y-axis. The spatial distortion can be explained by the imperfect compensation of the KTN crystal aberrations by the cylindrical lens. Note that this results in significant oversampling along the X-axis. Future optimization of the telescope could improve this aspect.

Once calibrated, a secondary real-time time-domain OCT system was used to assist in the positioning of the sample [105]. A coin was chosen as an example of a single layer object (as light does not penetrate metal) and its topography allowed us to illustrate the capabilities of the imaging system. The letters on the coin present interesting topological features that can be measured with volumetric OCT imaging. The real-time system allowed us to place the coin at the focal distance of the last lens, and to limit the tilt. The remaining tilt was then compensated for in post-processing.

The images obtained are presented in Figure 3.20. (a) and (c) are two *en-face* views respectively at the bottom and at the top of the letters. The features are sharp and distinguishable. Three B-scans along the slow scanning axis (Y-axis) were extracted and presented. Their respective positions in the frame are marked with dashed lines. The depth along the z-axis uses the same colour code in all five plots. We can notice on the B-scans dark areas that separate the top of the letters and the base of the coin. This is due to the curvature of the letters, which is irregular due to erosion while aging. The photons reflected are not directed toward the sample lens and the optical fibre, hence the loss of photons in these

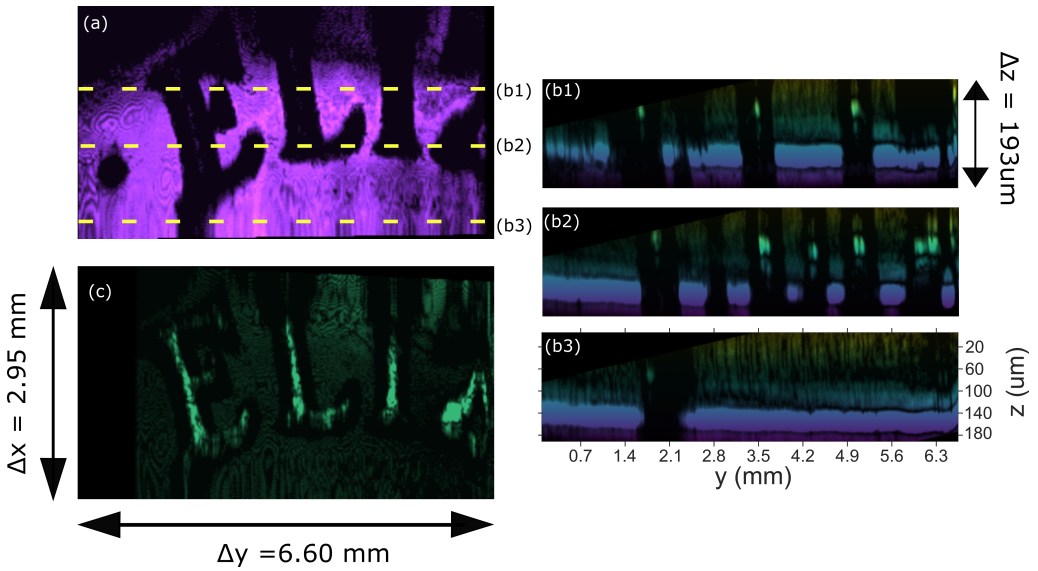

FIGURE 3.20: **High-speed OCT imaging demonstration on a coin**(a) En-face image of the bottom of the letters. (b1-3) B-scans at lateral positions as indicated by dashed yellow lines in (a). (c) En-face image of the top of the letters.

areas, while the flat top of the letters appears bright in these images.

While the sensitivity demonstrated in this application is currently limited, this demonstrated volumetric imaging at unprecedented speed at this wavelength. This device could bring significant improvement in the case of moving targets, such as surgery guidance, 4D-OCT, or polarisation sensitive OCT (PS-OCT).

3.6 Conclusion

To conclude, we presented the design and realization of a 80 MHz swept-source, operating at 1060 nm. This is an unprecedented sweeping rate at this wavelength of great potential for biomedical imaging and fast inspection. Three separate OCT systems were built to demonstrate the imaging capabilities of this source. One B-Scan showed the possibility for depth imaging, resolving the different interfaces of tapes through multiple layers. An M-Scan image of micrometer-scale objects moving at high-speed is also presented. This could open promising avenues, particularly for high-flow microfluidic or laser micromachining. Finally, a full volume at 400 Hz was demonstrated, combining for the first time a high-speed

scanner based on KTN crystal and SS-OCT. This high frame rate imaging can prove great benefit for large area scanning in handheld devices for example, or in large field of view for retina imaging.

However, this system still presents several limitations. The 2.8 km long optical fibre required in the stretcher introduces significant attenuation (>6 dB), which must be compensated by an optical amplifier. This amplifier, in turn, restricts the usable optical bandwidth, thereby limiting the axial resolution of the OCT system. Furthermore, although the swept-source exhibits low relative intensity noise (RIN) after the stretcher, the amplified spontaneous emission (ASE) introduced by the amplifier degrades the signal-to-noise ratio (SNR) of the final output. This effect, combined with the high sweep rate, leads to a reduction in overall system sensitivity, ultimately preventing effective imaging of highly scattering biological samples.

To balance these limitations, the investigation of other stretching modalities is necessary, that would provide high chromatic dispersion with lower attenuation. Alternatively, the use of a higher average power mode-locked laser and/or lower nonlinearity fibre for the supercontinuum generation could increase the power spectral density, and therefore increase the swept-source output power.

Chapter 4

10 MHz swept-source based on chirped fibre Bragg gratings

The experimental work presented in this chapter was conducted at NKT Photonics (January–August 2022) and the Applied Optics Group, University of Kent (September 2022–December 2023). The swept-source laser was developed, assembled, and characterised by the author. Its integration into the SS-OCT system, along with image acquisition and processing, was carried out in collaboration with Alejandro Martinez Jimenez, then a PhD candidate at the University of Kent.

Contents

AMONG the benefits of SS-OCT, the possibility to reach multi-MHz A-Scan rate is very promising. In the previous chapter, we demonstrated imaging at 80 MHz. However, to enable such imaging, a lower sweeping rate should be used. Retinal imaging at 1060 nm using 1.6 MHz-3 MHz swept-sources have been previously reported [106], [107]. Calculations of the sensitivity evolution with sweeping rate indicates that 10 MHz could be an interesting compromise. Reaching such low rate using the supercontinuum time-stretched method is challenging.

While a long spool of single mode fibre is an simple tool to induce chromatic dispersion, it also induces significant attenuation of the light that limits the level of power that can be delivered and as a consequence, restricts the area of applications. Another interesting approach for time-stretching is to use chirped fibre Bragg grating (CFBG) for broadband, large stretching.

This chapter presents the investigation of a 10 MHz swept-source using state-of-the-art CFBG to stretch the broadband pulses to durations not reachable with a SMF-based stretcher. The benefit to OCT imaging of highly scattering biomedical samples is demonstrated, with imaging of *in vivo* human skin and retina.

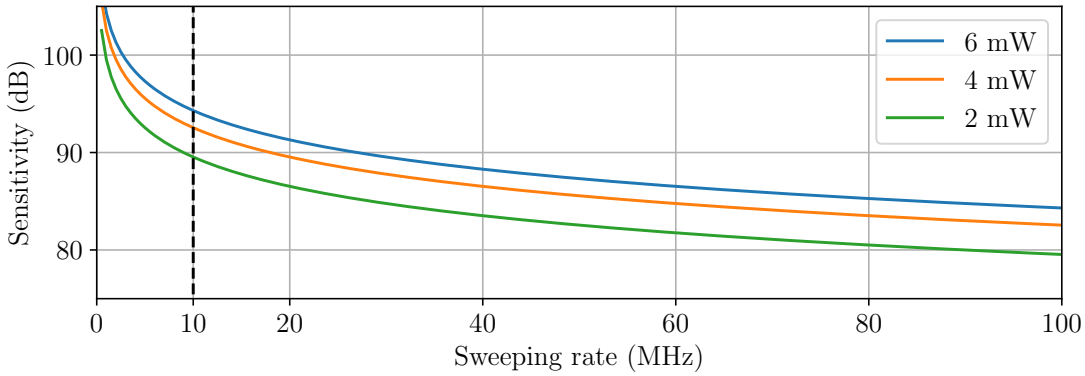

FIGURE 4.1: **Sensitivity vs sweeping rate**, assuming a shot-noise limited swept-source, centered at 1060 nm (using Eq. 4.5).

4.1 Extreme chirped fibre Bragg grating (CFBG)

4.1.1 Introduction to CFBG

A chirped fibre Bragg grating (CFBG) consists of an optical fibre, often a SMF, in which a periodic index change has been inscribed along the length of the fibre, creating a grating. This is commonly done either using UV lasers and interferometric method, through the use of masks, or point by point writing [108], [109]. The period of this grating can be engineered to reflect a specific wavelength with high efficiency ($> 90\%$), while the light at a different wavelength propagates through the grating unchanged. This reflected wavelength is referred to as Bragg wavelength λ_B, and calculated as:

$$\lambda_B = 2\Lambda n_{eff} \tag{4.1}$$

with Λ the period of the grating and n_{eff} the refractive index change. The period of the Bragg grating can also be changed along the fibre, slightly increasing. This can be written as:

$$\lambda_B(z) = \lambda_B(0) + \xi z \text{ , for } z \in [0, L_g] \tag{4.2}$$

with ξ being the chirp rate coefficient and L_g the grating length. Each wavelength is reflected from a different position in the fibre and therefore is delayed relatively

to the first reflected wavelength $\lambda_B(0)$ from the top of the structure.

The writing of CFBG offers an exceptional flexibility of design. For example, a grating can be optimized to produce a highly linear chirp by selecting a constant chirp rate ξ, which is a significant advantage for OCT application. The bandwidth and the dispersion induced by the CFBG are both limited by the total length of the grating. Indeed, in order to increase the bandwidth reflected with a fixed grating length $\Delta\lambda_B = \lambda_B(L_g) - \lambda_B(0)$, one needs to decrease the chirp rate ξ and therefore the dispersion induced by the grating.

These competing parameters become a critical limitation by the fact that the length of the grating is fixed by engineering limitations. The most commonly used method for grating inscription, interferometer and phase mask, typically produces gratings ~ 5 cm length. Therefore, each grating has to be optimized in terms of bandwidth and dispersion depending of the requirement of a specific application [108].

The third technique, the point by point inscription, can in theory cover very large lengths of fibre but requires a high precision in the order of a nanometer on the positioning of the fibre while translating the fibre perpendicular to the exposure laser beam. For this reason, the manufacturing of long CFBG is challenging and the commercial availability is limited. The recent scientific interest in such devices in multiple fields such as pulse chirped amplification, distributed sensing or laser development highlights the need for development of extreme CFBGs. To respond to such demand, companies are being set up to deliver custom gratings to address different applications.

4.1.2 Custom CFBG characterisation

A custom CFBG was ordered to stretch 100 nm pulses to 100 ns, targeting a 100% duty cycle at 10 MHz. The manufactured grating (Proximion, CB-HB005-B0930FA) was specified to operate from 1000 nm to 1100 nm, with a dispersion of 930 ps/nm.

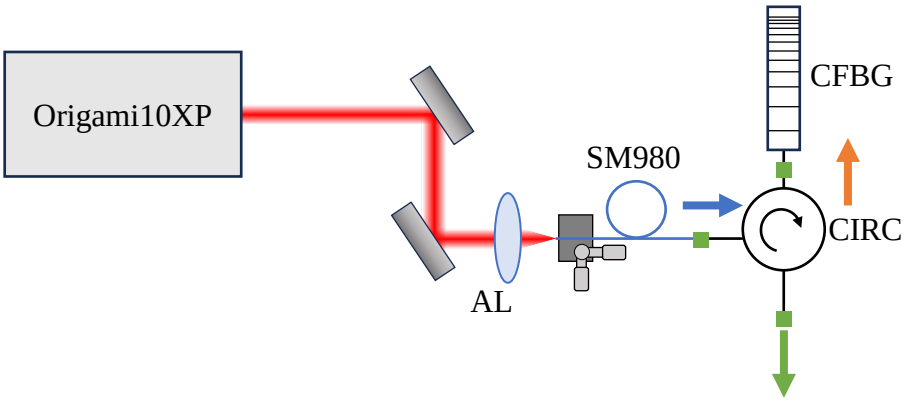

FIGURE 4.2: **Schematic of the CFBG characterisation set-up**. It was used to measure the optical attenuation, as well as the dispersion across the working bandwidth (1000-1100 nm). AL: Aspheric lens; CIRC: Circulator

As the operation of the swept-source depends heavily on the parameters of the CFBG, a characterisation experiment was built, see Figure. 4.2. For this, broadband pulses were required, as well as a broadband circulator (Opneti, HPCIR-3-1064-900-4-1-NE-1W) to extract the light reflected from the CFBG. To generate the broadband pulses, a mode-locked laser is needed. However, the lasers used in the previous chapter could not be used due to the short pulse train periods respectively of 12.5 ns and 25 ns, that would result in significant pulse overlapping after time-stretching by the CFBG. For this reason, a mode-locked laser with an incorporated acousto-optic modulator (AOM) was used (Origami 10 XP by NKT Photonics) that allows the repetition rate of the laser to be tuned.

However, the O10XP generates high energy pulses with a pulse duration of 440 fs, significantly longer than the previous lasers. The spectral broadening being dependent on the peak power, the longer the pulse the higher the average power required. To prevent thermal damage of the fibre used for the spectral broadening, the repetition rate was reduced to 1 MHz, dividing by 10 the average power.

The spectral broadening is performed in 3 m of single mode fibre (Thorlabs, SM980), which exhibit at 1060 nm a nonlinear parameter γ of 5.1 $W^{-1}km^{-1}$ and a dispersion parameter D of -40 ps/nm/km. The average power used is 46 mW

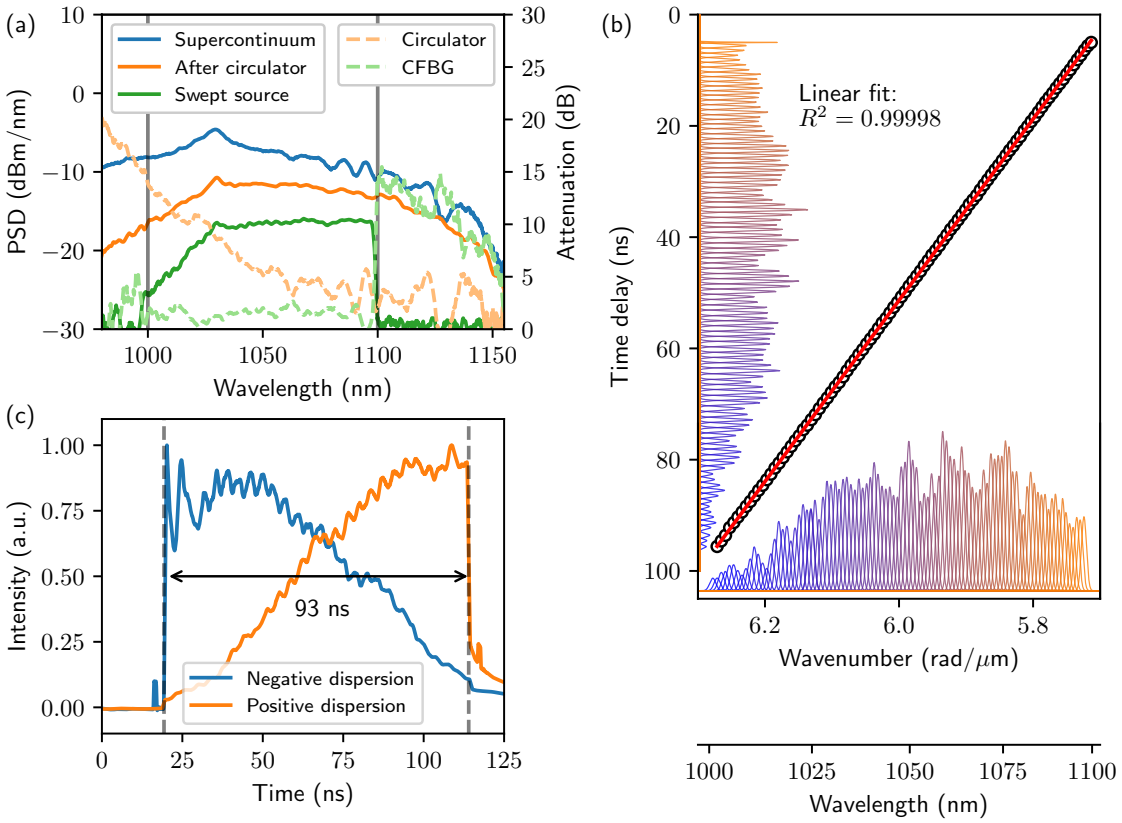

FIGURE 4.3: **CFBG characterisation**. **(a)** Spectral evolution (solid lines) and total attenuation of each components (dashed lines).**(b)** Stretcher linearity measurement. **(c)** Time-stretched pulse at the output of the swept-source.

with a coupling efficiency into the fibre of 61%, leading to 28 mW average power in the fibre which corresponds to a peak power of 56 kW. The spectrum is broadened to 47 nm at FWHM, 193 nm at -10 dB, centered at 1030 nm which is the central wavelength of the laser. The SM980, the circulator and the CFBG were all connectorized with FC/APC connectors for more flexibility in the assembly. The circulator was specified to exhibit a low attenuation (< 1 dB) over the whole bandwidth, but our characterisation using the generated broadband pulses revealed significant variability across the bandwidth of interest, see Figure.4.3 (a). While this does not prevent the characterisation of the CFBG, this failing circulator was returned to the manufacturer and replaced with a new one matching the specification, which was crucial for the swept-source final design.

Characterisation of the CFBG has proven a 100 nm bandwidth of operation,

from 1000 nm to 1100 nm, as ordered to the manufacturer, and presented in Figure4.3 (a). The attenuation of the CFBG in the operation bandwidth is $\sim$2 dB and relatively constant. This is much less than the attenuation of tens of km of fibres required to produce an equivalent delay. Modulation in the spectrum can be noticed, with a period of 4 nm. It can be attributed to the writing method of the multiple consecutive FBGs.

As visible in Figure 4.3 (c), the pulse measured at the output of the circulator is 93 ns long. The same modulation is observed, with a period of 3.5 ns that corresponds to the dispersive Fourier transform of the spectral modulation using the specified dispersion. The CFBG can be used in negative (D>0) or positive (D<0) dispersion, with negligible variation of the spectrum.

The linearity of the sweep is characterized by filtering part of the spectrum using a monochromator, measuring the filtered spectrum with an optical spectrum analyzer (Yokogawa, AQ6373B), and determining the time delay to a fixed reference using a 5 GHz photodiode (Thorlabs, DET08CFC/M) and a 12 GHz sampling oscilloscope (Picotech, Picoscope 9200). A linear regression is then applied on the set of data, as presented in Figure4.3 (b), demonstrating a high sweep linearity in wavenumber with a coefficient of determination R^2 of 0.99998. Data resampling before FFT processing is therefore not required in this system.

4.2 From 80 MHz to 10 MHz

The CFBG used in this study stretches a 100 nm bandwidth pulse to 93 ns, as discussed previously. Therefore, to optimise the pulses delivery while preventing overlap of the pulses, a seed mode-locked laser with a repetition rate of 10 MHz is required. While the Origami-10-XP was used for the characterisation experiment due to the internal control on the repetition rate, the pulses were too long to operate at 10 MHz without any damage to the fibre.

For this reason, the Origami 10 HP was preferred for the design of the swept-source, to deliver short pulses <250 fs. However, this laser does not include an internal control on the repetition rate. Therefore, an external pulse picker was developed to reduce the repetition rate from 80 MHz to 10 MHz. This section presents the work done on the choice of the modulator, the electronic system needed to drive it, the optical characterisation and the limits of such system.

4.2.1 The acousto-optic modulator

An acousto-optic modulator is a device that is made out of a crystal positioned in between a transducer and an absorber parallel to the optical axis. When the transducer is not activated, the laser beam propagates unperturbed along the crystal. When the transducer is driven with a high voltage sinusoidal signal, acoustic waves propagate in the crystal in a plane perpendicular to the optical axis, and are dampened by the absorber layer on the other facet of the crystal. For the design of the AOM, a characteristic length $L_0 = n(f/V)^2/\lambda_0$ is introduced, where n is the refractive index of the crystal, f the driving signal frequency, V the acoustic speed in the crystal and λ_0 the optical wavelength in vacuum. When the length of the crystal L=L_0, the AOM operates in the so called Bragg regime. Due to the periodic refractive index change induced by the standing wave, the crystal becomes a Bragg grating and deflects with an angle part of the laser beam. For an isotropic material, the deflection angle θ, twice the Bragg angle, can be calculated as:

$$\theta = \frac{\lambda_0 f}{V} \tag{4.3}$$

Operating in the Bragg regime presents two advantages. First, the diffraction efficiency of the first order can theoretically reach 100% [110], [111]. Second, the higher diffraction order are suppressed.

By periodically turning on and off the driving signal, a single pulse can be spatially isolated from a pulse train, resulting in a reduction of the repetition rate.

However, this operation requires specific electronic devices.

4.2.2 Pulse-picker electronics

Using an AOM as a pulse-picker requires three components. First, a clock from the laser has to be prepared. This can be done with a wedged window reflecting a fraction of the laser beam at an angle and a photodiode to measure the pulse train.

Second, the pulse train has to be transformed in a gate signal that will switch on and off the driving signal. The gating electronics take as an input the clock signal and generates a gate signal with status value 1 or 0, corresponding to a voltage adjusted to the requirement of the AOM driver. When working with transform limited pulses, like in our project, the pulses have a Gaussian profile. The gating electronics detects the rising edge of each pulse at a set threshold, and use it to switch the state of the gate signal. The gating electronics take two dynamic commands. The first one is the pulse picker ratio. Using this ratio (for example 1:8), the gate signal is switched from 0 to 1 only for one pulse, then followed by a signal at 0 for the corresponding number of pulses (7 following pulses). The second command is a delay of the gate relatively to the clock signal. Because the gate signal is generated using the pulses edge, it has to be delayed to be centered on the picked pulse.

Finally, the AOM driver emits the high voltage sinusoidal signal required by the AOM when the gate signal is at state 1.

4.2.3 Alignment and performance

The optical alignment of the laser beam can be decomposed into two aspects. The first consideration is the alignment of the beam for a angle of incidence on the AOM corresponding to its Bragg angle. The second consideration is the beam focusing into the AOM crystal. Indeed, a smaller beam improves the raising and

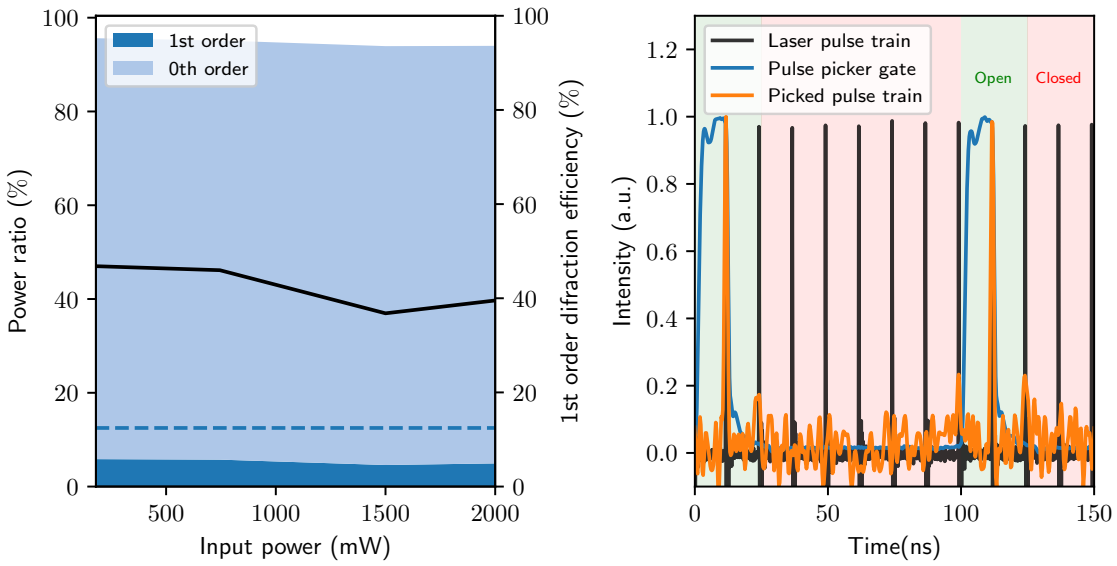

FIGURE 4.4: **AOM characterisation**. **(a)** Power distribution in each beam for increasing input power and 1st order diffraction efficiency measured (black). The dashed line corresponds to the power in the diffracted beam for 100% efficiency at 1:8 picking ratio. **(b)** Pulse picker time signals with the effective pulse picker gate open (green), and closed (red) time frames.

falling time of the pulse picker, but also reduces the diffraction efficiency. A compromise has to be found to maximize pulse selectivity while maintaining enough average power in the picked pulse for the supercontinuum generation.

We used a commercial AOM (G&H, AOMO 3200-1113) that had the fastest rising time available. Using a knife edge measurement, the seed laser beam diameter was estimated to be 1.4 mm, and its divergence angle 1.1 mrad. A lens of 75 mm focal length focuses the beam down to 80 µm in the AOM crystal, and the beam is then collimated with a 100 mm focal length lens. The longer focal length allows for a better separation of the zero order beam and the deflected 1st order beam. The power in the deflected beam with a pulse picker ratio of 1:8 is analyzed in Figure 4.4 (a) for various values of the input average power. The power ratio in the first order beam decreased slightly, from 5.9% at low power to 5.0% at high power. As the pulse ratio of 1:8 inherently reduces the average power to 12.5%, this corresponds to a diffraction efficiency of 40%.

Figure 4.4 (b) presents the pulse train before and after the pulse picker for a 1:8 ratio, as well as the gate signal. As it can be seen, the selectivity of the pulse

picker enables a high contrast in respect to the non-selected pulses. However, we notice that the preceding and succeeding pulses are also partly picked (∼20% of the picked pulse intensity), due to the long rising and falling time of the AOM. Nonetheless, to decrease the rising time, a reduction of the spot size on the crystal would be necessary which would further reduce the diffraction efficiency.

While electro-optic modulators offer significantly faster switching times, their use in the present configuration is constrained by practical considerations related to ultrashort pulses. In particular, efficient EOM operation typically requires relatively small beam diameters in order to achieve reasonable driving voltages, which in turn leads to substantially higher peak intensities for femtosecond pulses. For the present pulse energies, this increases the susceptibility to nonlinear effects and potential crystal damage. By contrast, the AOM allows operation with a larger beam size in the interaction region, providing a more robust configuration with reduced peak intensity while maintaining stable diffraction efficiency. Although thermal effects are not dominant at the average power used here, the combination of peak intensity and operational stability makes the AOM a more suitable choice in this context.

4.3 Swept-source design and characterisation

With the CFBG and the pulse picker characterized, the swept-source could be assembled. Figure 4.5 presents the structure of the time-stretched swept-source. In this section, we describe the design of the spectral broadening through ANDi supercontinuum dynamics, and the time stretching using the long CFBG. We then measured the wavenumber-to-time relationship to assess the linearity of the swept-source. Finally, as ANDi supercontinuum is well known for its low-noise, a study of the swept-source noise was conducted.

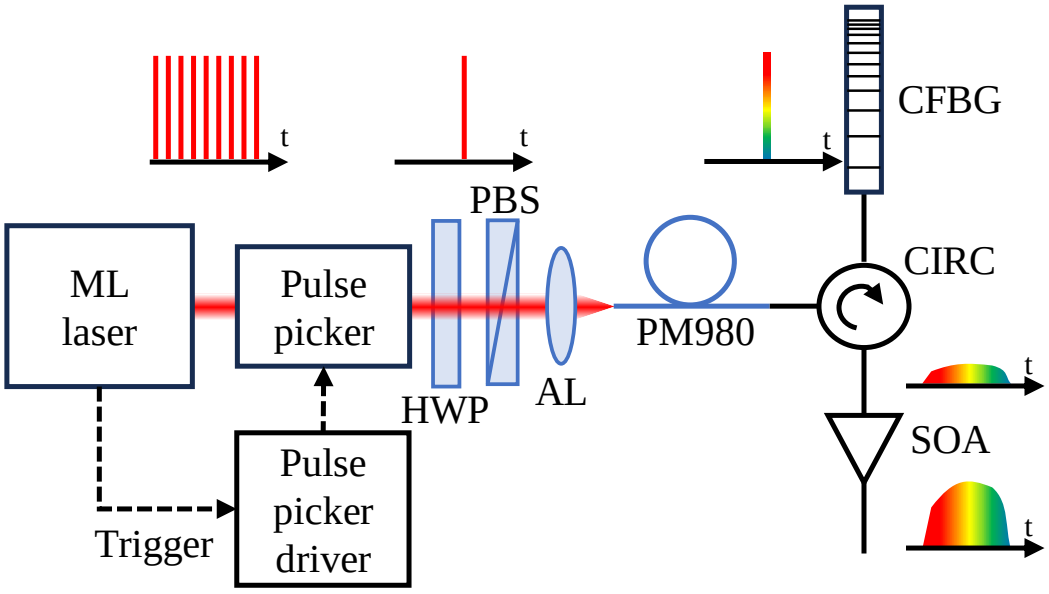

FIGURE 4.5: **Schematic of the time-stretched supercontinuum pulse swept-source structure and pulse evolution.** ML laser, modelocked laser; HWP, half-wave plate; PBS, Polarisation beam splitter; AL, aspheric lens; CIRC, circulator; CFBG, chirped fibre Bragg grating; SOA, semiconductor optical amplifier.

4.3.1 Supercontinuum generation

The laser beam exiting the pulse picker was divided into two beams. The non-deflected beam (zeroth order) was absorbed in a beam dampener for safety. The deflected beam (first order) was collected by a D-shaped silver mirror and coupled into the broadening fibre.

As large peak-power pulses were available, a high nonlinearity PCF was not required to obtain spectral broadening to a 100 nm bandwidth. Therefore, the NL-1050-NEG-1-PM (γ=26.5 $W^{-1}km^{-1}$) was replaced by a low nonlinearity commercial SMF, the PM980 (γ=3.9 $W^{-1}km^{-1}$). As can be seen by the simulations presented in Figure 4.6, this design enables a higher power spectral density (PSD) across the swept-source bandwidth, which is critical for high sensitivity OCT. Because of the elevated peak power, the potential for polarisation modulation instabilities (PMI) within the fibre becomes notable [50]. Consequently, a PM fibre (Coherent, PM980) was selected for the broadening. Additionally, to prevent cross phase modulation intensity (XPMI), the polarisation of the light was aligned

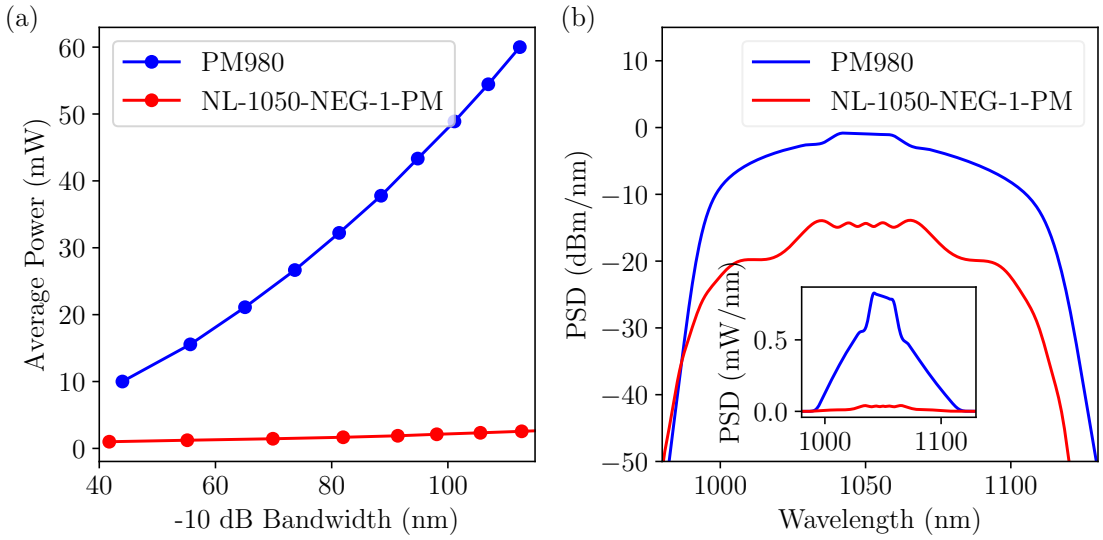

FIGURE 4.6: **Supercontinuum pulses power required for broadening to a desired bandwidth, depending on the optical fibre nonlinearity, for the same 250 fs pulse duration. (a)** Simulated average power corresponding to the desired bandwidth, for the two fibres (at 10 MHz). **(b)** Spectra simulated from broadening to 100nm (at -10dB) in a PCF (NL-1050-NEG-1-PM) and a SMF (PM980). The inset shows the same spectra in linear scale.

along the fast axis of the PM fibre using a zero-order half-wave plate (Thorlabs, WPH10M-1053). A polariser (Thorlabs, GTH10M) further ensured the linearity of the polarisation state before fibre coupling.

To guarantee a spectral broadening covering the time stretcher 100 nm bandwidth, we used simulations based on the generalized Schrodinger equation (GNLSE) optimising the fibre length and laser peak power. The supercontinuum dynamics takes place in the 5 m long PM980 fibre. This length ensures that the spectral ripples generated by SPM are smoothed out by the OWB. An average power of 102 mW at 10 MHz was used, reduced to 45 mW (18 kW peak power) at the input of the fibre due to attenuation of the polarisation optics devices and losses in the fibre coupling. Figure 4.7 (a) presents the produced spectrum with a bandwidth of 60 nm at FWHM, 110 nm at -10 dB. Compared to heavily structured spectrum of the anomalous dispersion supercontinuum reported in the literature, the ANDi supercontinuum exhibits a smoother spectrum with sharper edges [112].

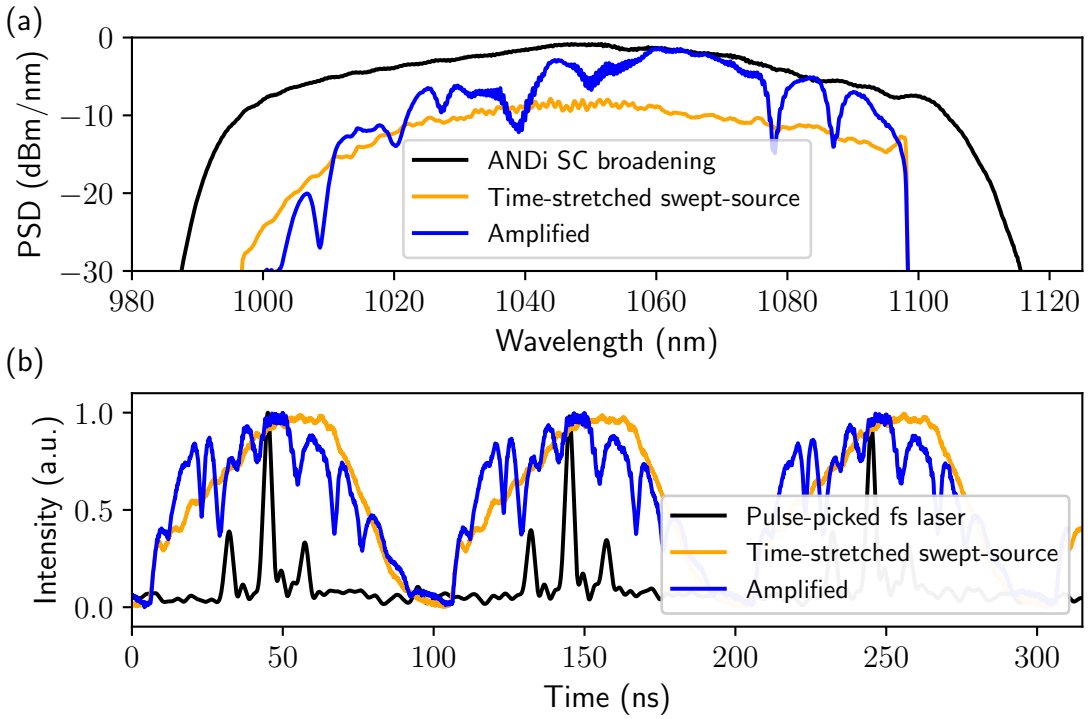

FIGURE 4.7: **Swept-source operation. (a)** Spectrum at 3 points along the system. **(b)** Time trace of the swept-source output.

4.3.2 Stretching with a CFBG

The spectrally broadened pulses are then stretched in time using a broadband circulator and the long CFBG. This stretches the pulse to Δt=D·$\Delta\lambda$=93 ns, where the steep spectral edges produced by OWB translates to a duty cycle of 93% in the time domain as shown in Figure 4.7 (b).

One benefit of long CFBG is the low attenuation-to-dispersion ratio. A combined total attenuation of 7.1 dB was measured, attributed to the circulator, CFBG and fibre splices, reducing the average power at the output of the swept-source to 8.7 mW. The CFBG-based stretcher has an efficiency parameter $\eta = 130$ ps/nm/dB as defined in Eq.2.25. For comparison, the step-index fibre used in the previous chapter (Coherent 980XP) had a stretcher efficiency parameter of 20.5 ps/nm/dB. Obtaining the same amount of dispersion than the CFBG would require more than 18 km of fibre. This would induce to more than 46 dB attenuation as presented in Table 4.1.

Stretcher type	$GDD_{@1050nm}$ (ps/nm)	α (dB)	η (ps/nm/dB)	α_{100ns} (dB)
SMF (980XP)	40/km	2.7/km	**20.5**	46
Long CFBG	920	7.1	**130**	7.1

TABLE 4.1: **Comparison of the stretchers.** The dispersion GDD and attenuation α are given per unit (propagation in the CFBG / in 1 km of SMF). α_{100ns} is the attenuation to stretch the pulse to 100 ns (one CFBG/18 km of SMF).

Nevertheless, although this power suffices for OCT imaging of highly reflective samples, optical amplification proved necessary for SS-OCT of biomedical samples exhibiting high scattering. A broadband semiconductor optical amplifier (SOA) (Innolume, SOA-1020-110-HI-27dB) was used to enhance the swept-source average power to 37 mW.

We notice in Figure 4.7 a spectral reshaping by the stretcher with higher attenuation of the low wavelengths, reducing the bandwidth to 55 nm at FWHM and 100 nm at -10 dB. Significant spectral alteration were observed after the SOA, reducing the bandwidth to 35 nm at FWHM and 90 nm at -10 dB. This is due to polarisation mode dispersion (PMD) in the circulator and long CFBG, revealed by the SOA gain, which is exclusively for the S linear polarisation. PMD compensation across the entire bandwidth with a polarisation controller is impractical due to wavelength-dependent birefringence in the CFBG. Future experiments could address this by writing the CFBG on a PM fibre.

4.3.3 Noise

ANDi supercontinuum dynamics are recommended for low noise broadband generation. As their use for time-stretched swept-source is recent, it is interesting to study how the noise transfers to the swept-source. Figure 4.8 (a) presents a measurement of the RIN of the swept-source output. 10,000 consecutive sweeps were recorded using a 2.5 GHZ photodiode (Thorlabs, PDB482C-AC) and a 20 GHZ oscilloscope (Teledyne Lecroy, WaveMaster 820Zi-B). The RIN was calculated using [113] :

$$RIN(\lambda) = \frac{\sigma(\lambda)}{\mu(\lambda)} \tag{4.4}$$

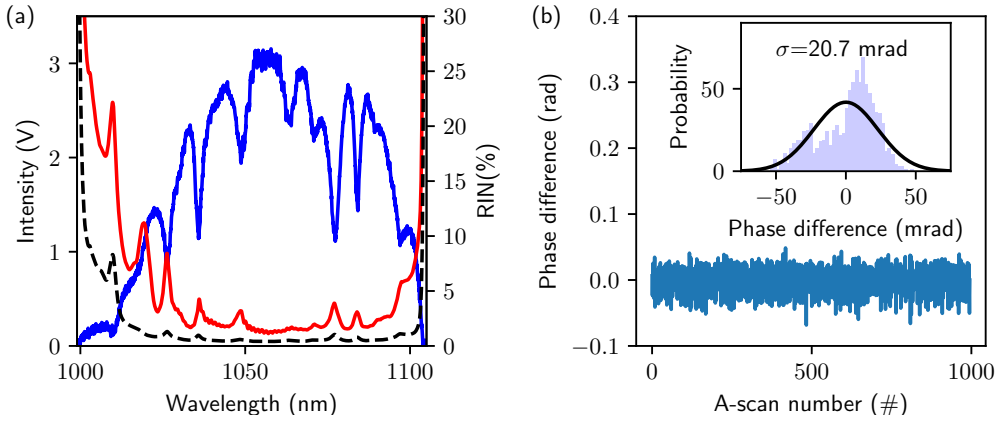

FIGURE 4.8: **Swept-source noise.(a)** Intensity noise measurement (red), detector noise level (dashed black), swept-source spectrum (blue). **(b)** Phase noise

where $\sigma(\lambda)$ denotes the standard deviation and $\mu(\lambda)$ the mean of the intensity measurements, calculated at the sweep timing associated with each wavelength.

The RIN measured is as low as 1.2%. We note that it remains slightly above the photodetector noise floor, which could be explained by the presence of amplified stimulated emission (ASE) from the SOA.

For many applications, the phase stability is crucial. In order to evaluate it a common path interferometer was employed and recorded 1000 consecutive A-Scans. Each A-Scan was processed using the complex master-slave (CMS) method, and the phase was extracted using Hilbert transform. The phase of the first A-Scan was used as reference, and the phase difference of the consecutive A-Scans was computed. Finally, the standard deviation of the phase difference histogram was calculated, giving a phase noise of 20.7 mrad as presented in Figure 4.8 (b), which is within the range of other reports on high sweep rate swept-sources [94].

4.4 OCT application

Figure 4.9 presents the structure of the interferometer system used to characterise the suitability of the swept-source for OCT. This system adopts an asymmetric

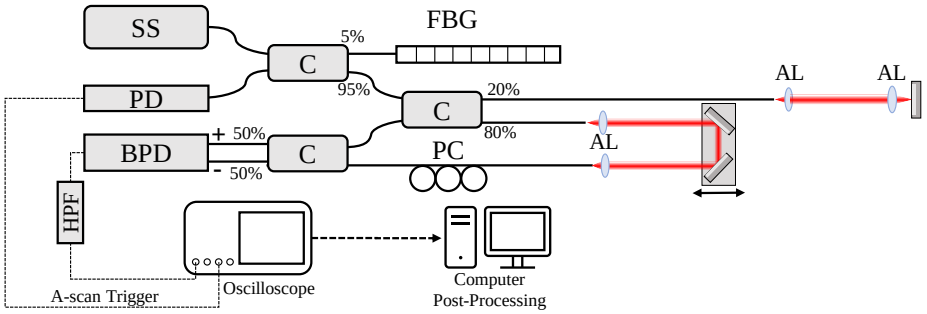

FIGURE 4.9: **Schematics of the OCT characterisation set-up**. Based on an asymmetric interferometer design, a trigger is picked at the input to ease the calibration with a trigger. SS, swept-source; C, fibre coupler; FBG, fibre Bragg grating; AL, aspheric lens; PC, polarisation controller; PD, photodetector; BPD, balanced photodetector; HPF, High pass filter.

design to optimise light collection from the sample, a critical aspect when imaging low reflectivity samples. An InGaAs 22 GHZ balanced photodetector (Optilab, BPR-23-M) and a 20 GHz oscilloscope digitized the interference signal. A 400 MHz high-pass filter was employed to suppress the DC signal. The lengths of the reference and sample arms were precisely matched to limit dispersion imbalance. At the input of the system, a 95/05 fibre coupler, a fibre Bragg grating and a 5 GHz photodiode (Thorlabs, DET08CFC/M) are used as a trigger for the OCT system. The FBG has a narrow reflectivity bandwidth of 0.1 nm centered at 1090 nm delivering a short pulse when the wavelength matches that of the FBG, pulse to be used as a trigger for synchronising the imaging process.

4.4.1 Signal processing and imaging performance

The interference signal was processed using the Complex Master Slave (CMS) method [37]. Figure 4.10 (a) presents two interference signals recorded for different optical path differences (OPD) corresponding to 1.232 mm and 1.432 mm depth measured in air. From these, 10,000 eigenvectors (also known as "masks") were synthesized with CMS, each corresponding to a specific depth spaced by 0.55 µm. A Hanning apodization was applied to the synthetic masks to limit side lobes in the A-Scan.

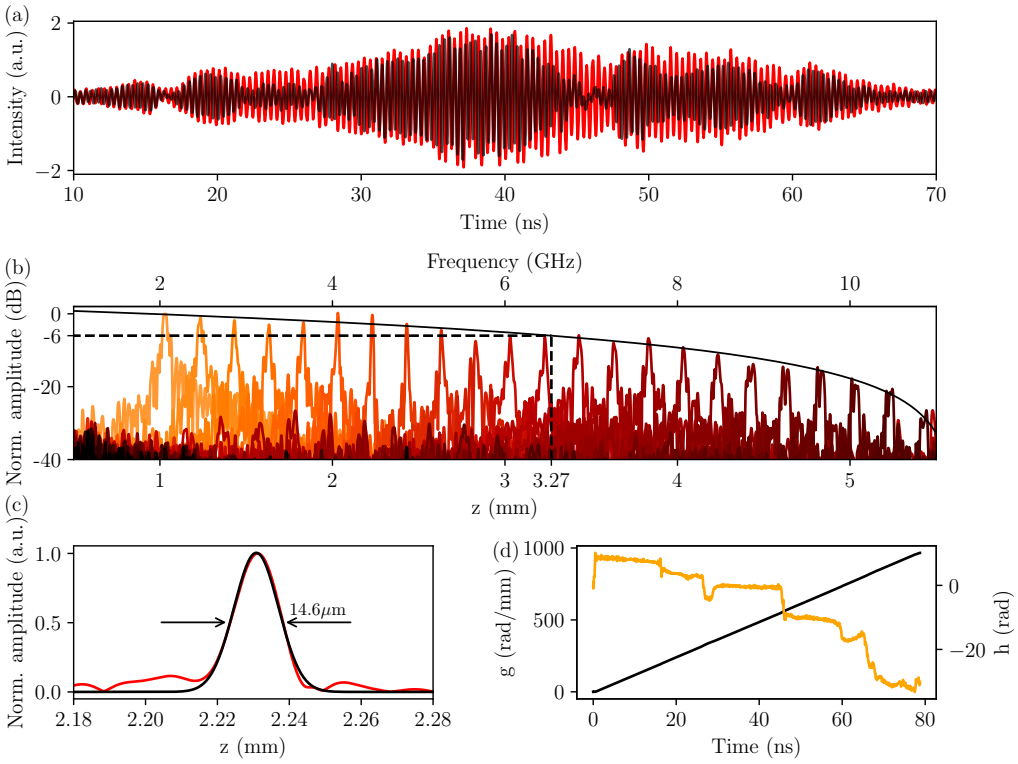

FIGURE 4.10: **OCT performance**. **(a)** Channeled spectra for two different OPD. **(b)** Roll-off measurement with logarithmic fit (solid black) and -6 dB level (dashed black). **(c)** Axial resolution measurement, with Gaussian fit (black). **(d)** CMS phase parameters g(k) (black) and h(k) (orange).

A roll-off measurement is presented in Figure 4.10 (b), with 6 dB axial range of 3.27 mm. Figure 4.10 (c) presents an A-Scan, that shows an axial resolution measured in air, δz, of 14.6 µm, in agreement with the theoretical resolution of 13.6 µm (that assumes perfect Gaussian spectrum).

While recording the masks for the roll-off measurement, we observed that the A-Scan peaks did not exhibit the expected roll-off behaviour and instead displayed a modulation pattern, with A-Scan intensity drops at fixed period in OPD. The masks for Figure 4.10 (b) were recorded at the maximum intensity OPD. However, such behaviour is atypical for SS-OCT systems and warranted a detailed investigation. Examination of the phase parameters *g(k)* and *h(k)*, obtained from the CMS processing and shown in Figure 4.10(d), reveals the presence of phase discontinuities. By comparing the evolution of the phase parameter *h(k)* with the channeled spectra at two different OPD in Figure 4.10(a), it becomes evident that the occurrence of phase discontinuities coincides with regions where one spectrum experiences a drop in intensity while the other remains unaffected. When the intensity of the channeled spectrum falls to the noise floor, the CMS algorithm fails to accurately reconstruct the phase, leading to discontinuities in the phase parameter *h(k)*.

The origin of the intensity modulations observed in the channeled spectra is non-trivial. We hypothesised that these modulations were linked to the incomplete suppression of the seed femtosecond pulses, occurring before and after the selected pulse, by the pulse picker. To investigate this, we adjusted the delay signal of the pulse picker to shift the gating window away from the selected pulse. Figure 4.11(a) presents the pulse picker output for three different delay settings. In the initial configuration, the output signal exhibits a main pulse of high intensity accompanied by two side pulses of comparable intensity. As the delay is increased, the intensity of one side pulse rises while the other diminishes, until the side pulse intensity becomes comparable to that of the main pulse.

It should be noted that our investigation focused on the evolution of the side

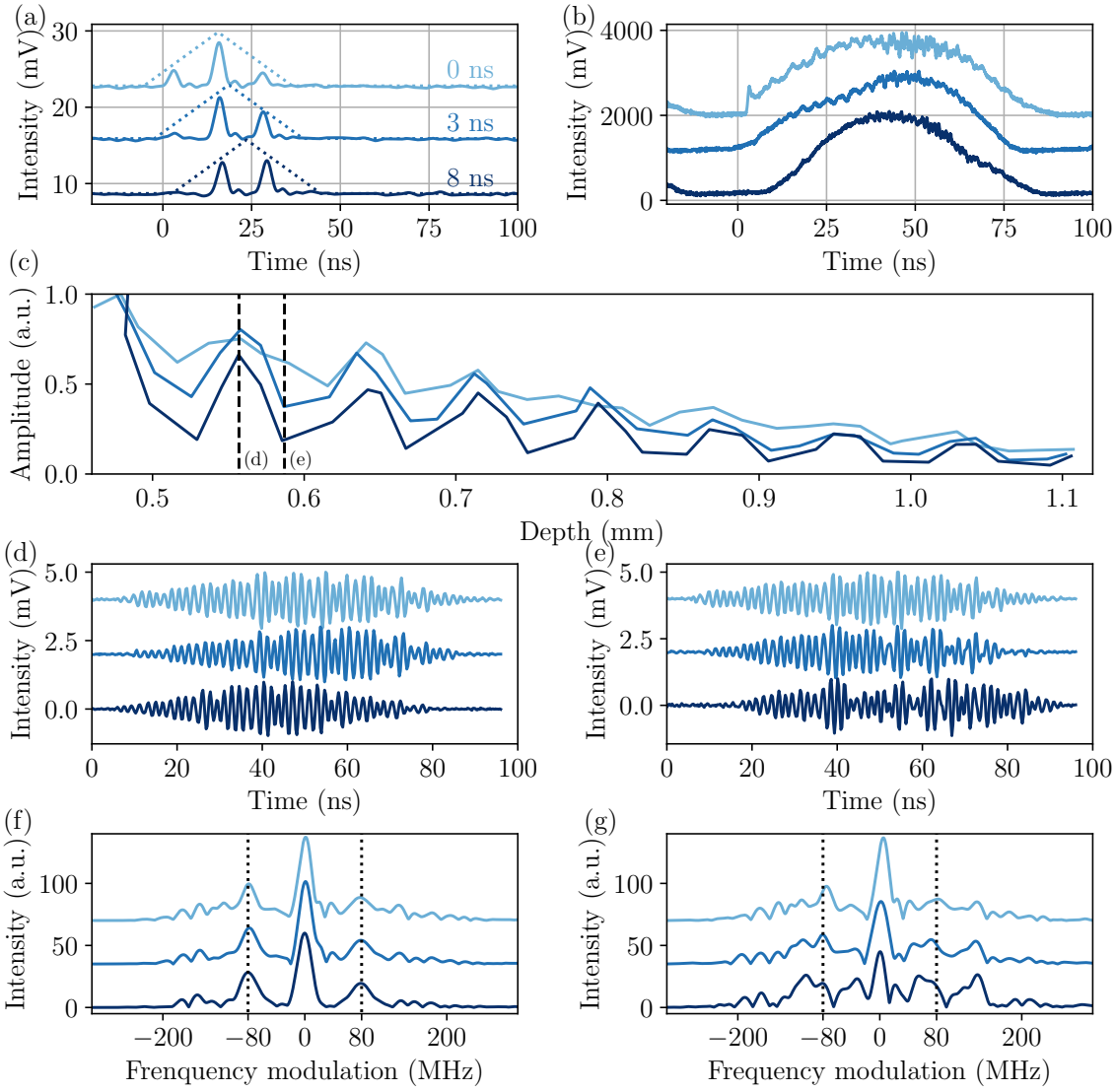

FIGURE 4.11: **Impact of the pulse picker operation on the SS-OCT system**. **(a)** Output pulse trains of the pulse picker for three different gate delays, alongside a schematic representation of the pulse picker transmission function (dotted). The colors in the subsequent plots correspond to the pulse picker outputs shown here. **(b)** Output swept-source signals. **(c)** Variation in A-Scan peak amplitude. **(d)**, **(e)** Channeled spectra at respectively an amplitude peak and drop for each pulse picker delay configuration. The dashed vertical lines in (c) mark the depth corresponding to the spectral plotted in (d) and (e). **(f)**,**(g)** Fourier transform of the channeled spectra respectively in (d) and (e), centered on the A-Scan frequency. Dashed vertical lines mark the 80 MHz modulations.

pulses. Consequently, the optical power incident on the photodetector was adjusted to optimise the detection of the side pulses. As a result, the main pulse saturated the photodiode, and thus the measured intensities of the side and main pulses cannot be directly used to infer their true power ratios.

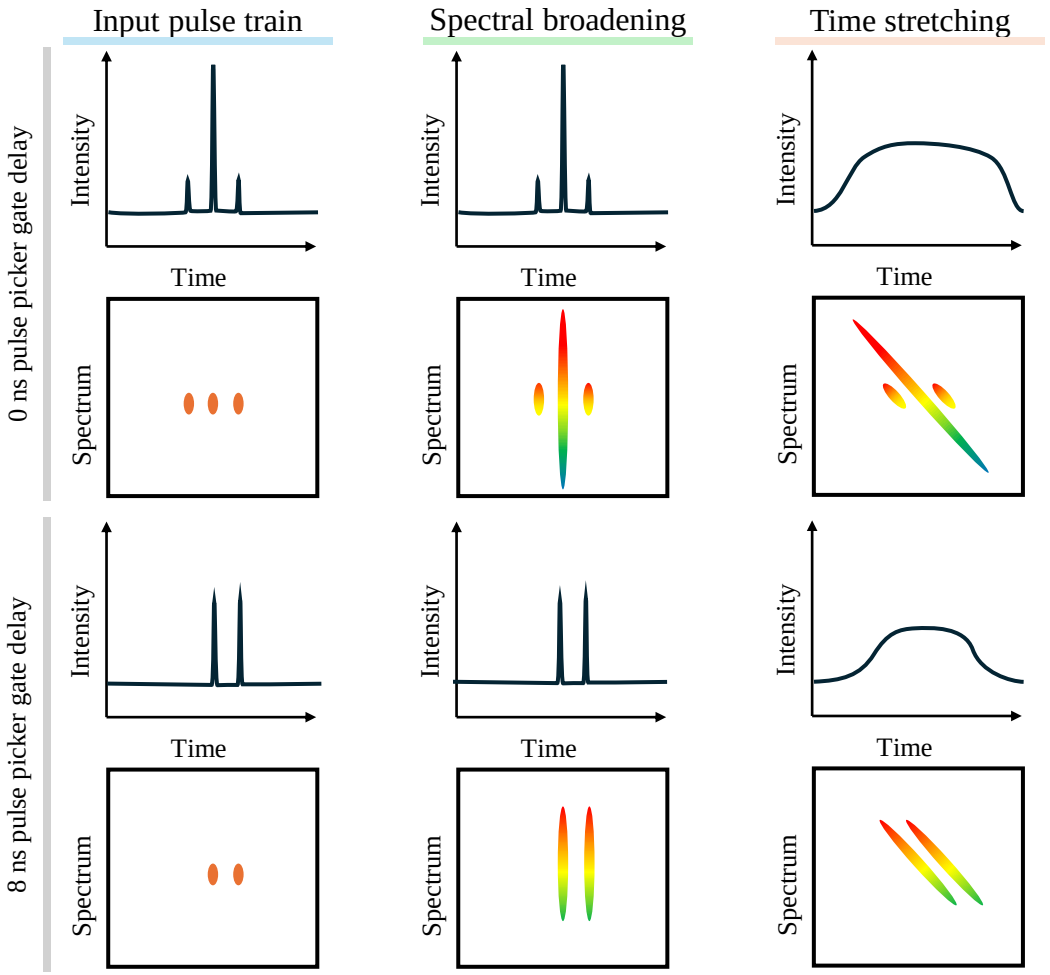

FIGURE 4.12: **Representation of the pulse evolution for two pulse picker delay**.

The three pulses experience nonlinear spectral broadening in the PM980 fibre. Ideally, an analysis of the spectral broadening generated by each side lobes would have been carried out. However, as we had no access to a frequency resolved optical gating (FROG) instrument, the spectrum of each pulse could not be observed separately. Nonetheless, due to the time-stretching of the long CFBG applying a dispersive Fourier transform to the signal, measuring the time trace corresponds to an acquisition of the spectrum of each pulse, shifted by 12.5 ns. This behaviour is represented in Figure 4.12. Figure 4.11 (b) presents the swept-source output measured with a 2 GHZ photodiode and a 2 GHz oscilloscope—the phenomenon being observed at all OPD, a limited imaging range was sufficient and more convenient for the processing.

Analysis of the time trace reveals that its duration is longest when the central pulse carries the majority of the optical energy. This observation is consistent with the nonlinear nature of the spectral broadening process, whereby greater pulse intensity leads to broader spectra, subsequently mapped into longer time traces by the dispersive Fourier transform. Conversely, when the energy is equally divided between two pulses, the broadening of each pulse is reduced, resulting in shorter individual time traces.

The swept-source light was then coupled into the OCT interferometer, and a roll-off measurement was performed with each pulse picker gate delay. Figure 4.11 (c) presents the peak amplitude of each A-Scan. As the side pulse intensity increases, the A-Scan amplitude fluctuation with OPD change increases, with modulation of amplitude leading to near total cancellation of the A-Scan. To quantify this modulation, the visibility of the A-Scan at 1.6 mm, marked with a vertical line, is calculated compared to the expected linear roll-off. Using the three delay parameters, the visibility drops from 75% to 53%, and 32%.

Pulse Picker gate delay	0 ns	3 ns	8 ns
80 MHz Modulation in Figure 4.11(g)	Visible	Visible	Weak (with 120 MHz)
Fringes visibility	75%	53%	32%

TABLE 4.2: **Impact of the pulse picker delay on the system.**

Figure 4.11 (d) and (e) respectively presents the interferometer output from high and low visibility A-Scans for the three pulse picker parameters, with the corresponding Fourier transform in (f) and (g). All the signals suffer from an 80 MHz modulation due to the unsuppressed side pulses. However, the channeled spectra from the low visibility A-Scan present an additional 120 MHz modulation. As the intensity of the side pulse increases, the relative intensity of the modulation compared to the A-Scan frequency is strengthened.

While the study of this phenomenon demonstrates the impact from the intensity distribution in the side pulses, the exact physics behind this modulation remains to be understood. The modulation of the A-Scans depending of the OPD

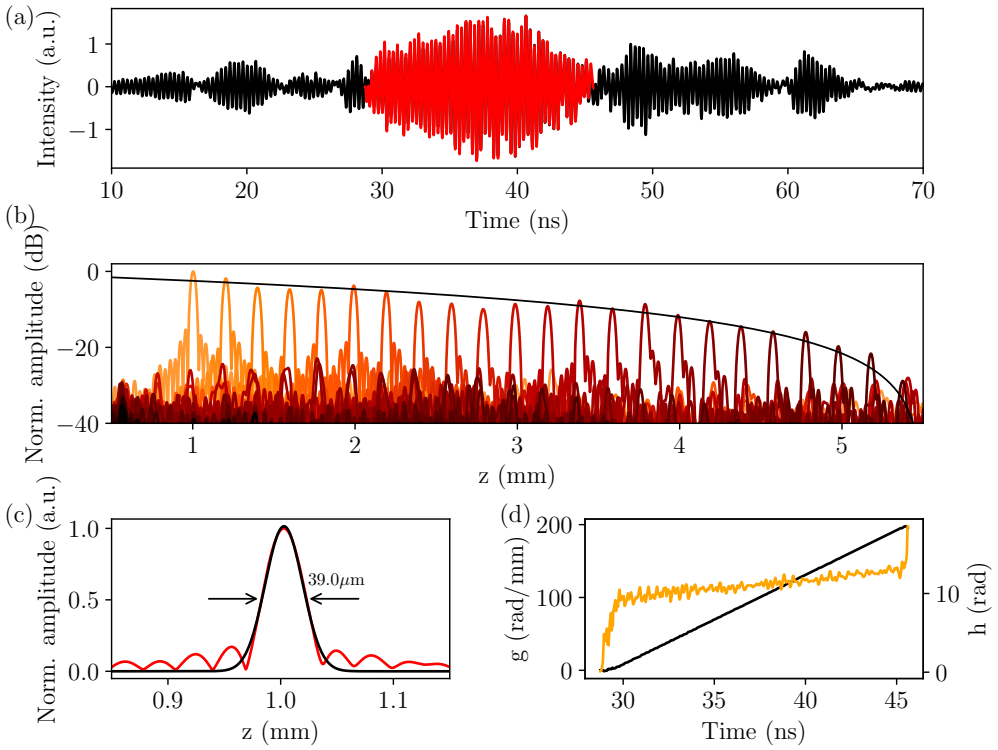

FIGURE 4.13: **OCT performance of reduced channeled spectra**. **(a)** Channeled spectra initial (black) and cropped (red). **(b)** Roll-off measurement. **(c)** Axial resolution measurement, with Gaussian fit (black). **(d)** CMS phase parameters.

does not correspond to the beating of two pulses of same wavelength separated by 12.5 ns. The nonlinear broadening phenomenon could be one factor leading to the intensity modulation.

Optimising the pulse picker delay allowed the visibility drop to be minimized, but it could not be totally removed, which is detrimental for the OCT imaging. One solution to reduce the impact of leftover modulations is to use only the time trace between two intensity drop in the post processing, as presented in Figure 4.13 (a). Figure 4.13 (b) shows the roll-off modulation free, and the phase in Figure 4.13 (d) is continuous over the total bandwidth. However, this technique degrades the axial resolution in air to 39.0 µm, see Figure 4.13 (c). This topic is further discussed in the conclusion. Alternatively, the development of femtosecond mode-locked laser cavities operating at 10 MHz would represent a solution.

In the previous subsection 4.3.3, the short-term phase noise of the system was characterised. However, in addition to short-term fluctuations, long-term drift

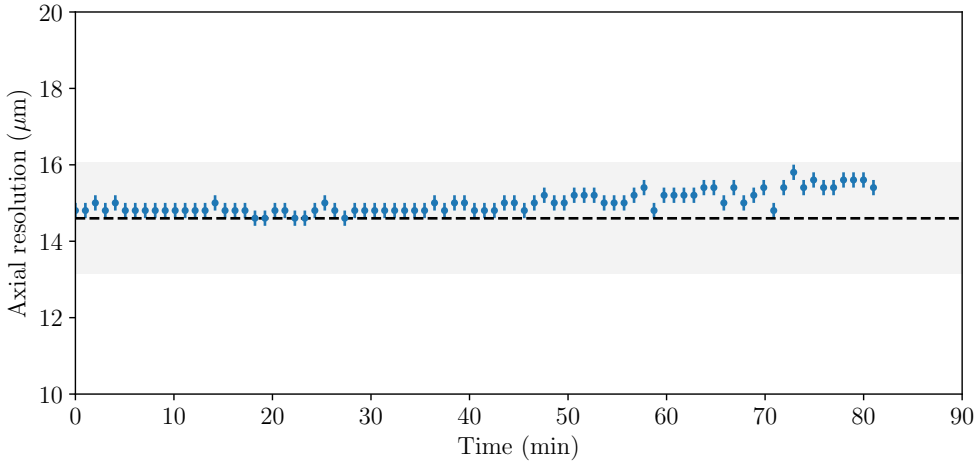

FIGURE 4.14: **Long term sweep stability.** The A-Scans are processed with CMS using masks measured at the start of the experiment. The dotted black line marks the initial axial resolution, and the grey shaded area covers ±10% variation.

of the phase within the sweep may occur due to the sensitivity of the sweeping mechanism to environmental variations, in particular temperature. Such drifts alter the time-to-wavenumber mapping and therefore affect computational methods relying on a prior calibration stage, such as CMS, for which the calibration masks become invalid if the sweeping characteristics change.

To assess this effect, the long-term stability of the calibration masks was investigated by performing an initial calibration followed by periodic acquisition of channeled spectra over a duration of 80,minutes. The resulting A-scans were processed using the initial calibration masks, and the axial resolution was monitored (Fig. 4.14). The axial resolution was observed to vary by less than 10%, demonstrating that imaging can be performed for more than one hour without recalibration.

This level of stability can be attributed to the passive sweeping mechanism of the supercontinuum stretched-pulse source, which exhibits reduced thermal load compared to mechanically tuned swept-sources. In contrast, conventional swept-source technologies, such as MEMS-tunable lasers and polygon-based scanners,

are known to exhibit sweep-to-sweep and long-term drift arising from mechanical motion and thermal effects, typically requiring active temperature stabilisation and/or frequent recalibration to maintain phase stability and k-space linearity. For instance, Robert Huber and colleagues have shown that FDML lasers can achieve high phase stability, but require careful thermal control of long fibre delay lines to suppress drift [3], [107]. Similarly, MEMS-based swept-sources generally rely on precise thermal and electronic control to maintain sweep repeatability, particularly in phase-sensitive OCT applications [4].

Even under well-controlled thermal conditions, residual drift in the sweep characteristics is typically mitigated through repeated k-clock calibration or numerical phase correction techniques rather than assuming a static calibration. In this context, the demonstrated stability of the proposed source, enabling operation over extended periods without recalibration, represents a practical advantage for applications requiring long acquisition times or reduced system complexity, such as in vivo or unsupervised imaging.

4.4.2 Biological sample imaging setup and dermal imaging

In order to perform real time imaging of *in vivo* biological samples, the OCT system had to be modified as presented in Figure 4.15. A customised commercial system including a chin-rest and a motorised 3 dimensional translation stage was used in the sample arm, for precise and stable positioning of the sample. To scan the sample, the beam was deflected by a pair of galvanometer scanner mirrors (Cambridge Technology, 6210H). For calibration, a 19 mm aspheric lens (Thorlabs, AC127-019-B-ML) and a flat silver mirror were used as a model eye. A telescope was integrated into the instrument to maximize the lateral resolution, and adequate dispersion compensation glass rods were placed in the reference arm. The lateral resolution was measured using a 1951 USAF target, achieving $\sim$ 19.69 µm, i.e. group 4, element 5. The fibre output of the sample arm, the scanners, and the telescope were positioned on a chin rest equipped with a motorized

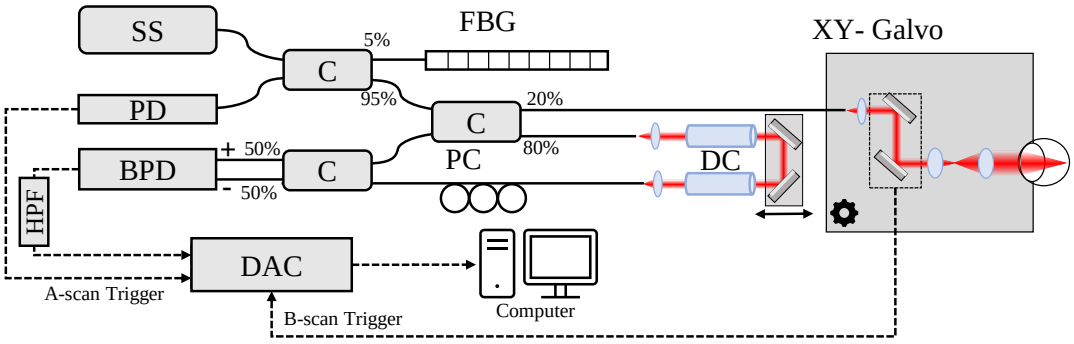

FIGURE 4.15: **OCT set-up used for live biomedical imaging.**SS: Swept-Source; C: fibre Coupler; FBG: Fibre Bragg Grating; PC: Polarisation Controller; PD: Photo-Detector; BPD: Balanced Photo-Detector; HPF: High-Pass Filter; DC: Dispersion Compensation glass; DAC: Digital-Analog Converter.

stage enabling pupil tracking as well as control of the sample arm length by adjusting the focal point in the eye.

Real-time visualization is critical for controlling the positioning of the *in vivo* biological sample. For this reason, a 12-bit waveform digitizer (AlazarTech, ATS9373) was incorporated into a computer for live processing. As its acquisition rate is 4 GS/s, using a 20 GHz photodetector is unnecessary. It was therefore relplaced by a balanced photodetector with smaller bandwidth but better noise performance (Thorlabs, PDB482C-AC).

Figure 4.16 shows the sensitivity measurement for multiple reference power levels, reaching up to 84 dB which corresponds to the shot-noise limited sensitivity, calculated as [114]:

$$S_{shot-noise} = 10\ log_{10}\left(\frac{\rho\ P_{sample}}{e\ f_{sweep}}\right) - IL \tag{4.5}$$

with ρ=0.72 A/W the photodiode responsivity at 1060 nm, P_{sample} the optical power incident on the sample, e the elementary charge of the electron, f_{sweep} the sweeping rate, and IL the insertion loss on the way back to the photodetector. The insertion loss in the system was measured to be 8.7 dB, accounting for both the fibre coupling and the components attenuation. To improve the sensitivity, further

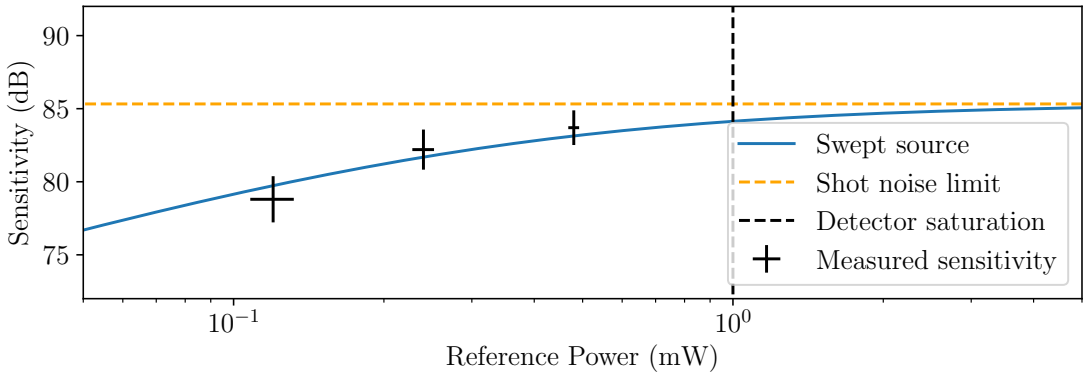

FIGURE 4.16: **Sensitivity of the SSOCT system (measured and theoretical).**

studies could use components with lower attenuation across the 100 nm bandwidth.

The first test of the SS-OCT interferometer for biological imaging was performed on a dermal sample. The safety limit on average power is higher for the skin than for the retina, enabling us to use higher average power for a better sensitivity. The thumb of a healthy volunteer was placed at the focal spot of the 19 mm aspheric lens. The motorized stage was turned off for this experiment. The galvanometer scanner are driven with a 1 V triangular signal at 750 Hz yielding to a scanning over 7.5 mm, reaching the maximum speed of the scanner. The power on the sample was 6.5 mW. A re-calibration was performed to account for the impact of the new components on the remaining phase. To enable real-time visualization, the number of synthesized masks was reduced to 500, and only one out of every 40 acquired B-Scans was displayed for a refresh rate of 20 Hz. The masks were generated for OPD from 0.3 mm to 2.3 mm respectively corresponding to the high-pass filter frequency and to the detection bandwidth. Each mask therefore covered 4.0 µm, with an oversampling factor in z of 3.65. During the imaging, the spectra were acquired only during the forward scan of the galvanometer scanner, and stored in the acquisition card buffer. During the backward scan, the data was then saved and processed by the computer. Each forward scan was 0.66 ms long, which, for a sweeping rate of 10 MHz, corresponds to 6600 A-Scans. This results

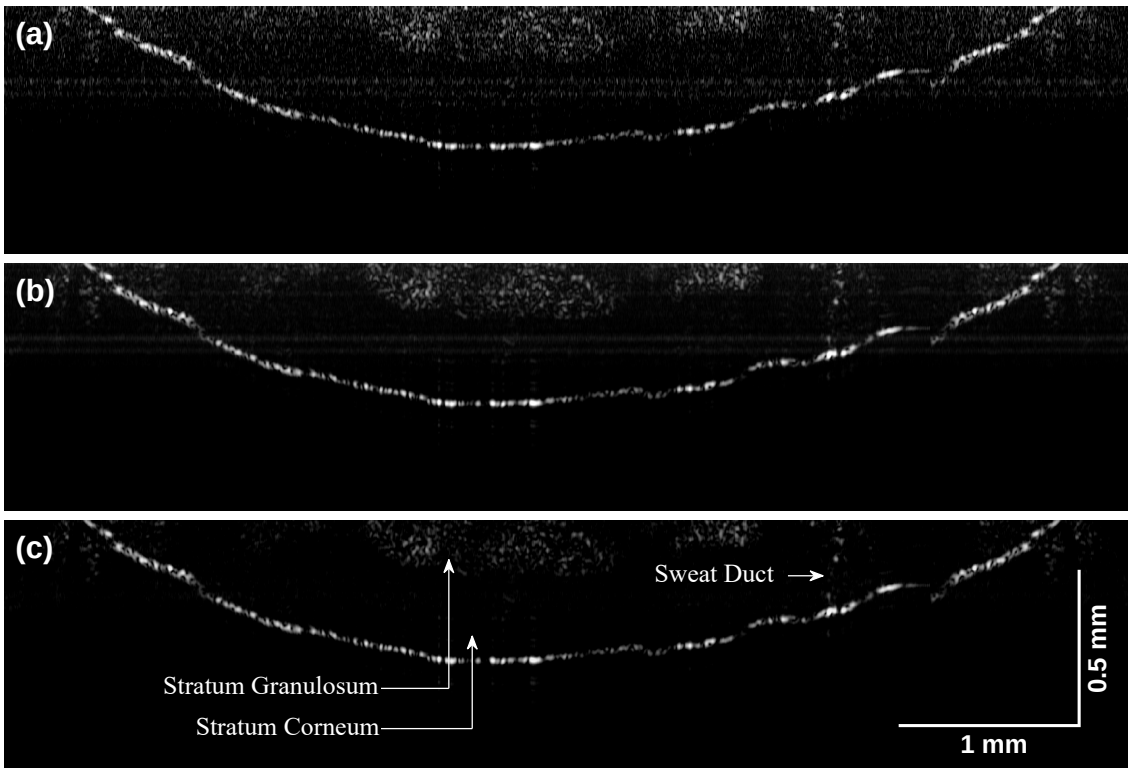

FIGURE 4.17: **B-Scan of a human thumb. (a)** Without averaging. **(b)** Averaged over 10 consecutive B-scans. **(c)** With B-Scan averaging and static A-Scan noise removal. The axial scale (vertical) corresponds to 0.5 mm measured in air.

in significant oversampling with 1.1 μm per A-Scan, i.e. an oversampling factor in x of 17.5. Considering this, the number of acquired A-Scans was reduced to 2200 to further diminish the processing time.

Figure 4.17 presents B-scans of the sample for various processing methods, with the OPD increasing from top to bottom of each image. Figure 4.17(a) is the B-Scan after CMS, without any averaging. The different structural features of the thumb are recognizable, with the bright curved line of the air/epidermis interface, two layers of the epidermis with the 0.28 mm thick stratum corneum and the grainy area on top of the image corresponding to the highly scattering stratum granulosum. Spiraling across the epidermis layers, the vertical line corresponds to a sweat duct.

In order to maximize the visibility of the dermis, the sample was positioned at a distance to the aspheric lens shorter than the focal length. This has two advantages. Firstly, the lateral resolution on the dermis is better, optimising the imaging

of its structure. Secondly, the dermis is placed at a shorter OPD which ensures a higher sensitivity compared to the epidermis that is at a larger OPD, due to the SS-OCT roll-off.

While the features are identifiable on this B-Scan obtained without averaging, the quality of the image is significantly improved by averaging 10 consecutive B-scans of the same area, as presented in Figure.4.17 (b). The speckles are reduced, leaving detailed structures. However, horizontal lines are still visible. These might be due to change in the swept-source between the CMS masks acquisition and the imaging. To remove these artifacts, a noise parameter was calculated by averaging all the A-Scans in the B-Scan, and subtracting this noise parameter from each A-Scan, see Figure.4.17 (c). The image has a higher contrast but also lost some details that were at the same depth as the artifacts.

4.4.3 Retinal imaging

The SS-OCT built successfully demonstrated imaging of two layers of the skin and captured fine details such as a sweat duct. However, the human retina is more challenging due to higher scattering and lower damage threshold. The power to the sample was reduced to 3.9 mW, and its stability was measured over 12 hours with a fluctuation $<$0.3 mW, to ensure operational safety.

Figure 4.18 and 4.19 presents B-Scans of the retina respectively of the macula region and of the optical nerve area. The scanning parameters were identical with those used for the skin imaging, with 750 Hz scanning rate over 7.5 mm. In both scanned areas, the nerve fibre layer is visible, as well as the retinal pigment epithelium (RPE) layers. In Figure.4.18 and Figure.4.19, (b) is the B-Scan without averaging is shown, while (a) and (c) present averaging respectively over 20 and 5 consecutive B-Scans. Although the layers are visible without averaging, using the 20 B-Scans averaging improves the contrast of the final image and reveals the choroid layer.

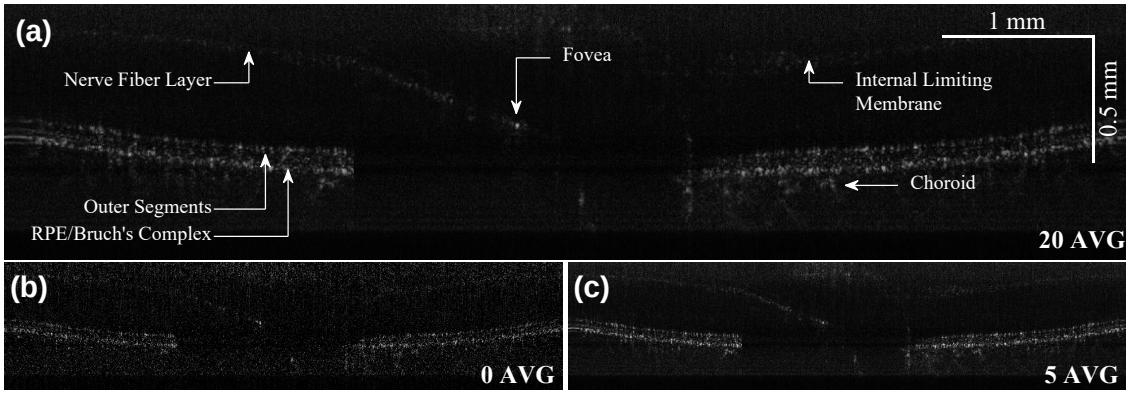

FIGURE 4.18: **B-Scan of the macula region.(a)** Averaging of 20 consecutive B-Scans. **(b)** B-Scan without averaging. **(c)** Averaging of 5 consecutive B-Scans.

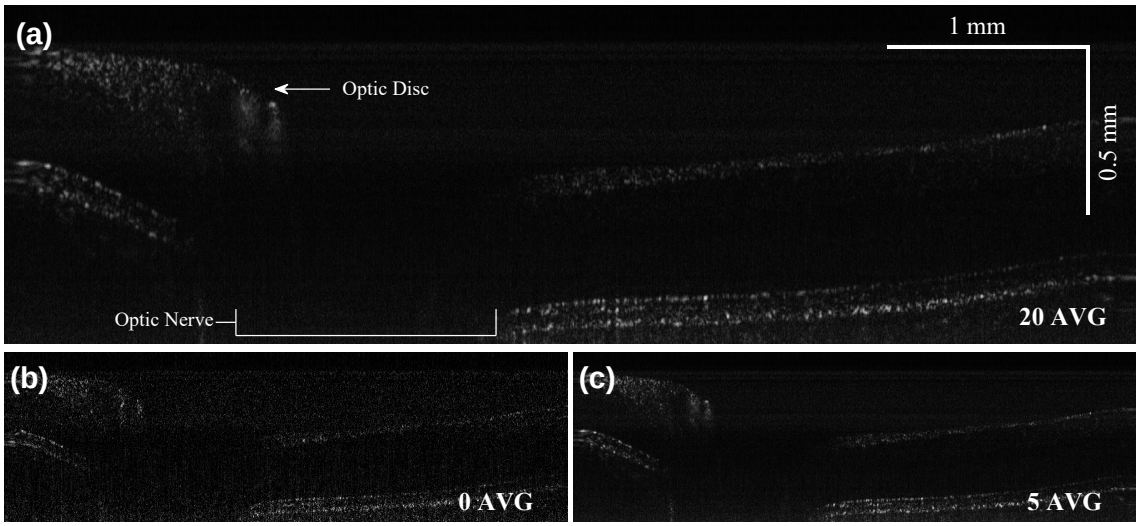

FIGURE 4.19: **B-Scan of the retina with optical nerve.(a)** Averaging of 20 consecutive B-Scans. **(b)** B-Scan without averaging. **(c)** Averaging of 5 consecutive B-Scans.

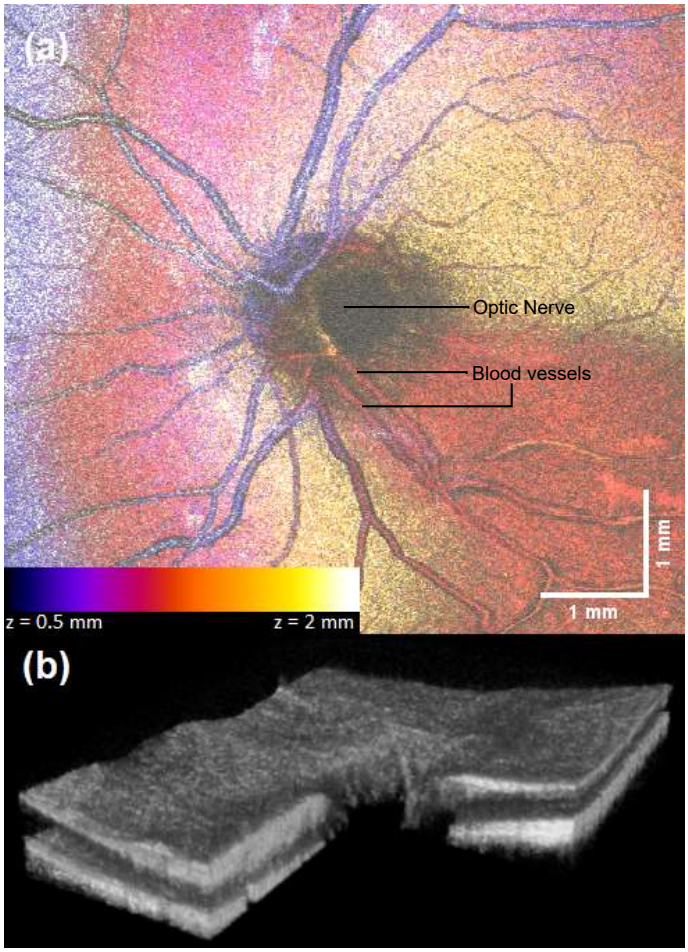

FIGURE 4.20: (a) Assembly of 500 *en face* views of a human retina with colour coded depth. (b) Volume of the same retina with a cut showing B-Scan of the optic nerve.

Figure 4.20 (a) and (b) respectively demonstrates *in vivo* imaging of a human retina with an *en face* view and a volume view. The area imaged is 6.75 mm by 8 mm. As for the precedent acquisition of images from a finger, the x-axis galvanometer scanner is driven with a 750 Hz triangular signal and the data are recorded during the forward scan and processed during the backward scan, leading to a B-Scan acquisition time of 0.33 ms. Each B-Scan is set to contains 2200 A-Scans, and each volume consists of 500 B-Scans. This leads to a volume rate of 4.5 Hz.

The optic nerve in the centre of the image is well defined, and the blood vessels are clearly distinguishable.

A faster volume acquisition rate can be achieved with a faster scanner on the x-axis, such as a resonant scanner or a KTN scanner. Further improvement of the OCT system could also exploit the high B-Scan rate for OCTA imaging. Additionally, the low axial range of the real time imaging set-up prevented scanning of large area due to the eye curvature. A detection system with higher sampling rate would enable wide angle imaging.

4.5 Conclusion

In conclusion, we presented a swept-source with extreme time-stretching enabling a sweeping rate of 10 MHz. It employs a long CFBG that provides a large GDD of 920 ps/nm over a 100 nm bandwidth covering 1000-110 nm. A pulse picker has been developed to reduce the seed laser repetition rate from 80 MHz to 10 MHz, preventing pulse overlap. In addition to the innovative use of long CFBG, the supercontinuum generation process has been carefully redesigned to improve the PSD over the spectral band of interest. The highly nonlinear PCF was replaced with a low nonlinearity SMF and a seed laser with higher power was used, resulting in a PSD 3 times higher, of 0.63 mW/nm and 0.1 mW/nm at 1050 nm respectively before and after time stretching.

An asymmetric SS-OCT interferometer was used to asses the performance of the swept-source for imaging. An axial range of 3.27 mm at -6 dB was measured, with an axial resolution of 14.6 μm. Considering the extremely high sweeping speed used, a decent sensitivity of 84 dB was obtained, close to the shot-noise limited sensitivity. This allowed the demonstration of *in vivo* biomedical sample imaging such as a thumb epidermis and retina, distinguishing key feature of these structures.

However, it was demonstrated during the study that the swept-source was limited by the acousto-optic modulator in the pulse picker, being too slow and insufficiently efficient for high selectivity, low loss pulse picking. Selecting a beam focus diameter within the AOM that permitted complete suppression of side pulses—even at the expense of reduced transmission efficiency—would likely have yielded better imaging performance, given the detrimental impact of these pulses on OCT image quality. Going forward, the development of improved raising speed AOM, or novel pulse picking techniques would be highly beneficial for the design presented here.

While improvements in system design may enhance sensitivity to approximately 90 dB through reduction of optical losses, achieving clinically relevant sensitivity levels within the permissible safety thresholds for retinal exposure remains a significant challenge. Future generations of detection systems may offer pathways to overcome this limitation. Alternatively, time-stretched supercontinuum technology presents a promising avenue in applications where higher optical powers are permissible. In biomedical imaging, for instance, this approach could be particularly advantageous in scenarios such as wide-area skin imaging requiring ultrafast scanning rates, or dynamic imaging of rapidly moving anatomical structures such as the vocal folds. Beyond biomedical applications, time-stretched supercontinuum swept-source OCT systems hold potential

for non-destructive evaluation processes in industrial settings. By enabling flexible optimisation of key imaging parameters—such as axial resolution, acquisition speed, and imaging range—this technology allows tailored adaptation of the OCT system to meet the specific requirements of diverse industrial processes, including but not limited to large-area thin-film inspection.

Part III

Conclusions and Outlook

Chapter 5

Conclusion

SWEPT source optical coherence tomography (SS-OCT) is a rapidly evolving imaging technique with significant potential applications, particularly in non-destructive testing and medical diagnostics. Ongoing developments in this field could greatly enhance imaging performance and improve healthcare quality.

This thesis has explored new swept-source technologies for high-speed OCT, focusing on the low-absorption spectral band of water, centred at 1060 nm. This wavelength is particularly relevant for biomedical imaging, as it enables deeper tissue penetration compared to visible wavelengths while maintaining higher resolution than longer-wavelength alternatives.

To achieve sweeping rates exceeding 5 MHz without buffering, an akinetic swept-source is required. In this work, the potential of time-stretched supercontinuum lasers for this application was investigated. This approach offers several advantages, including a broad bandwidth and the ability to achieve exceptionally high sweeping rates (ranging from tens to hundreds of MHz). However, previous studies have been limited by the high relative intensity noise (RIN) associated with conventional supercontinuum generation. In recent years, advances in photonic crystal fibre (PCF) manufacturing have enabled the development of a new supercontinuum generation method based on all-normal dispersion (ANDi) fibres, which significantly reduces RIN.

For the first time, this thesis demonstrates the use of ANDi supercontinuum

for a multi-MHz swept-source operating at 1060 nm. Initially, an 80 MHz sweeping-rate source was developed using a fibre-based stretcher. A simulation tool created during this research was used to optimise nonlinear broadening, while a detailed study of stretcher dispersion enabled linear sweeping and maximised the duty cycle while preventing pulse overlap.

An OCT system was built to harness the capabilities of this high-speed swept-source. B-scan imaging was successfully demonstrated at an A-scan rate of 40 MHz, along with the imaging of micrometre-scale fast-moving objects. Using the same swept-source, a second system was developed, incorporating a novel fast scanner based on an electro-optic deflector, enabling full-volume acquisition at 400 Hz.

While these initial results were promising, operating at such high-speeds inherently limits the imaging of fragile and highly scattering samples—such as the retina—due to shot noise and electrical noise. To address this, a second swept-source was developed at 10 MHz. Achieving lower sweeping rates required significant dispersion. However, fibre-based stretchers were unsuitable due to excessive optical attenuation, particularly at 1060 nm. Instead, a custom-made chirped fibre Bragg grating (CFBG) was investigated as an alternative dispersive device. A pulse picker was implemented to reduce the mode-locked laser rate from 80 MHz to 10 MHz, and supercontinuum generation was further optimised through simulations. This second system successfully demonstrated low-noise swept-source operation at 10 MHz.

An OCT system suitable for dermal and retinal imaging was employed with this swept-source. *In vivo* imaging of a thumb was successfully demonstrated, revealing multiple layers of the epidermis in a B-scan, as well as fine structures such as sweat ducts. Following this, *in vivo* retinal imaging was also achieved. In B-scan images, several key retinal features were identified, including the nerve fibre layer and the fovea in the upper layers, as well as the choroid in the deeper

layers. In a full-volume scan, the vascular system and optical nerve were visualised.

5.1 Outlook

Future work could explore the use of time-stretched supercontinuum at other wavelengths—like in the visible or in the Mid-IR—for high-speed non-destructive testing, with potential applications in areas such as thin multilayer film production and coating inspection.

Another potential avenue for further research is the use of multi-Watt femtosecond lasers to seed a time-stretched supercontinuum swept-source based on a fibre stretcher. The main limitation encountered in this work was the lack of power spectral density (PSD), which necessitated the use of an amplifier, thereby limiting the spectral bandwidth. A high-power mode-locked laser would enable improved noise characteristics as well as a significantly broader bandwidth, with the potential to achieve micrometre-level axial resolution.

A third direction for future research would be the development of a high-power (>100 mW) femtosecond fibre laser with low RIN (<5%), which could lead to a substantial reduction in cost, size and stability of the swept-source, improving its commercial viability.

In parallel, the capabilities of time-stretched supercontinuum swept-sources for SS-OCT remain constrained by the manufacturing limitations of several key components and would greatly benefit from advances in other fields. Firstly, the fabrication of longer CFBGs would enable smaller instantaneous linewidths, extending the imaging range and potentially allowing high-speed full-organ imaging. Secondly, and most critically, improvements in high-speed detectors—such as photodiodes, oscilloscopes, and acquisition cards—would enable full utilisation of high sweeping speeds. At present, the high electronic noise of fast detectors hinders high-sensitivity imaging. As a result, highly scattering samples,

such as the retina, must be imaged using lower-speed electronics, which in turn reduces the achievable axial range. Addressing these limitations would not only enhance the sensitivity and resolution of high-speed imaging but also expand its applicability to more challenging samples and complex biological structures.

Appendix A

Peer-reviewed articles published during the course of the doctoral programme

1. Genier Etienne, **Sacha Grelet**, Rasmus D. Engelsholm, Patrick Bowen, Peter M. Moselund, Ole Bang, John M. Dudley, and Thibaut Sylvestre. "Ultra-flat, low-noise, and linearly polarized fiber supercontinuum source covering 670–1390 nm." *Optics Letters* 46, no. 8 (2021): 1820-1823.

2. Jiménez, Alejandro Martínez, **Sacha Grelet**, Veronika Tsatourian, Patrick Bowen Montague, Adrian Bradu, and Adrian Podoleanu. "400 Hz volume rate swept-source optical coherence tomography at 1060 nm using a KTN deflector." *IEEE Photonics Technology Letters* 34, no. 23 (2022): 1277-1280.

3. **Sacha Grelet**, Alejandro Martínez Jiménez, Rasmus Dybbro Engelsholm, Patrick Bowen Montague, and Adrian Podoleanu. “40 MHz swept-source optical coherence tomography at 1060 nm using a time-stretch and supercontinuum spectral broadening dynamics.”, *IEEE Photonics Journal* vol. 14, no. 6, pp. 1-6, ()Dec. 2022) DOI: 10.1109/JPHOT.2022.3226820. pp. 4014–4017, DOI: 10.1364/OL.40.004014.

4. **Sacha Grelet**, Alejandro Martinez Jimenez, Patrick B. Montague, and Adrian Podoleanu. “Shot-noise limited, 10 MHz swept-source optical coherence tomography for retinal imaging.”, *IEEE Photonics Journal* vol. 17, no. 2, pp. 1-5, (April 2025), DOI: 10.1109/JPHOT.2025.3534424

Appendix B

Conferences proceedings and talks

1. **S. Grelet**, P. Bowen, P. M. Moselund, and A. Podoleanu, "80 MHz Swept Source Operating at 1060 nm Based on All- Normal-Dispersion Supercontinuum Generation for Ultrahigh-Speed Optical Coherence Tomography," in *European Conferences on Biomedical Optics 2021 (ECBO)*, OSA Technical Digest (Optica Publishing Group, 2021), paper ETu3D.5.

2. **S. Grelet**, P. B. Montague, A. Podoleanu, "Towards sub-5 µm axial resolution OCT from a multi-MHz swept source," Proc. SPIE 12390, *High-Speed Biomedical Imaging and Spectroscopy VIII*, 123900E (16 March 2023); https://doi.org/10.1117/12.2649688

3. A.M. Jiménez, **S. Grelet**, P.B. Montague, A. Bradu and A. Podoleanu, 2023, June. Dual Ultrahigh Speed Swept-Source & Time Domain Optical Coherence Tomography system using a time stretch laser and a KTN deflector. In European Conference on Biomedical Optics (p. 126320B). (Optica Publishing Group).

4. **S. Grelet**, P. B. Montague, and A. Podoleanu, "10 MHz swept-source for optical coherence tomography at 1050 nm," in *Conference on Lasers and Electro-Optics/Europe (CLEO/Europe 2023) and European Quantum Electronics Conference (EQEC 2023)*, Technical Digest Series (Optica Publishing Group, 2023).

Bibliography

[1] S. R. Chinn, E. A. Swanson, and J. G. Fujimoto, "Optical coherence tomography using a frequency-tunable optical source," *Opt. Lett.*, vol. 22, no. 5, pp. 340–342, Mar. 1997. DOI: 10.1364/OL.22.000340.

[2] B. Golubovic, B. E. Bouma, G. J. Tearney, and J. G. Fujimoto, "Optical frequency-domain reflectometry using rapid wavelength tuning of a cr4+:forsterite laser," *Opt. Lett.*, vol. 22, no. 22, pp. 1704–1706, Nov. 1997. DOI: 10.1364/OL.22.001704.

[3] R. Huber, M. Wojtkowski, and J. G. Fujimoto, "Fourier Domain Mode Locking (FDML): A new laser operating regime and applications for optical coherence tomography," *Opt. Express*, vol. 14, no. 8, pp. 3225–3237, Apr. 2006. DOI: 10.1364/OA_License_v1#VOR.

[4] S. Moon and E. S. Choi, "VCSEL-based swept source for low-cost optical coherence tomography," *Biomedical Opt. Express*, vol. 8, no. 2, p. 1110, Feb. 2017, ISSN: 2156-7085. DOI: 10.1364/boe.8.001110.

[5] S. Tozburun, M. Siddiqui, and B. J. Vakoc, "A rapid, dispersion-based wavelength-stepped and wavelength-swept laser for optical coherence tomography," *Opt. Express*, vol. 22, no. 3, p. 3414, Feb. 2014, First SPML design. Full SMF+DCF, 9 MHz, 1550 nm, ISSN: 10944087. DOI: 10.1364/oe.22.003414.

[6] R. Riha, A. Bradu, and A. Podoleanu, "Dual resonance akinetic dispersive cavity swept source at 900 kHz using a cFBG and an intensity modulator," *Opt. Lett.*, vol. 47, no. 16, pp. 4032–4035, Aug. 2022. DOI: 10.1364/OL.463675.

[7] S. Moon and D. Y. Kim, "Ultra-high-speed optical coherence tomography with a stretched pulse supercontinuum source," *Opt. Express*, vol. 14, no. 24, pp. 11 575–11 584, Nov. 2006. DOI: 10.1364/OE.14.011575.

[8] T. Klein and R. Huber, "High-speed OCT light sources and systems," *Biomedical Opt. Express*, vol. 8, no. 2, p. 828, Feb. 2017, ISSN: 2156-7085. DOI: 10.1364/boe.8.000828.

[9] D. Huang, F. Li, C. Shang, Z. Cheng, and P. K. A. Wai, "Reconfigurable time-stretched swept laser source with up to 100 MHz sweep rate, 100 nm bandwidth, and 100 mm OCT imaging range," *Photonics Research*, vol. 8, no. 8, p. 1360, Aug. 2020, ISSN: 2327-9125. DOI: 10.1364/prj.390076.

[10] D. Huang, F. Li, Z. He, Z. Cheng, C. Shang, and P. K. A. Wai, "400 MHz ultrafast Optical Coherence Tomography," *Opt. Lett.*, vol. 45, no. 24, p. 6675, Dec. 2020, ISSN: 0146-9592. DOI: 10.1364/ol.409607.

[11] C. Finot, B. Kibler, L. Provost, and S. Wabnitz, "Beneficial impact of wave-breaking for coherent continuum formation in normally dispersive nonlinear fibers," *J. Opt. Soc. Am. B*, vol. 25, no. 11, pp. 1938–1948, Nov. 2008. DOI: 10.1364/JOSAB.25.001938.

[12] A. M. Heidt, "Pulse preserving flat-top supercontinuum generation in all-normal dispersion photonic crystal fibers," *J. Opt. Soc. Am. B*, vol. 27, no. 3, pp. 550–559, Mar. 2010. DOI: 10.1364/JOSAB.27.000550.

[13] M. Jensen *et al.*, "Noise of supercontinuum sources in spectral domain optical coherence tomography," *Journal of the Optical Society of America B*, vol. 36, no. 2, A154–A160, Feb. 2019, ISSN: 0740-3224. DOI: 10.1364/josab.36.00a154.

[14] D. Huang *et al.*, "Optical coherence tomography," *Science*, vol. 254, no. 5035, pp. 1178–1181, Nov. 1991. DOI: 10.1126/science.1957169.

[15] A. Y. Alibhai, C. Or, and A. J. Witkin, "Swept Source Optical Coherence Tomography: a Review," *Current Ophthalmology Reports*, vol. 6, no. 1, pp. 7–16, Mar. 2018, ISSN: 2167-4868. DOI: 10.1007/s40135-018-0158-3.

[16] H. Li *et al.*, "Three-dimensional random-access confocal microscopy with 3D remote focusing system," *Communications Engineering*, vol. 3, no. 1, p. 166, Nov. 2024, ISSN: 2731-3395. DOI: 10.1038/s44172-024-00320-2.

[17] E. A. Swanson *et al.*, "In vivo retinal imaging by optical coherence tomography," *Opt. Lett.*, vol. 18, no. 21, pp. 1864–1866, Nov. 1993. DOI: 10.1364/OL.18.001864.

[18] J. Fujimoto and E. Swanson, "The development, commercialization, and impact of optical coherence tomography," *Investigative Ophthalmology Visual Science*, vol. 57, no. 9, OCT1–OCT13, Jul. 2016, ISSN: 1552-5783. DOI: 10.1167/iovs.16-19963.

[19] E. A. Swanson and J. G. Fujimoto, "The ecosystem that powered the translation of oct from fundamental research to clinical and commercial impact," *Biomed. Opt. Express*, vol. 8, no. 3, pp. 1638–1664, Mar. 2017. DOI: 10.1364/BOE.8.001638.

[20] R. M. Werkmeister *et al.*, "Ultrahigh-resolution OCT imaging of the human cornea," *Biomedical Opt. Lett. Express*, vol. 8, no. 2, p. 1221, Feb. 2017, ISSN: 2156-7085. DOI: 10.1364/boe.8.001221.

[21] A. Fercher, C. Hitzenberger, G. Kamp, and S. El-Zaiat, "Measurement of intraocular distances by backscattering spectral interferometry," *Optics Communications*, vol. 117, no. 1, pp. 43–48, 1995, ISSN: 0030-4018. DOI: https://doi.org/10.1016/0030-4018(95)00119-S.

[22] G. Haeusler and M. W. Lindner, ""Coherence radar" and "Spectral radar"-new tools for dermatological diagnosis," *Journal of Biomedical Optics*, vol. 3, no. 1, pp. 21–31, 1998. DOI: 10.1117/1.429899.

[23] R. Leitgeb, C. K. Hitzenberger, and A. F. Fercher, "Performance of fourier domain vs. time domain optical coherence tomography," *Opt. Express*, vol. 11, no. 8, pp. 889–894, Apr. 2003. DOI: 10.1364/OE.11.000889.

[24] P. E. Napoli *et al.*, "Fourier-domain OCT imaging of the ocular surface and tear film dynamics: A review of the state of the art and an integrative model of the tear behavior during the inter-blink period and visual fixation," *Journal of Clinical Medicine*, vol. 9, no. 3, Mar. 2020, ISSN: 20770383. DOI: 10.3390/jcm9030668.

[25] K. Bizheva *et al.*, "In vivo imaging and morphometry of the human pre-descemet's layer and endothelium with ultrahigh-resolution optical coherence tomography," *Investigative Ophthalmology and Visual Science*, vol. 57, no. 6, pp. 2782–2787, May 2016, ISSN: 15525783. DOI: 10.1167/iovs.15-18936.

[26] B. Potsaid *et al.*, "Ultrahigh speed spectral / fourier domain oct ophthalmic imaging at 70,000 to 312,500 axial scans per second," *Opt. Express*, vol. 16, no. 19, pp. 15 149–15 169, Sep. 2008. DOI: 10.1364/OE.16.015149.

[27] X. Yang *et al.*, "High-speed low-cost line-field spectral-domain optical coherence tomography for industrial applications," *Optics and Lasers in Engineering*, vol. 184, p. 108 631, 2025, ISSN: 0143-8166. DOI: https://doi.org/10.1016/j.optlaseng.2024.108631.

[28] L. S. Brea, D. A. D. Jesus, M. F. Shirazi, M. Pircher, T. van Walsum, and S. Klein, "Review on retrospective procedures to correct retinal motion artefacts in OCT imaging," *Applied Sciences (Switzerland)*, vol. 9, no. 13, Jul. 2019, ISSN: 20763417. DOI: 10.3390/app9132700.

[29] T. Klein, W. Wieser, C. M. Eigenwillig, B. R. Biedermann, and R. Huber, "Megahertz OCT for ultrawide-field retinal imaging with a 1050nm Fourier domain mode-locked laser," *Opt. Express*, vol. 19, no. 4, pp. 3044–3062, Feb. 2011. DOI: 10.1364/OE.19.003044.

[30] S. Aumann, S. Donner, J. Fischer, and F. Müller, "Optical coherence tomography (oct): Principle and technical realization," in *High Resolution Imaging in Microscopy and Ophthalmology: New Frontiers in Biomedical Optics*, J. F. Bille, Ed. Cham: Springer International Publishing, 2019, pp. 59–85, ISBN: 978-3-030-16638-0. DOI: 10.1007/978-3-030-16638-0_3.

[31] A. G. Podoleanu, G. M. Dobre, D. J. Webb, and D. A. Jackson, "Coherence imaging by use of a Newton rings sampling function," *Opt. Lett.*, vol. 21, no. 21, pp. 1789–1791, Nov. 1996. DOI: 10.1364/OL.21.001789.

[32] S. Yagi *et al.*, "A mechanical-free 150-kHz repetition swept light source incorporated a KTN electro-optic deflector," in *Optical Coherence Tomography and Coherence Domain Optical Methods in Biomedicine XV*, vol. 7889, SPIE, Feb. 2011, 78891J, ISBN: 9780819484260. DOI: 10.1117/12.876024.

[33] A. Velazco, M. Nord, A. Béché, and J. Verbeeck, "Evaluation of different rectangular scan strategies for STEM imaging," *Ultramicroscopy*, vol. 215, p. 113 021, 2020, ISSN: 0304-3991. DOI: 10.1016/j.ultramic.2020.113021.

[34] A. Kovács, "Scanning strategies for imaging arrays," in *Millimeter and Submillimeter Detectors and Instrumentation for Astronomy IV*, W. D. Duncan, W. S. Holland, S. Withington, and J. Zmuidzinas, Eds., International Society for Optics and Photonics, vol. 7020, SPIE, 2008, p. 702 007. DOI: 10.1117/12.790272.

[35] S. Moon and Z. Chen, "Phase-stability optimization of swept-source optical coherence tomography," *Biomed. Opt. Express*, vol. 9, no. 11, pp. 5280–5295, Nov. 2018. DOI: 10.1364/BOE.9.005280.

[36] Y. Ling, Y. Gan, X. Yao, and C. P. Hendon, "Phase-noise analysis of swept-source optical coherence tomography systems," *Opt. Lett.*, vol. 42, no. 7, pp. 1333–1336, Apr. 2017. DOI: 10.1364/OL.42.001333.

[37] S. Rivet, M. Maria, A. Bradu, T. Feuchter, L. Leick, and A. Podoleanu, "Complex master slave interferometry," *Opt. Express*, vol. 24, no. 3, p. 2885, Feb. 2016, ISSN: 1094-4087. DOI: 10.1364/oe.24.002885.

[38] A. Bradu *et al.*, "Recovering distance information in spectral domain interferometry," *Scientific Reports*, vol. 8, no. 1, Dec. 2018, ISSN: 20452322. DOI: 10.1038/s41598-018-33821-0.

[39] W. Drexler, M. Liu, A. Kumar, T. Kamali, A. Unterhuber, and R. A. Leitgeb, "Optical coherence tomography today: speed, contrast, and multimodality," *Journal of Biomedical Optics*, vol. 19, no. 7, p. 071 412, Jul. 2014, ISSN: 1083-3668. DOI: 10.1117/1.jbo.19.7.071412.

[40] G. P. Agrawal, "Chapter 10 - four-wave mixing," in *Nonlinear Fiber Optics (Sixth Edition)*, G. P. Agrawal, Ed., Sixth Edition, Academic Press, 2019, pp. 401–462, ISBN: 978-0-12-817042-7. DOI: https://doi.org/10.1016/B978-0-12-817042-7.00017-8.

[41] W. J. Tomlinson, R. H. Stolen, and A. M. Johnson, "Optical wave breaking of pulses in nonlinear optical fibers," *Opt. Lett.*, vol. 10, no. 9, 1985.

[42] J. E. Rothenberg, "Femtosecond optical shocks and wave breaking in fiber propagation," *J. Opt. Soc. Am. B*, vol. 6, no. 12, 1989.

[43] G. P. Agrawal, P. L. Baldeck, and R. R. Alfano, "Optical wave breaking and pulse compression due to cross-phase modulation in optical fibers," *Opt. Lett.*, vol. 14, no. 2, pp. 137–139, Jan. 1989. DOI: 10.1364/OL.14.000137.

[44] D. Anderson, M. Desaix, M. Lisak, and M. L. Quiroga–Teixeiro, "Wave breaking in nonlinear-optical fibers," *J. Opt. Soc. Am. B*, vol. 9, no. 8, pp. 1358–1361, Aug. 1992. DOI: 10.1364/JOSAB.9.001358.

[45] A. M. Heidt *et al.*, "Coherent octave spanning near-infrared and visible supercontinuum generation in all-normal dispersion photonic crystal fibers," *Opt. Express*, vol. 19, no. 4, pp. 3775–3787, 2011.

[46] A. M. Heidt, J. S. Feehan, J. H. V. Price, and T. Feurer, "Limits of coherent supercontinuum generation in normal dispersion fibers," *Journal of the Optical Society of America B*, vol. 34, no. 4, p. 764, Apr. 2017, ISSN: 0740-3224. DOI: 10.1364/josab.34.000764.

[47] S. G. Murdoch, R. Leonhardt, and J. D. Harvey, "Polarization modulation instability in weakly birefringent fibers," *Opt. Lett.*, vol. 20, no. 8, pp. 866–868, Apr. 1995. DOI: 10.1364/OA_License_v1#VOR.

[48] G. Millot, E. Seve, S. Wabnitz, and M. Haelterman, "Observation of induced modulational polarization instabilities and pulse-train generation in the normal-dispersion regime of a birefringent optical fiber," *J. Opt. Soc. Am. B*, vol. 15, no. 4, pp. 1266–1277, Apr. 1998. DOI: 10.1364/JOSAB.15.001266.

[49] G. P. Agrawal, "Chapter 6 - polarization effects," in G. Agrawal, Ed., Fifth Edition. Academic Press, 2013, pp. 193–244. DOI: https://doi.org/10.1016/B978-0-12-397023-7.00006-1.

[50] I. B. Gonzalo, R. D. Engelsholm, M. P. Sørensen, and O. Bang, "Polarization noise places severe constraints on coherence of all-normal dispersion femtosecond supercontinuum generation," *Scientific Reports*, vol. 8, no. 1, Dec. 2018, ISSN: 20452322. DOI: 10.1038/s41598-018-24691-7.

[51] A. Kudlinski *et al.*, "Simultaneous scalar and cross-phase modulation instabilities in highly birefringent photonic crystal fiber," *Opt. Express*, vol. 21, no. 7, p. 8437, Apr. 2013, ISSN: 10944087. DOI: 10.1364/oe.21.008437.

[52] R. H. Stolen, J. P. Gordon, W. J. Tomlinson, and H. A. Haus, "Raman response function of silica-core fibers," *J. Opt. Soc. Am. B*, vol. 6, no. 6, pp. 1159–1166, Jun. 1989. DOI: 10.1364/JOSAB.6.001159.

[53] C.-F. Chen and B. Luo, "The freeze of intrapulse raman scattering effect of ultrashort solitons in optical fiber," *Optik*, vol. 118, no. 1, pp. 1–4, 2007,

ISSN: 0030-4026. DOI: https://doi.org/10.1016/j.ijleo.2006.01.003.

[54] R. R. Alfano and S. L. Shapiro, "Emission in the region 4000 to 7000 å via four-photon coupling in glass," *Phys. Rev. Lett.*, vol. 24, no. 11, pp. 584–587, Mar. 1970. DOI: 10.1103/PhysRevLett.24.584.

[55] P. Russell, "Photonic crystal fiber," *Science*, vol. 299, no. 5606, pp. 358–362, Aug. 2003, ISSN: 13483447. DOI: 10.1126/science.1079280.

[56] J. C. Knight, "Photonic crystal fibres," *Nature*, vol. 424, no. 6950, pp. 847–851, 2003. DOI: 10.1038/nature01940.

[57] I. Zorin, P. Gattinger, A. Ebner, and M. Brandstetter, "Advances in mid-infrared spectroscopy enabled by supercontinuum laser sources," *Opt. Express*, vol. 30, no. 4, p. 5222, Feb. 2022, ISSN: 10944087. DOI: 10.1364/oe.447269.

[58] M. Falconieri, M. Marrocco, C. Merla, S. Gagliardi, F. Rondino, and M. Ghezelbash, "Characterization of supercontinuum generation in a photonic crystal fiber for uses in multiplex CARS microspectroscopy," *Journal of Raman Spectroscopy*, vol. 50, no. 9, pp. 1287–1295, Sep. 2019, ISSN: 10974555. DOI: 10.1002/jrs.5599.

[59] S. R. DS *et al.*, "Shot-noise limited, supercontinuum-based optical coherence tomography," *Light: Science & Applications*, vol. 10, no. 1, pp. 1–13, Jun. 2021. DOI: 10.1038/s41377-021-00574-x.

[60] C. Poudel and C. F. Kaminski, "Supercontinuum radiation in fluorescence microscopy and biomedical imaging applications," *Journal of the Optical Society of America B*, vol. 36, no. 2, A139, Feb. 2019, ISSN: 0740-3224. DOI: 10.1364/josab.36.00a139.

[61] C. S. Brès, A. D. Torre, D. Grassani, V. Brasch, C. Grillet, and C. Monat, "Supercontinuum in integrated photonics: Generation, applications, challenges, and perspectives," *Nanophotonics*, vol. 12, no. 7, pp. 1199–1244, Apr. 2023, ISSN: 21928614. DOI: 10.1515/nanoph-2022-0749.

[62] P. Russell, "Photonic crystal fibers," *Science*, vol. 299, no. 5605, pp. 358–362, 2003. DOI: 10.1126/science.1079280.

[63] F. Poletti, "Nested antiresonant nodeless hollow core fiber," *Opt. Express*, vol. 22, no. 20, pp. 23 807–23 828, Oct. 2014. DOI: 10.1364/OE.22.023807.

[64] S. Sawraj *et al.*, "PCF-based Sensors for Biomedical Applications-A Review," *IEEE Transactions on Nanobioscience*, 2024, ISSN: 15582639. DOI: 10.1109/TNB.2024.3462748.

[65] A. M. Cubillas *et al.*, "Photonic crystal fibres for chemical sensing and photochemistry," *Chemical Society Reviews*, vol. 42, no. 22, pp. 8629–8648, 2013. DOI: 10.1039/C3CS60128E.

[66] J. M. Dudley, G. Genty, and S. Coen, "Supercontinuum generation in photonic crystal fiber," *Reviews of Modern Physics*, vol. 78, no. 4, pp. 1135–1184, 2006, ISSN: 00346861. DOI: 10.1103/RevModPhys.78.1135.

[67] X. Zhu *et al.*, "Delivery of cw laser power up to 300 watts at 1080 nm by an uncooled low-loss anti-resonant hollow-core fiber," *Opt. Express*, vol. 29, no. 2, pp. 1492–1501, Jan. 2021. DOI: 10.1364/OE.415494.

[68] A. M. Heidt *et al.*, "High quality sub-two cycle pulses from compression of supercontinuum generated in all-normal dispersion photonic crystal fiber," *Opt. Express*, vol. 19, no. 15, pp. 13 873–13 879, Jul. 2011. DOI: 10.1364/OE.19.013873.

[69] J. K. Ranka, R. S. Windeler, and A. J. Stentz, "Visible continuum generation in air–silica microstructure optical fibers with anomalous dispersion at 800

nm," *Opt. Lett.*, vol. 25, no. 1, pp. 25–27, Jan. 2000. DOI: 10.1364/OL.25.000025.

[70] K. L. Corwin *et al.*, "Fundamental noise limitations to supercontinuum generation in microstructure fiber," *Phys. Rev. Lett.*, vol. 90, p. 113 904, 11 Mar. 2003. DOI: 10.1103/PhysRevLett.90.113904.

[71] I. B. Gonzalo, T. Vestergaard, and O. Bang, "All-Fiber-Based All-Normal Dispersion Supercontinuum Source Using a Femtosecond Fiber Laser with Hollow-Core Fiber Pulse Compression," in *Advanced Photonics 2018 (BGPP, IPR, NP, NOMA, Sensors, Networks, SPPCom, SOF)*, Optica Publishing Group, 2018, NpTh2I.3. DOI: 10.1364/NP.2018.NpTh2I.3.

[72] E. Genier *et al.*, "Ultra-flat, low-noise, and linearly polarized fiber supercontinuum source covering 670–1390 nm," *Opt. Lett.*, vol. 46, no. 8, p. 1820, Apr. 2021, ISSN: 0146-9592. DOI: 10.1364/ol.420676.

[73] C. J. Chang-Hasnain *et al.*, "Multiple wavelength tunable surface-emitting laser arrays," *IEEE Journal of Quantum Electronics*, vol. 27, no. 6, pp. 1368–1376, 1991.

[74] F. Koyama, "Recent Advances of VCSEL Photonics," *Journal of Lightwave Technology*, vol. 24, no. 12, pp. 4502–4513, 2006. DOI: 10.1109/JLT.2006.886064.

[75] V. Jayaraman *et al.*, "Vcsel swept light sources," in *Optical Coherence Tomography: Technology and Applications*, W. Drexler and J. G. Fujimoto, Eds. Cham: Springer International Publishing, 2015, pp. 659–686, ISBN: 978-3-319-06419-2. DOI: 10.1007/978-3-319-06419-2_23.

[76] B. Potsaid, V. Jayaraman, J. G. Fujimoto, J. Jiang, P. J. S. Heim, and A. E. Cable, "MEMS tunable VCSEL light source for ultrahigh speed 60kHz - 1MHz axial scan rate and long range centimeter class OCT imaging," in *Optical Coherence Tomography and Coherence Domain Optical Methods in*

Biomedicine XVI, vol. 8213, SPIE, Feb. 2012, p. 82130M, ISBN: 9780819488565. DOI: 10.1117/12.911098.

[77] G. D. Cole, E. Behymer, T. C. Bond, and L. L. Goddard, "Short-wavelength MEMS-tunable VCSELs," *Opt. Express*, vol. 16, no. 20, pp. 16 093–16 103, Sep. 2008. DOI: 10.1364/OE.16.016093.

[78] E. A. P. Grijalva *et al.*, "Novel 1.6 MHz swept source for real-time volumetric in-vivo OCT imaging of the human retina," SPIE-Intl Soc Optical Eng, Mar. 2023, p. 8, ISBN: 9781510658394. DOI: 10.1117/12.2649142.

[79] J. Zhang *et al.*, "Multi-MHz MEMS-VCSEL swept-source optical coherence tomography for endoscopic structural and angiographic imaging with miniaturized brushless motor probes," *Biomedical Opt. Express*, vol. 12, no. 4, p. 2384, Apr. 2021, ISSN: 2156-7085. DOI: 10.1364/boe.420394.

[80] D. Huang, Y. Shi, F. Li, and P. K. Wai, "Fourier domain mode locked laser and its applications," *Sensors*, vol. 22, no. 9, May 2022, ISSN: 14248220. DOI: 10.3390/s22093145.

[81] M. Klufts *et al.*, "828 kHz retinal imaging with an 840 nm Fourier domain mode locked laser," *Biomed. Opt. Express*, vol. 14, no. 12, pp. 6493–6508, Dec. 2023. DOI: 10.1364/BOE.504302.

[82] T. Klein, W. Wieser, L. Reznicek, A. Neubauer, A. Kampik, and R. Huber, "Multi-MHz retinal OCT," *Biomedical Opt. Express*, vol. 4, no. 10, p. 1890, Oct. 2013, ISSN: 2156-7085. DOI: 10.1364/boe.4.001890.

[83] J. P. Kolb, T. Pfeiffer, M. Eibl, H. Hakert, and R. Huber, "High-resolution retinal swept source optical coherence tomography with an ultra-wideband Fourier-domain mode-locked laser at MHz A-scan rates," *Biomed. Opt. Express*, vol. 9, no. 1, pp. 120–130, Jan. 2018. DOI: 10.1364/BOE.9.000120.

[84] S. Yamashita and M. Asano, "Wide and fast wavelength-tunable mode-locked fiber laser based on dispersion tuning," *Opt. Express*, vol. 14, no. 20, pp. 9299–9306, Oct. 2006. DOI: 10.1364/OE.14.009299.

[85] Y. Takubo and S. Yamashita, "High-speed dispersion-tuned wavelength-swept fiber laser using a reflective SOA and a chirped FBG," *Opt. Express*, vol. 21, no. 4, pp. 5130–5139, Feb. 2013. DOI: 10.1364/OE.21.005130.

[86] R. Khazaeinezhad, M. Siddiqui, and B. J. Vakoc, "16MHz wavelength-swept and wavelength-stepped laser architectures based on stretched-pulse active mode locking with a single continuously chirped fiber Bragg grating," *Opt. Lett.*, vol. 42, no. 10, pp. 2046–2049, May 2017. DOI: 10.1364/OL.42.002046.

[87] S. Yamashita, Y. Nakazaki, R. Konishi, and O. Kusakari, "Wide and fast wavelength-swept fiber laser based on dispersion tuning for dynamic sensing," *Journal of Sensors*, vol. 2009, no. 1, p. 572 835, 2009.

[88] F. Toadere, R.-F. Stancu, W. Poon, D. Schultz, and A. Podoleanu, "1 MHz Akinetic Dispersive Ring Cavity Swept Source at 850 nm," *IEEE Photonics Technology Letters*, vol. 29, no. 11, pp. 933–936, 2017. DOI: 10.1109/LPT.2017.2695083.

[89] R. Riha, A. M. Jimenez, G. Venugopal, M. Klufts, R. Huber, and A. Podoleanu, "Dispersion-Tuned Mode-Locked Laser for Swept Source OCT at 850 nm Using a cFBG and the Pulse Modulation Technique," *IEEE Photonics Journal*, vol. 16, no. 4, pp. 1–5, 2024. DOI: 10.1109/JPHOT.2024.3417829.

[90] I. Trifanov, A. Bradu, L. Neagu, P. Guerreiro, A. B. Lobo Ribeiro, and A. G. Podoleanu, "Experimental method to find the optimum excitation waveform to quench mechanical resonances of fabry–pérot tunable filters used in swept sources," *IEEE Photonics Technology Letters*, vol. 23, no. 12, pp. 825–827, 2011. DOI: 10.1109/LPT.2011.2140101.

[91] A. Mahjoubfar, D. V. Churkin, S. Barland, N. Broderick, S. K. Turitsyn, and B. Jalali, "Time stretch and its applications," *Nature Photonics*, vol. 11, no. 6, pp. 341–351, Jun. 2017. DOI: 10.1038/nphoton.2017.76.

[92] A. Bhushan, F. Coppinger, and B. Jalali, "Time-stretched analogue-to-digital conversion," *Electronics Letters*, vol. 34, no. 11, pp. 1081–1083, 1998. DOI: 10.1049/el:19980750.

[93] A. K. Lau *et al.*, "Interferometric time-stretch microscopy for ultrafast quantitative cellular and tissue imaging at 1 µm," *Journal of Biomedical Optics*, vol. 19, no. 7, p. 076 001, 2014. DOI: 10.1117/1.JBO.19.7.076001.

[94] X. Wei, A. K. S. Lau, Y. Xu, K. K. Tsia, and K. K. Y. Wong, "28 MHz swept source at 1.0 um for ultrafast quantitative phase imaging," *Biomedical Opt. Express*, vol. 6, no. 10, p. 3855, Oct. 2015, ISSN: 2156-7085. DOI: 10.1364/boe.6.003855.

[95] J. Kang, P. Feng, X. Wei, E. Y. Lam, K. K. Tsia, and K. K. Y. Wong, "102 nm, 44.5 MHz inertial-free swept source by mode-locked fiber laser and time stretch technique for optical coherence tomography," *Opt. Express*, vol. 26, no. 4, p. 4370, Feb. 2018, ISSN: 10944087. DOI: 10.1364/oe.26.004370.

[96] T. Huo *et al.*, "Ultrahigh-speed optical coherence tomography utilizing all-optical 40 MHz swept-source," *Journal of Biomedical Optics*, vol. 20, no. 3, p. 030 503, Mar. 2015, ISSN: 1083-3668. DOI: 10.1117/1.jbo.20.3.030503.

[97] T. S. Kim *et al.*, "9.4 MHz A-line rate optical coherence tomography at 1300 nm using a wavelength-swept laser based on stretched-pulse active mode-locking," *Scientific Reports*, vol. 10, no. 1, Dec. 2020, ISSN: 20452322. DOI: 10.1038/s41598-020-66322-0.

[98] M. Ibsen, M. Durkin, M. Zervas, A. Grudinin, and R. Laming, "Custom design of long chirped bragg gratings: Application to gain-flattening filter with incorporated dispersion compensation," *IEEE Photonics Technology Letters*, vol. 12, no. 5, pp. 498–500, 2000. DOI: 10.1109/68.841265.

[99] E. D. Diebold *et al.*, "Giant tunable optical dispersion using chromo-modal excitation of a multimode waveguide," *Opt. Express*, vol. 19, no. 24, pp. 23 809–23 817, Nov. 2011. DOI: 10.1364/OE.19.023809.

[100] Y. Qiu, J. Xu, K. K. Y. Wong, and K. K. Tsia, "Exploiting few mode-fibers for optical time-stretch confocal microscopy in the short near-infrared window," *Opt. Express*, vol. 20, no. 22, pp. 24 115–24 123, Oct. 2012. DOI: 10.1364/OE.20.024115.

[101] E. Genier, P. Bowen, T. Sylvestre, J. M. Dudley, P. M. Moselund, and O. Bang, "Amplitude noise and coherence degradation of femtosecond supercontinuum generation in all-normal-dispersion fibers," *JOSA B*, vol. 36, A161–A167, Feb. 2019, ISSN: 0740-3224. DOI: 10.1364/josab.36.00a161.

[102] J. Xu, C. Zhang, J. Xu, K. K. Y. Wong, and K. K. Tsia, "Megahertz all-optical swept-source optical coherence tomography based on broadband amplified optical time-stretch," *Opt. Lett.*, vol. 39, no. 3, p. 622, Feb. 2014, ISSN: 0146-9592. DOI: 10.1364/ol.39.000622.

[103] C. C. Rosa and A. G. Podoleanu, "Limitation of the achievable signal-to-noise ratio in optical coherence tomography due to mismatch of the balanced receiver," *Appl. Opt.*, vol. 43, no. 25, pp. 4802–4815, Sep. 2004. DOI: 10.1364/AO.43.004802.

[104] T. Imai, M. Ueno, Y. Sasaki, and T. Sakamoto, "Analyses of optical rays in KTN optical beam deflectors for device design," *Appl. Opt.*, vol. 56, no. 25, pp. 7277–7285, Sep. 2017. DOI: 10.1364/AO.56.007277.

[105] A. M. Jiménez, S. Grelet, P. B. Montague, A. Bradu, and A. Podoleanu, "Dual Ultrahigh Speed Swept-Source & Time Domain Optical Coherence Tomography system using a time stretch laser and a KTN deflector," in *Optical Coherence Imaging Techniques and Imaging in Scattering Media V*, Optica Publishing Group, 2023, 126320B. DOI: 10.1117/12.2670440.

[106] M. Azimipour, J. V. Migacz, R. J. Zawadzki, J. S. Werner, and R. S. Jonnal, "Functional retinal imaging using adaptive optics swept-source OCT at 1.6 MHz," *Optica*, vol. 6, no. 3, p. 300, Mar. 2019, ISSN: 2334-2536. DOI: 10.1364/optica.6.000300.

[107] T. Pfeiffer, M. Petermann, W. Draxinger, C. Jirauschek, and R. Huber, "Ultra low noise fourier domain mode locked laser for high quality megahertz optical coherence tomography," *Biomedical Opt. Express*, vol. 9, no. 9, p. 4130, Sep. 2018, ISSN: 2156-7085. DOI: 10.1364/boe.9.004130.

[108] D. Tosi, "Review of chirped fiber bragg grating (CFBG) fiber-optic sensors and their applications," *Sensors (Switzerland)*, vol. 18, no. 7, Jul. 2018, ISSN: 14248220. DOI: 10.3390/s18072147.

[109] X.-P. Pan *et al.*, "Femtosecond laser inscribed chirped fiber bragg gratings," *Opt. Lett.*, vol. 46, no. 9, p. 2059, May 2021, ISSN: 0146-9592. DOI: 10.1364/ol.422576.

[110] W. Klein and B. Cook, "Unified approach to ultrasonic light diffraction," *IEEE Transactions on Sonics and Ultrasonics*, vol. 14, no. 3, pp. 123–134, 1967. DOI: 10.1109/T-SU.1967.29423.

[111] D. Maydan, "Acoustooptical pulse modulators," *IEEE Journal of Quantum Electronics*, vol. 6, no. 1, pp. 15–24, 1970. DOI: 10.1109/JQE.1970.1076309.

[112] T. Sylvestre *et al.*, "Recent advances in supercontinuum generation in specialty optical fibers," *J. Opt. Soc. Am. B*, vol. 38, no. 12, F90–F103, Dec. 2021. DOI: 10.1364/JOSAB.439330.

[113] C. R. Smith, R. D. Engelsholm, and O. Bang, "Pulse-to-pulse relative intensity noise measurements for ultrafast lasers," *Opt. Express*, vol. 30, no. 5, p. 8136, Feb. 2022, ISSN: 10944087. DOI: 10.1364/oe.450819.

[114] J. F. de Boer, R. Leitgeb, and M. Wojtkowski, "Twenty-five years of optical coherence tomography: the paradigm shift in sensitivity and speed provided by Fourier domain OCT," *Biomed. Opt. Express*, vol. 8, no. 7, pp. 3248–3280, Jul. 2017. DOI: 10.1364/BOE.8.003248.